TRIBOLOGICAL IMPROVEMENTS OF CARBON-CARBON COMPOSITES BY

INFILTRATION OF ATOMIC LAYER DEPOSITED LUBRICIOUS

NANOSTRUCTURED CERAMIC OXIDES

Hamidreza Mohseni, B.S., M.S.

Dissertation Prepared for the Degree of

DOCTOR OF PHILOSOPHY

UNIVERSITY OF NORTH TEXAS

August 2011

APPROVED:

Thomas W. Scharf, Major Professor
Rajarshi.Banerjee, Committee Member
Richard F. Reidy, Committee Member
Nigel Shepherd, Committee Member
Srinivasan Srivilliputhur, Committee Member
Narendra Dahotre , Chair of the Department of
        Materials Science and Engineering
Costas Tsatsoulis, Dean of the College of
        Engineering
James D. Meernik, Acting Dean of the
        Toulouse Graduate School

Mohseni, Hamidreza. *Tribological Improvements of carbon-carbon composites by infiltration of atomic layer deposited lubricious nanostructured ceramic oxides*. Doctor of Philosophy (Materials Science and Engineering), August 2011, 177 pages, 11 tables, 74 figures, 156 references.

A number of investigators have reported enhancement in oxidation and wear resistant of carbon-carbon composites (CCC) in the presence of protective coating layers. However, application of a surface and subsurface coating system that can preserve its oxidation and wear resistance along with maintaining lubricity at high temperature remains unsolved. To this end, thermodynamically stable protective oxides (ZnO/Al$_2$O$_3$/ZrO$_2$) have been deposited by atomic layer deposition (ALD) to infiltrate porous CCC and graphite foams in order to improve the thermal stability and wear resistance in low and high speed sliding contacts. Characterization of microstructural evolution was achieved by using energy dispersive x-ray spectroscopy (EDS) mapping in scanning electron microscope (SEM) coupled with focused ion beam (FIB), x-ray tomography, high resolution transmission electron microscopy (HRTEM), scanning transmission electron microscopy (STEM) and X-ray diffraction (XRD). Evaluation of the tribological properties of CCC coated with abovementioned ALD thin films were performed by employing low speed pure sliding tribometer and a high speed/frequency reciprocating rig to simulate the fretting wear behavior at ambient temperature and elevated temperatures of 400°C.

It was determined with x-ray tomography imaging and EDS mapping that ALD ZnO/Al$_2$O$_3$/ZrO$_2$ nanolaminates and baseline ZrO$_2$ coatings exhibited excellent conformality and pore-filling capabilities down to ~100 μm and 1.5 mm in the porous CCC and graphite foam, respectively, which were dependent on the exposure time of the ALD precursors. XRD and HRTEM determined the crystalline phases of {0002} textured ZnO (wurtzite), amorphous Al$_2$O$_3$,

and $\{101\}$-tetragonal ZrO_2. Significant improvements up to ~65% in the sliding and fretting wear factors were determined for the nanolaminates in comparison to the uncoated CCC. A tribochemical sliding-induced mechanically mixed layer (MML) was found to be responsible for these improvements. HRTEM confirmed the presence of a high density of ZnO shear-induced basal stacking faults inside the wear tracks responsible for intrafilm shear velocity accommodation that mitigated friction and wear.

ACKNOWLEDGEMENTS

TABLE OF CONTENTS

LIST OF TABLES

LIST OF FIGURES

CHAPTER 1

INTRODUCTION

1.1 Motivation

For a long time carbon has been utilized in high temperature application such as heating elements. For instance in 1879, Thomas Alva Edison used a crude form of carbon fiber for the first electric lamp, and Germans used graphite for the jet vanes in the V_2 rocket. But the failure even at the low strains, thermal shock sensitivity, anisotropy and processing difficulties for large and complex shapes limited its application as the structural element. The introduction of carbon-carbon composites (CCC) was found to be a solution to overcome these challenges [1].

The CCC, carbon fiber reinforcements embedded in a carbonaceous matrix, has received significant attention in aerospace applications over the recent years, due to their high specific strength and stiffness at elevated temperature. Furthermore, CCC does not suffer from the strength degradation at elevated temperature, and exhibited reasonable thermomechanical strength at temperature above the 2000°C in nonoxidizing atmosphere. Superior frictional properties, low wear and high fracture toughness are the other advantages of these composites [1, 2]. However, in oxidizing environments, carbon is susceptible to oxidation at temperatures around 350 °C [3], and the rate of oxidation is dependent upon the diffusion of oxygen atoms into the CCC that results in significant material loss.

Another significant drawback of CCC is that the life-time of the parts, like any other load-bearing components that are subjected to vibration, can suffer from fretting

(oscillatory) wear, fretting fatigue and surface deterioration [4]. The extent of damage is strongly dependent upon variety of factors such as reciprocating amplitude, number of cycles to fretting, reciprocating frequency, material, contact temperature, stress field and environment [5].

Therefore for long-term reliable usage of parts which are made of CCC, application of advanced oxidation-resistant coating that can be a barrier to inhibit oxygen diffusion is crucial [6]. For instance, weight loss minimization and extended life-time was reported by Huang and co-workers by application of glassy B_2O_3, B_2O_3-SiO_2, SiC, and yttrium silicate into the CCC [7]. Nevertheless, establishing and maintaing a coherent and adherent external coating can be extermely challenging, due to the thermal expansion characteristics of the CCC. Furthermore, the coating technique must minimize the density of defects and imperfections from processing.

Depending on the required depth of protection, surface coating techniques such as chemical vapor deposition (CVD), physical vapor deposition (PVD), atomic layer deposition (ALD) and plasma spray can provide in-depth protection. In comparison to the other techniques, ALD has unique capabilities, which include creating an extremely conformal and uniform coating in high aspect ratio materials, and producing multilayer structures via continous manner and good control over the film thickness [8]. Therefore, ALD was considered as a potential candidate for deposition of nanolaminate coatings of different materials into the CCC to tailor the properties such as friction, hardness and wear resistance with consideration of in-service conditions.

In principle, the transition metal oxides are potential candidates for solid lubricity and thermal resistant coatings, due to their thermal stability at high temperatures (above 550 °C) and low shear strength [9, 10]. But at normal temperatures, the brittleness of bulk ceramic oxides results in crack formation and leads to an increase in friction and wear. If these oxides can exhibit lubricity even at low temperatures, they can be used in a wide variety of environments. It was reported that nano-grain sized polycrystalline ceramic oxides are able to accommodate plastic deformation through the diffusional creep of atoms along the grain boundaries [11-14]. Therefore, in this investigation, ALD was employed to infiltrate the CCC with nano-structured ceramic oxide coating of monolayer of ZrO_2 and trilayer composite coating of $ZnO/Al_2O_3/ZrO_2$ and unidirectional sliding wear test along with fretting wear test at various temperatures were conducted to confirm the influence of resultant structure on the tribological properties of CCC.

1.2 Contributions of Dissertation

The present investigation attempts to provide the following insights:

- In addition to the investigations which were conducted by Romanes [15] and Mensah [16], the further characterizations of microstructural features in ALD monolayer of ZrO_2 and ALD $ZnO/Al_2O_3/ZrO_2$ were employed in an attempt to find a correlation between the structure and tribological properties.

- Design, optimization and deposition of the ALD monolayer of ZrO_2 and ALD $ZnO/Al_2O_3/ZrO_2$ coatings on the CCC substrate to enhance tribological behavior of the CCC.

3

- Application of the unidirectional pure sliding test to evaluate the sliding wear and friction response of CCC coated with ALD monolayer of ZrO_2 and ALD $ZnO/Al_2O_3/ZrO_2$

- Simulating the fretting wear condition for CCC coated with ALD monolayer of ZrO_2 and ALD $ZnO/Al_2O_3/ZrO_2$ at ambient and elevated temperature.

- Interrogating the changes in the microstructural feature of the worn ALD films by using TEM and STEM to elucidate the mechanisms responsible for friction mitigation and wear reduction.

1.3 Dissertation Overview

This dissertation consists of six chapters, chapter one includes a brief introduction of the materials which are subject of this investigation and the reason behind this study. Chapter two offers a literature survey on materials, processing method and the subject of tribology which was mainly focused on sliding and fretting contacts. Chapter four presents the result of unidirectional sliding test and the performance of CCC substrate with various ALD coating under these tribological contacts. Chapter five present the result of the high frequency reciprocating test that simulates the fretting wear behavior of the CCC with various ALD coatings. Chapter six is a summary of the whole experimental parts and the entire conclusions.

All the procedure for substrate preparation, ALD deposition of nanolaminates, was conducted by using the facilities of the Laboratory for Moving Mechanical Assemblies at the Department of Materials Science & Engineering of the University of North Texas (UNT). Characterization of the coatings was performed by using equipment

at the UNT Center for Advanced Research and Technology (CART) and in the Department of Materials Science & Engineering.

1.4 Chapter References

1. Devi, G.R., Rama, R. K. *Carbon-Carbon Composites -An Overview.* Defence Science Journal, 1993. 43(4): p. 369-383.

2. Buckley, J.D., *Carbon-Carbon , An Overview.* American Ceramic Society Bulletin, 1988. 67(2): p. 364-368.

3. Bacos, M.P., *Carbon-carbon composites : oxidation behavior and coatings protection.* Le Journal de Physique IV, 1993. 03(C7): p. C7-1895-C7-1903.

4. Berthier, Y., L. Vincent, and M. Godet, *Fretting fatigue and fretting wear.* Tribology International, 1989. 22(4): p. 235-242.

5. Stachowiak, G.W. and A.W. Batchelor, *Fretting and Minor Wear Mechanisms*, in *Engineering Tribology* 2006, Butterworth-Heinemann. p. 621-650.

6. Gray, P.B., *Oxidation-inhibited carbon-carbon composites* U.S. Patent, Editor 1989, GA Technologies Inc. (San Diego, CA) USA.

7. Huang, J., et al., *Oxidation resistant yttrium silicates coating for carbon/carbon composites prepared by a novel in-situ formation method.* Ceramics International, 2007. 33(5): p. 887-890.

8. Doll, G.L., et al., *Chemical Vapor Deposition and Atomic Layer Deposition of Coatings for Mechanical Applications.* Journal of Thermal Spray Technology, 2010. 19(1/2): p. 510-516.

9.   Donnet, C. and A. Erdemir, *Historical developments and new trends in tribological and solid lubricant coatings.* Surface and Coatings Technology, 2004. 180-181: p. 76-84.

10.   Ouyang, J.H., S. Sasaki, and K. Umeda, *Microstructure and tribological properties of low-pressure plasma-sprayed ZrO_2-CaF_2-Ag_2O composite coating at elevated temperature.* Wear, 2001. 249(5-6): p. 440-451.

11.   Karch, J., R. Birringer, and H. Gleiter, *Ceramics ductile at low temperature.* Nature, 1987. 330(6148): p. 556-558.

12.   Zabinski, J., et al., *Lubricious zinc oxide films: synthesis, characterization and tribological behaviour.* Journal of Materials Science, 1997. 32(20): p. 5313-5319.

13.   Cahn, R.W., *Strategies to defeat brittleness.* Nature, 1988. 332(6160): p. 112-113.

14.   Mayo, M.J., *High and low temperature superplasticity in nanocrystalline materials.* Nanostructured Materials, 1997. 9(1-8): p. 717-726.

15.   Romanes, M.C., *Structure and Low-Temperature Tribology of Lubricious Nanocrystaline ZrO_2 Monofilms and ZnO/Al_2O_3 Nanolaminates Grown by Atomic Layer Deposition*, in *Department of Materials Science & Engineering* 2008, University of North Texas: Denton.

16.   Mensah, B.A., *Growth, structure and tribological properties of atomic layer deposited lubricious oxide nanolaminates*, in *Department of Materials Science and Engineering* 2010, University of North Texas: Denton.

CHAPTER 2

OVERVIEW OF MATERIALS, PROCESSING METHODS & TRIBOLOGY

2.1   Carbon-Carbon Composites

Carbon-carbon composites (CCC) are well-known materials for their superior mechanical properties at high temperatures. They exhibit high strength-to-weight ratio, good thermal shock resistance, low thermal expansion, good abrasion and corrosion resistance. These properties have introduced CCC as a potential candidate for numerous aerospace applications, where maintaining the structural stability at very high temperature is required [1-3]. However, widespread application of the CCC has currently encountered two main drawbacks. First, the extended usage of CCC at temperatures above ~350 ºC can lead to oxidation and subsequent degradation of CCC, and second, the production cost of CCC can be rather high and is only affordable by military and aerospace industries [2, 4].

Protective coatings are currently being studied as a solution for this first drawback of CCC, and this can play a critical role when the CCC is used in a highly oxidizing atmosphere, such as jet engines and hypersonic vehicles. Numerous investigations have reported the enhancement in life-time of CCC due to the application of oxidation barrier coatings [5-8]. For instance, Huang and co-workers reported the protection of CCC from oxidation at 1600 ºC for 202 hours by application of glassy B_2O_3, B_2O_3-SiO_2, SiC, and yttrium silicate protective coating [5].

2.1.1   Architecture and Microstructure

The carbon fiber and carbon matrix are the main constituents of the CCC, where the fiber provides strength, stiffness and fatigue resistance and the refractory carbonaceous matrix of various structures holds the fibers together [2, 4]. Depending on the starting materials and composite fabrication process, microstructure and accordingly properties of CCC can vary significantly. The matrix carbon can include small, randomly oriented crystallites of graphitic or turbostratic carbon, and this makes the matrix approximately isotropic. Also the matrix can be strongly anisotropic, by comprising of relatively large crystallites of highly graphitized carbon. In spite of having isotropic or anisotropic structure, the matrix includes some inherent porosity and microcracks, where their level strongly depends on the anisotropy of carbon in thermal expansion [1].

Carbon fibers are available in variety of architecture such as unidirectional, bidirectional, three-directional (three-dimensional) orthogonal weaves, or multidirectional weaves and braids (Fig.2.1), where type of fibers, fibers orientation, fibers volume fraction and the nature of the interface between fibers and matrix determine thermal, mechanical and physical properties of the composite. Most of the fibers are derived from polyacrylonitrile (PAN) resin, petroleum pitch (PIC) or rayon [1, 3, 4]. The fabrication process of the CCC, which is called densification, includes designing a preform of carbon fibers that is close to the net shape of final product and then filling the interstices between the carbon fibers by using (i) a chemical vapor deposition (CVD) process, or (ii) liquid phase impregnation, by employing thermosetting

8

resins or pitch. The CVD process is appropriate for thin-walled parts and the liquid phase

route is preferred for thick products (Fig.2.2).
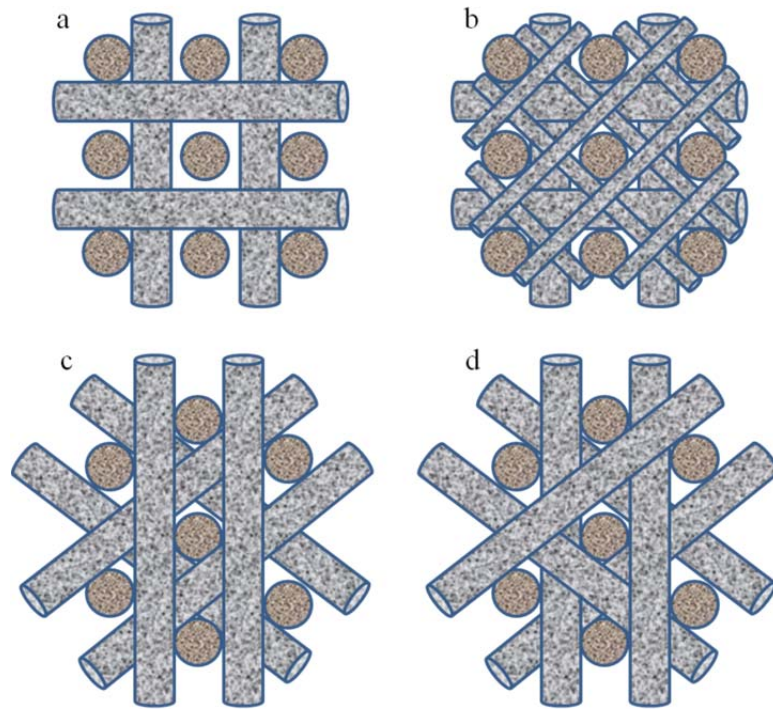
Figure 2.1: Fiber array architecture with (a) 3-
Directional, (b) 5-Directional, (c) 4-Directional and (d) 5-
Directional[2].
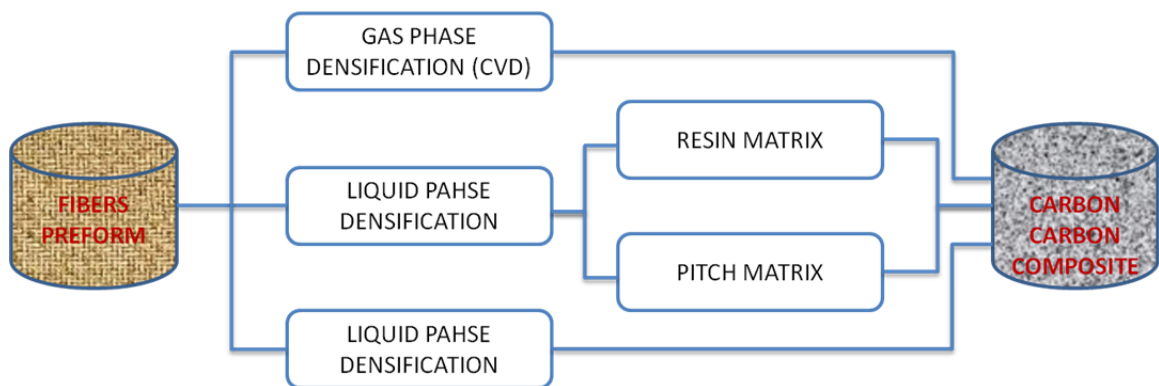
Figure 2.2: General fabrication process of carbon-carbon composite[2].

2.1.2 Oxidation Resistance

The inherent reactivity of the carbon to oxidation and degradation at temperatures above ~350 ºC restricts the potential application of the CCC, for extended period of time in oxidizing atmosphere, such as turbines' structural components and aircraft brake disks. In a general definition, the oxidation mechanisms in CCC involves (i) gas phase diffusion across the boundary layer, (ii) gas diffusion through the cracks in the CCC and (iii) reaction between carbon and oxygen to form oxidation product [4, 9]. Hence using any oxygen barrier that inhibits the oxygen diffusion to the porous structure is beneficial in this case.

Depending on the different carbon structure and the pore structures of CCC, the oxidation behavior of these materials can be different from one to another. Therefore depending on the structure of CCC, varieties of oxidation protection procedures, which mainly provide internal and/or external protection, are employed to enhance the service temperature of the components fabricated of CCC. It is of the importance that the protection methods exhibit thermal expansion compatibility with CCC substrate, low oxygen and carbon diffusion, low vapor pressure, chemical compatibility with carbon, wear and impact resistance [3, 4, 10].

Internal protection methods include purification and deactivation of the CCC from catalytic impurities or addition of oxidation inhibitors and additives to the CCC matrix, like B, Si, Zr or their compounds. The external protection comprises of (i) surface coatings and (ii) in-depth protection. The surface coatings techniques like physical vapor deposition (PVD), CVD and plasma spray are employed to deposit single/multilayer

composite coating of functionally graded materials of carbides, nitrides and oxides of Si, Zr, Ta, Al, etc. The in-depth protection includes sol-gel process and melt impregnation [2, 10].

Because of the mismatch in coefficient of thermal expansion (CTE) between CCC substrate and the external coating (Fig.2.3), establishing and maintaining a coherent, adherent, and conformal oxygen barrier coating is challenging. One of the attractive compounds for oxidation protection is B_2O_3, since it has high chemical compatibility with carbon, good wetting properties and low viscosity that allow the formation of thin protective glass films.

The external coating system should present minimum density of porosities and the self-healing properties that can undergo in-situ modification during the service time. For example, Sheehan and co-workers [4] showed that for the case of an ideal defect-free external coating the rate of carbon oxidation to CO can be calculated by Eq. 2.1:

$$R = \frac{kM}{\rho xt} \quad\quad\quad\quad\quad\quad\quad\quad \text{(Eq. 2.1)}$$

Where R is the percentage of carbon oxidation rate per hour, k is a constant, which is the product of the weight of carbon removed per weight of reacting oxygen, ρ is the density of the CCC, M is the rate of diffusive oxygen permeation through the coating, t is the coating thickness and x is the half of CCC section thickness.

Based on Eq.2.1 and the experimental data presented in Fig. 6 of [4], among the common refractory oxides, just SiO_2 and Al_2O_3 exhibited low oxygen permeabilities enough to protect CCC at 1000-1400 ºC for extended hours. But for achieving higher

11

temperature protection one potential approach could be using nonoxide coating that must initially oxidize before oxygen diffusion to the underlying carbon, these coatings could be average CTE value coatings like SiC, Si_3N_4 and HfB_2. For instance, it was shown that using HfB_2 as an external coating for CCC leads to formation of a protective oxide of ~ 200μm in 100hr at 1500 ºC and more efficiency was obtained by having SiO_2, which forms on SiC, Si_3N_4, and the oxidation depth is ~ 10μm in 100hr at 1650 ºC [3, 4].

Multilayer-composite coatings are known to be a suitable solution for large temperature range oxidation protection for carbon-carbon composites. Where each layer in this system contributes a complementary property to the whole assembly of the multilayer and functionally graded coating is obtained [5,11, 12]. It was shown by Huang and the co-workers that the application of interlayer of yttrium silicate coatings of SiC/yttrium silicates/borosilicate protected CCC from oxidation at 1600 C in air for 202 hours with the weight loss of 2.87 x 10^{-3} g/cm^3 [5].
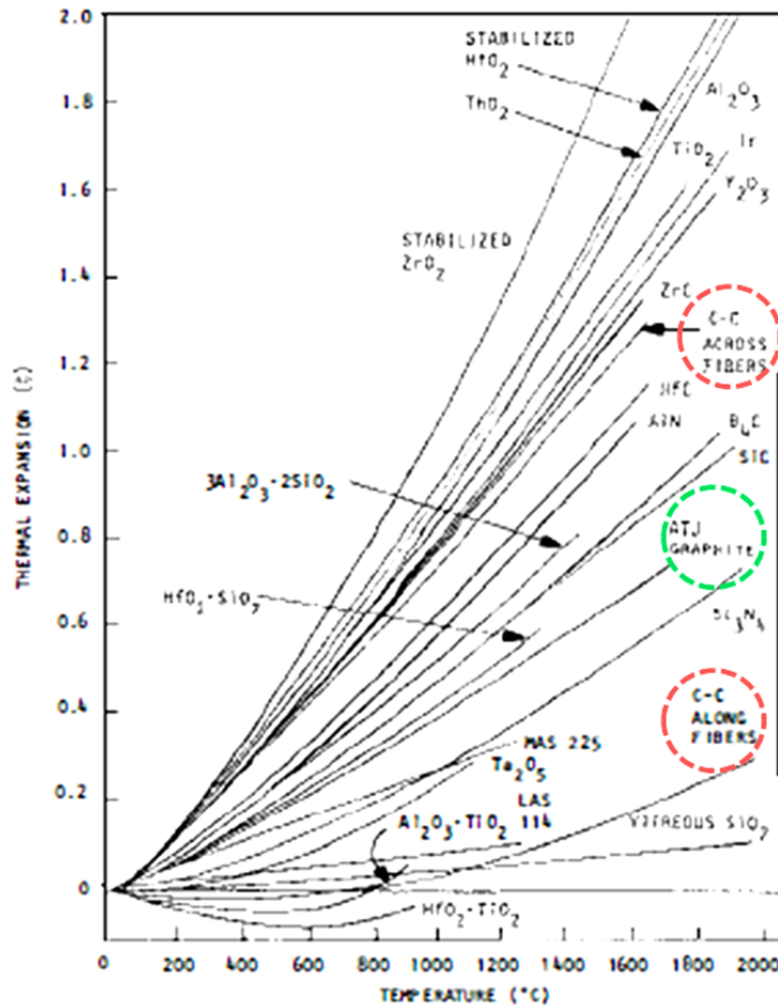
Figure 2.3: Coefficient of thermal expansion for
refractory materials [3].

2.2 Tribology

The word 'tribology' was originated from the Greek word of 'tribos', which means rubbing or sliding. The tribology as a novel field of science (defined in 1967) encompasses knowledge of various disciplines such as materials science, mechanical engineering, chemistry, physics, solid mechanics, and rheology. It involves operational

13

analysis of wear, friction and lubrication of interacting surfaces that are in relative motions (mainly rolling, sliding and normal loading).In short, wear is known as material loss due to the mechanical contact, friction is the main consequence of wear which causes energy dissipation, and the aim of lubrication is to control friction and minimize wear that can lead to considerable energy savings [13].

2.2.1 Friction

Friction is the resistance to the movement of one body over another body; frictional forces are non-conservative, since they convert the kinetic energy of materials in contact into internal energy. Friction is usually represented by coefficient of friction (μ) and is defined as the ratio of lateral force or frictional force (F) to normal force (L) [14]:

$$\mu = \frac{F}{L} \qquad\qquad\qquad\qquad\qquad\qquad (Eq.2.2)$$

Coefficient of friction (COF) typically ranges from 0.03 for a very well lubricated bearing, to 0.5 to 0.7 for dry sliding of metals with native oxides, and greater than 5 for clean metal surfaces in a vacuum. Nature of two surfaces, applied load, interfacial temperature, sliding velocity and environment are determinant factors in COF, hence, COF is considered as a system property rather than a material's property [15].

It has been suggested that the friction is originated from the atomic lattice vibrations occurring when atoms close to one surface are forced to move, by sliding action, into the opposing surface and some of the required mechanical energy for making

such a movement would be transformed into sound energy and subsequently into the heat [16, 17].

Fig. 2.4 schematically represents the microscopic mechanisms which are involved in friction of various degrees: (1) adhesion, (2) mechanical interaction of counterfaces, e.g., by plowing of one surface by asperities on the other surface, (3) deformation and/or fracture of surface layers such as oxides, and (4) formation of third body, agglomeration of wear particles, trapped between the moving surfaces.

The classical theory of adhesive friction introduced by Bowden and Tabor [18], considers friction force (F), as the product of the shear strength (τ) of the lubricant material and the contact area (A). Where the friction coefficient (μ) can be expressed by

$$\mu = \frac{F}{L} = \frac{A.\tau}{L} = \frac{\tau}{P_H} = \frac{\tau_0}{P_H} + \alpha \qquad \text{(Eq. 2.3)}$$

where L is the normal load, P_H is the mean Hertzian contact pressure; τ_o is the interfacial shear strength, a 'velocity accommodation parameter' which is a property of the interface; and α is the dependence of the shear strength on pressure. The constant 'α' is the lowest attainable friction coefficient for a given friction couple. In principle, a hard material with a soft skin ought to provide low friction coefficient by reducing τ_o and increasing P_H (low A).
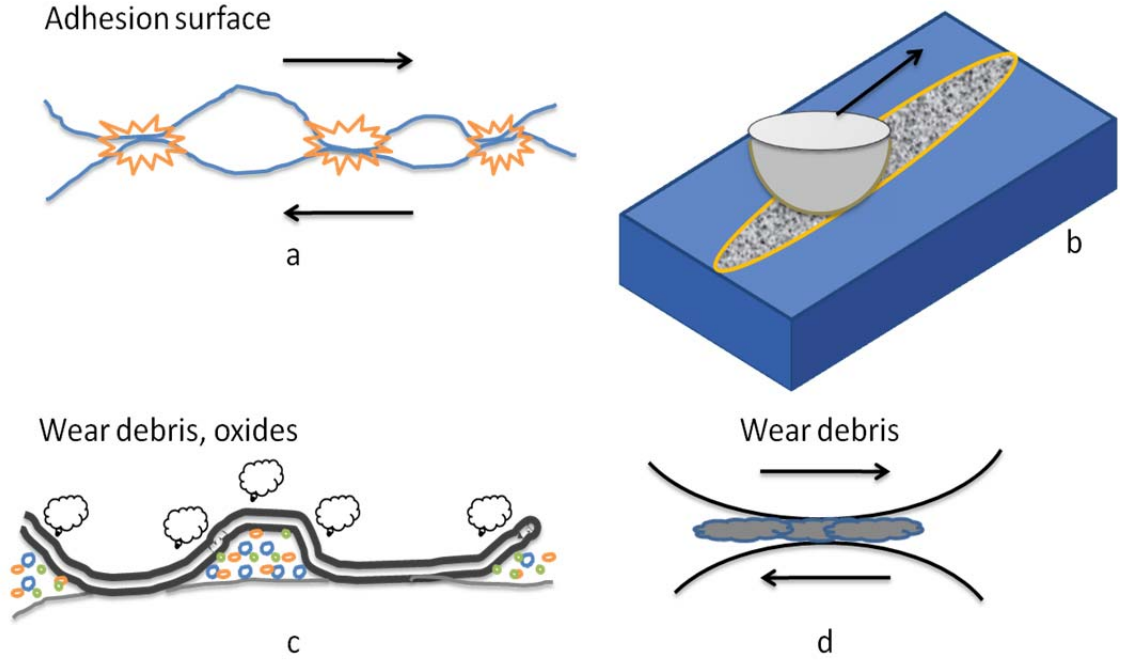
Figure 2.4: Friction mechanisms on microscopic level include (a) adhesion, (b) plowing, (c) deformation and fracture of oxides and (d) trapped wear particle [14].

The Hertzian elastic model [19] is employed to describe the loading configuration in elastic regime, which defines that: (i) the surfaces under the normal load have continuous profile, (ii) the area of the contact is finite and smaller than the dimensions of the nonconforming bodies and the radius of the surface curvature, (iii) the contact is thoroughly elastic and the contacting bodies do not undergo plastic deformation and (iv) absence of friction at the contact interfaces.

In Hertzian elastic contact model, for the configuration of 'sphere-on-flat', the friction can be expressed as:

$$\mu = \tau_0 \pi \left(\frac{3R}{4E}\right)^{2/3} L^{-1/3} + \alpha \qquad \text{(Eq. 2.4)}$$

where R is the sphere radius and E is the equivalent Young's modulus. In this Hertzian elastic model, the friction coefficient is dependent upon the normal load, when the contact deformation is elastic:

$$\mu \ \alpha \ L^{-1/3} \hspace{4cm} \text{(Eq. 2.5)}$$

Therefore, in the elastic contact regime, increasing the normal load (or mean Hertz pressure) can lead to decreases of friction coefficient. This linear relationship between normal load and friction coefficient has been verified experimentally for various solid lubricants (Fig. 2.5) [15].

Contact pressure is primarily supported by substrate in thin films and coatings, and increasing the hardness and modulus of the substrate leads to decrease in the contact area for a given normal load. Therefore, the ideal case for achieving low friction is by using a stiff and elastically hard substrate that can endure the normal load and keep the contact area small, while the coating has the ability to accommodate the interfacial shear strength and reduce junction strength [14], until the substrate yields and begins to deform plastically.
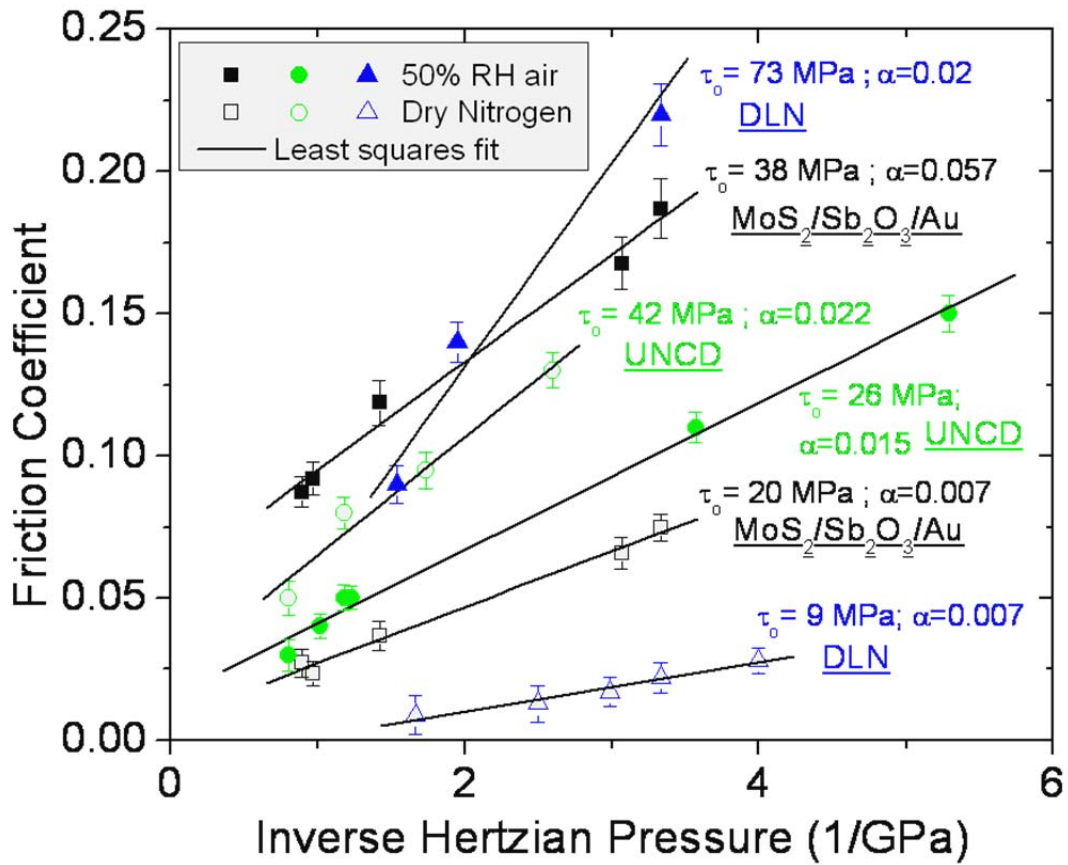
Figure 2.5: Linear regression fits for friction coefficient as a function of inverse Hertzian pressure fitted to $\mu=(\tau_o/P_H)+\alpha$ with values of shear strength (τ_o) shown for three low friction, environmentally-robust coatings: Si_3N_4 on DLN, UNCD coated Si_3N_4 on UNCD, and Si_3N_4 on $MoS_2/Sb_2O_3/Au$ in both dry nitrogen and humid air [T.W. Scharf private communication, [15]].

But the mechanical and physical properties of the interacting surfaces are not the only determining factors for friction as a system's property, surrounding environment can significantly affect the tribological performance of a coating. For instance the metal-on-metal friction is much higher in vacuum than in air, because the open air eases the formation of protective oxide layer [14].

The enhancement of surface characterization techniques, such as atomic force microscopy (AFM) and friction force microscopy (FFM), has made the investigation of friction and wear at atomistic and molecular scale feasible. Various tribological phenomena including surface roughness, adhesion, friction, scratching, wear, indentation, detection of tribolayer and boundary lubrication can be studied by employing these techniques [20]. The improvements in capabilities of surface characterization instruments have been coupled with the increased computational power, where molecular dynamic and atomistic simulations are capable of investigating the atomic scale contact mechanisms.

2.2.2 Wear

In principle, the interacting surfaces in contact (also known as tribosurface), may exhibit a damage pattern that can be a combination of various damage mechanisms. The surface damage classification includes: (1) damage by structural changes, such as tempering, aging, phase transformation, recrystallization, etc; (2) damage induced by plastic deformation, at the asperity level and beyond; (3) surface cracking, due to the excessive contact strains or cyclic variation of mechanically or thermally induced strains; (4) surface damage involving the transfer of materials from counterface and/or corrosive reaction by-products, and (5) surface damage associated with material loss, known as wear. It leaves behind the surface scar of various shape and size and gives a rise to decrease in a local dimension [21]. The occurrence of wear, as the most important surface damage mechanism, is related to the interaction of two solid surfaces that are in relative

19

motion such as sliding, rolling, etc. The fundamental elements in wear formation can be shear fracture, extrusion, chip formation, tearing, brittle fracture, fatigue fracture, chemical dissolution and diffusion.

Any mechanism, by which volume loss occurs, is called wear and although the formation of wear debris can influence the wear mechanism and wear rate, volume loss will take place only when these wear debris are ejected from the contact. Different wear mechanisms were classified by Matthews et. al. into two groups of mechanical wear mechanisms and physical-chemical wear mechanisms [22].

Mechanical wear mechanisms comprise:

- Ploughing or cutting by abrasive or erosive surface. In this mechanism the harder surface or particle generates wear debris and chips by abrading the softer surface. The rate at which the surfaces abrade depends on characteristics of each surface, speed of contact and environmental conditions. Removal of softer material by a harder phase during the abrasive wear includes several mechanisms of cutting, fracture, fatigue by repeated ploughing, and grain pull out. Direct observation of different aspects of abrasive wear has become possible by using scanning electron microscope which is coupled with in-situ pin-on-disk tribometer [13, 23].

- Extraction of materials from the surface, this occurs when the adhesive bond formed in the contact is stronger than the local cohesive strength of the material. The bond occurs at the asperities of the surfaces in contact and relative tangential movement of the surfaces causes the separation of the softer materials from its

substrate. Wear particles stick to the harder surface and forms loose debris that can be ejected from the contact or being re-circulated continuously into the contacts. Metals are usually prone to adhesive wear and if the lubricant film does not separate the two sliding surfaces, the adhesive wear is inevitable. Besides the application of proper lubrication, the availability of some surface contamination such as surface oxides can prevent the adhesion of two contacting surface [13].

- Plastic deformation/compaction: this mechanism is due to the roughness and waviness of two contacting surfaces. The asperities on the either contacting surfaces collide during the relative motion and this gives a rise to plastically deformed asperities on one surface or on the either surfaces that eventually leads to materials removal from the asperities.

Physical-chemical wear mechanisms include:

- Chemical wear: detrimental surface chemical reactions like electrochemical and oxidation reactions, which are initiated by environment, can lead to significant loss of underlying material. This occurs when the chemical reaction is simultaneously followed by sliding motion or other mechanical mechanism of wear.

- Physical wear: dissolution, diffusion and/or evaporation of material from contacting surfaces can lead to this type of wear. For instance, in cutting tools, where there is a true contact between atoms of two surfaces and combined with a high interfacial temperature, diffusion of chemical elements from one body to another body occurs [13].

In practice it is uncommon to observe just one wear mechanism being responsible for material loss and surface damage. In most cases, different combinations of various mechanisms are involved, but the relative contribution of each individual mechanism will be changed based on the local variations in the tribological system. This is a significant obstacle in wear prediction and understanding the dominant wear mechanism at each time interval can be beneficial in predicting how the wear rate changes with time.

2.2.2.1 Sliding Wear

Sliding wear is related to the type of wear which is generated by sliding of one surface along another surface. The surface condition is a determining factor in sliding wear behavior, where surfaces of (i) metals are usually covered with oxide layer, followed by a second layer of adsorbed gases and hydrocarbons; (ii) ceramics also covered by adsorbed gases and possibility of oxidation for non-oxide ceramic, and (iii) polymers may contain absorbed water and most likely covered with mold release agents, adsorbed gases and oils [24].

When two surfaces are in sliding contact against each other, depending on the contact pressure, the surface films such as adsorbed layer, oxides and hydrocarbons will either be squeezed out of the contact or if the contact pressure is high enough, the surface layer may fracture and the substrates will be exposed to the contact area and asperities bond together. When two contacting surfaces have identical ionic or covalent atomic structure the bond has a very high strength. Bond strength will be usually less when the lattice dimension of one is different from that of the other. Conformality of the contacting

surfaces has influence on type of bonding, where ductile materials, unlike to brittle materials, tend to deform and increase the likelihood of bond formation.

Sliding applies shear stress, besides the normal stresses already imposed, to the contacting surfaces and this may give a rise to plastic flow, crack initiation, crack propagation and eventually fracture of materials. A layer of mechanically mixed substances is formed after some sliding periods. This layer includes wear debris, but most of which will remain as a third body, such as a transfer film. The wear rate will depend on the tendency of the mechanically mixed layer to leave the system. Vibration modes of the contacting bodies, the temperature, possible chemical reactivity with the surrounding environment, and many other parameters can determine the wear rate in this case. The Pin-on-disk (POD) method is known as a method to evaluate sliding wear rate and coefficient of friction of the coated and uncoated surfaces at relatively low sliding speeds and normal loads. A pin or ball of various materials is used to run on the surface of a rotating plate. Sliding speed, sliding distance, contact load/pressure, lubrication condition, temperature and humidity are important parameters in conducting POD analysis [13, 24, 25]. Further details about this tribological test will be given in chapter 3.

2.2.2.2 Fretting Wear

Fretting wear and surface damage occurs whenever small-amplitude oscillatory movement takes place between two contacting surfaces. For extended period of time, this may lead to deterioration of fatigue life followed by fatigue cracks and failure. The extent of fretting damage is much greater than the magnitude of the oscillatory (sliding)

distance. Reciprocating movements as short as 0.1μm in amplitude, which is coupled with high number of reciprocating cycles, can cause failure of the component even at very low levels of stress [13, 25-27]. Fretting wear is present in contacts, which are subjected to vibration, and causes the loss of clearance in many applications. Due to the small sliding amplitude wear debris can be encapsulated in the contact and this leads to material jamming that stops the functionality of the component in a system.

Based on the contact load and the reciprocating amplitude/frequency three fretting regimes are known i.e. stick, partial slip and gross slip (Fig. 2.6 and 2.7). In this case critical loads and reciprocating amplitude at the boundary of the three major regions depend on materials properties, contact geometry and number of cycles.
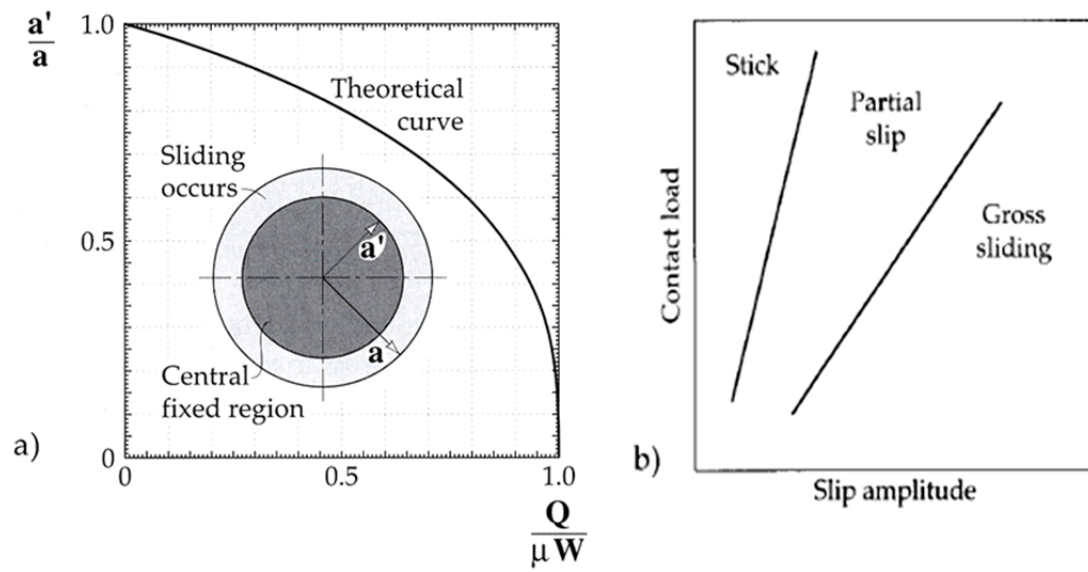
Figure 2.6: (a) The relationship between the radius of central stationary zone (a′/a) and oscillatory tangential load (Q) and frictional force (μW), and (b) schematic fretting regime map [13].
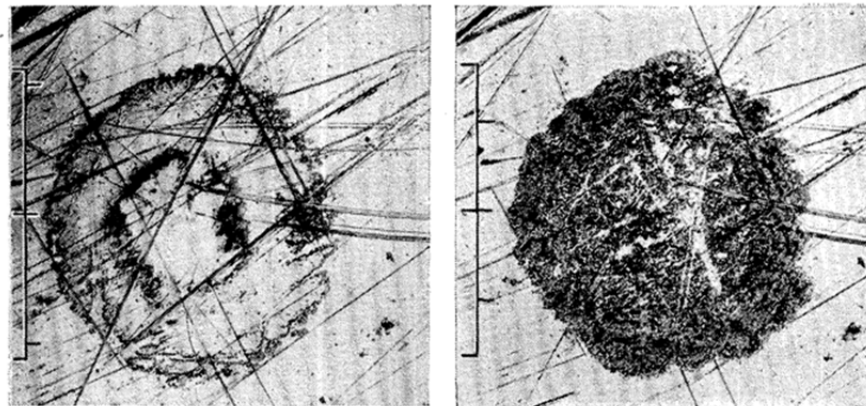
Figure 2.7: Effect of increased amplitude of fretting on fretting damage [13].

When the fretting contact is operating under the stick regime or conditions, no damage is observed. The crack propagation that leads to fretting fatigue is the dominant damage mechanism in the partial slip regime. Crack initiation and propagation are important in both fretting wear and fretting fatigue [28]. In the gross slip regime (or gross sliding) damage by wear dominates. An additional regime, called mixed fretting regime, is often included in this category and comprises a competition between crack (partial slip) and wear (gross slip) induced fretting damage [13].

Fouvry and the co-workers employed an energy approach to describe the formation of wear debris in the gross slip regime and they identified two additional wear regimes which are classified under the gross slip condition i.e. a low wear regime when the friction is low and high wear regime when friction is high. The low wear regime corresponds to the elastic or elastic shakedown situation, while the plastic deformation dominates in the high wear regime [29]. For transition from low wear and low friction to high wear and high friction, accumulative energy is required to plastically deform the subsurface layer into a tribological transformed layer (TTL) (alternatively is called " mechanically mixed layer") that further fretting cycle can disintegrate the TTL into the wear debris. Without having TTS at the contact, minimal fretting wear occurs due the asperity contact and friction is low (Fig. 2.8) [30].

It was suggested that more than 50 parameters can play a role in fretting wear and many of them are interdependent, the most important of these parameters include: slip amplitude, contact pressure, stress field in contact vicinity, number of cycles to fretting, materials, frequency, contact temperature and environment [31, 32].

26

Plastic deformation   Fully Transformed TTS

Fretting movement between ball & plate   Superficial fretting wear debris layer produced by TTS disintegration
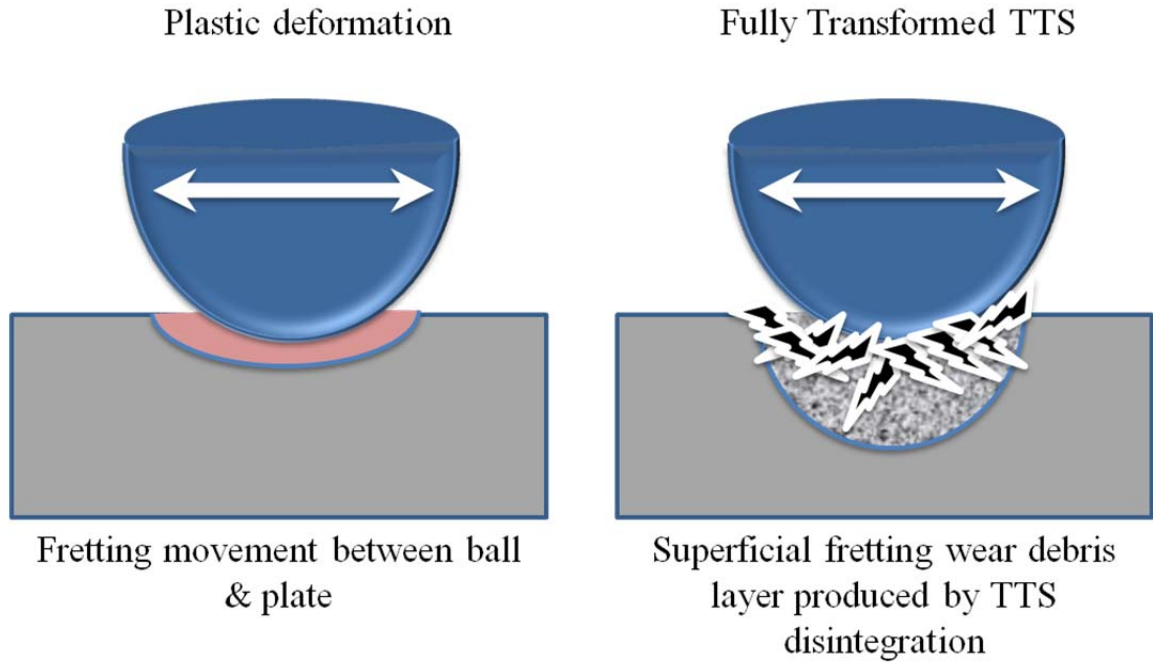
Figure 2.8: Schematic formation of tribological transformed structure in fretting [13].

It is generally accepted that the fretting wear rate (that is, the loss of material per unit of sliding distance per unit of applied normal load, and is measured by using profilometry) increases with increasing the slip amplitude. The sigmoidal curves represent the relationship between wear rates versus slip amplitude. At sliding amplitudes below 10-25µm, the wear rates are low and often constant and it increases linearly at moderate amplitude (20-100 µm) and at amplitudes above 100 µm it tends to become constant again [13, 26-28].

When the sliding amplitude is minute, the wear is entrapped for longer time in the contact and it can accommodate and support the interfacial loads and separate the two contacting surfaces, this leads to observation of low wear rate. The wear debris retention

in the contact is confined to the slip amplitudes below 25 μm for most cases. When the slip amplitude is constant the wear rate is found to be directly proportional to the applied load. The disruption in wear debris retention (includes adhesion, debris generation, debris trapping and debris elimination) mechanism can take place by application of higher frequency. Interfacial strain rate increases at higher frequencies which lead to increase the fretting and fatigue damage [13, 26, 28, 30, 32].

For metals, it is generally found that the oxygen and water accentuate fretting wear and surface damage, inert atmospheres such as nitrogen and argon suppress fretting of metals. The protective surface oxide film is continuously disrupted by fretting contact with the counterface and this will expose the fresh surface to the oxygen-containing atmosphere and causes further deterioration [28, 33].

Temperature may affect the fretting wear process in two ways. First, temperature usually increases the corrosion and oxidation rates, and second, temperature will change the mechanical properties of materials. Temperature can have a beneficial effect on both fretting wear and fretting fatigue. For instance in a metal-to-metal contact, if a thick, stable, adherent and mechanically strong oxide film forms on the surface, due to the temperature rise, the fretting wear rate usually decreases and fretting fatigue life increases. This film can act as a strong solid lubricant that prevents metal-to-metal contact and subsequently reduces the friction and surface damage [28]. The generated oxide films vary in thickness and morphology and are formed at different temperature for different materials.

In general, two approaches have been adapted so far to mitigate and prevent the fretting wear: (i) application of surface treatment such as coating and shot peening- in case of metallic substrate, and (ii) design optimization. Where, the aim of the latter is to modify the geometry of components in order to eliminate the excessive shear stress concentration at the interface. The efficiency of the former approach is reliant on the capabilities of coating technique in providing good adhesion between substrate and coating that prevents spallation of coating and extends the fatigue life of coating [13, 25, 26].

In the case of surface treatment to avoid fretting wear, it was shown that if the applied coating exhibits low-friction characteristic, the fretting fatigue can be reduced significantly[13,34]:

$$S_{fr} = S_0 - 2\mu P_0 [1 - e^{(-I/k)}] \tag{Eq.2.6}$$

Where S_{fr} is the fretting fatigue strength (MPa), S_0 is the fatigue strength in the absence of fretting (MPa), μ is coefficient of friction, P_0 is contact pressure (MPa), I is reciprocating amplitude(μm) and k is a constant , typically k=3.8 (μm) and for reciprocating amplitude greater than 25(μm), makes the exponential term negligible. According to Eq.2.6, application of low-friction coating can significantly enhance the fretting wear resistance of substrate, therefore application of lubricants seems to be a solution to minimize the fretting damage, but the problem is that lubricants are usually difficult to apply in fretting contacts because of the difficulty of maintaining the lubricant in the contact.

Tribological coatings such as sulphides, nitrides, selenides, diamond-like carbons (DLC), are known as potential solid lubricants due to their characteristic wear resistance and low friction. Reportedly, application of these coatings on the metallic substrates showed significant improvement in fretting wear behaviour [25, 32, 35, 36].

Determining the dominant wear mechanism is crucial in order to select the appropriate coating material and coating method. Various vacuum coating techniques have been extensively utilised to deposit foreign material to the surface, such as electro-deposition, plasma spray, ion implantation, physical vapour deposition (PVD) and chemical vapour deposition (CVD). But atomic layer deposition (ALD), which is a variant of CVD technique, showed proven capabilities in providing extremely conformal coating of elements, binary and ternary materials with precise and uniform thickness of desired [37].

2.2.3 Lubrication

The low shear strength layers of gas, liquid or solid are placed between the surfaces in contact to mitigate the frictional stresses and prevent wear. In the presence of extreme conditions such as elevated temperatures (above 500 ºC), space technology, ultra-high vacuum, high humidity, electrical conductivity or strong radioactivity, where liquid and gaseous lubricants are likely to degrade or decompose, the solid lubricants play the main role. For severe service conditions, it is essential that the solid lubricant exhibits thermal stability, oxidation stability, low volatility, chemical reactivity and adherence to substrate, effective at high loads and slow speeds [38]. The efficiency of the solid

lubricant in providing surface protection relies on the deposition method, since even most powerful lubricants will be easily scraped off by a wearing surface if the deposition method is not correct.

There is no single solid lubricant that can provide low friction and low wear over a broad range of temperature and environmental conditions. The major shortcomings of the solid lubricants can be listed as: (a) except for soft metal, solid lubricants exhibit poor thermal conductivity, therefore, they cannot carry away the heat from sliding interfaces, (b) their friction coefficient can be high or fluctuating considerably and this depends on the test environment and the test condition, (c) they have limited life-time and the replenishment is more difficult than the liquid lubricants [39]. To overcome these limitations novel coating architectures including multi-layers, micro-surface texturing, nano-structures and/or composites coatings have been developed.

Solid lubricity by different solid lubricants has various mechanisms. Lamellar solids such as graphite and metal dichalocogenides MX_2 (where M is molybdenum or tungsten and X is sulphur or selenium), exhibit anisotropy in their mechanical properties and their planes of low shear strength are sliding one over another at relatively low shear stresses and this interlamellar smooth sliding leads to low friction and self-lubricity (Fig.2.9(a)) [13]. Besides having weak bonding between lamellae, it is highly desirable that the solid lubricant presents good adhesion to the worn surface; otherwise it will be swept by the sliding action of counterface.

Second mechanism of solid lubrication is where a soft metal like silver, gold, indium and lead, is often deposited on a hard substrate. The hard substrate determines the contact area, regardless of the thickness of soft metal coating (Fig.2.9(b-d)) [18]. The shear strength of asperities in contact is determined by softer and weaker metallic film and this provides low friction. This mechanism is particularly useful for high vacuum applications, where the absence of oxygen allows the soft metallic particles to be repeatedly transferred between sliding surfaces. But soft metallic films are prone to flake off at very low temperature.

(a) Lamellar Crystal structure of the solid lubricant

(b) *A* small, τ large   (c) *A* Large, τ small   (d) *A* small, τ small
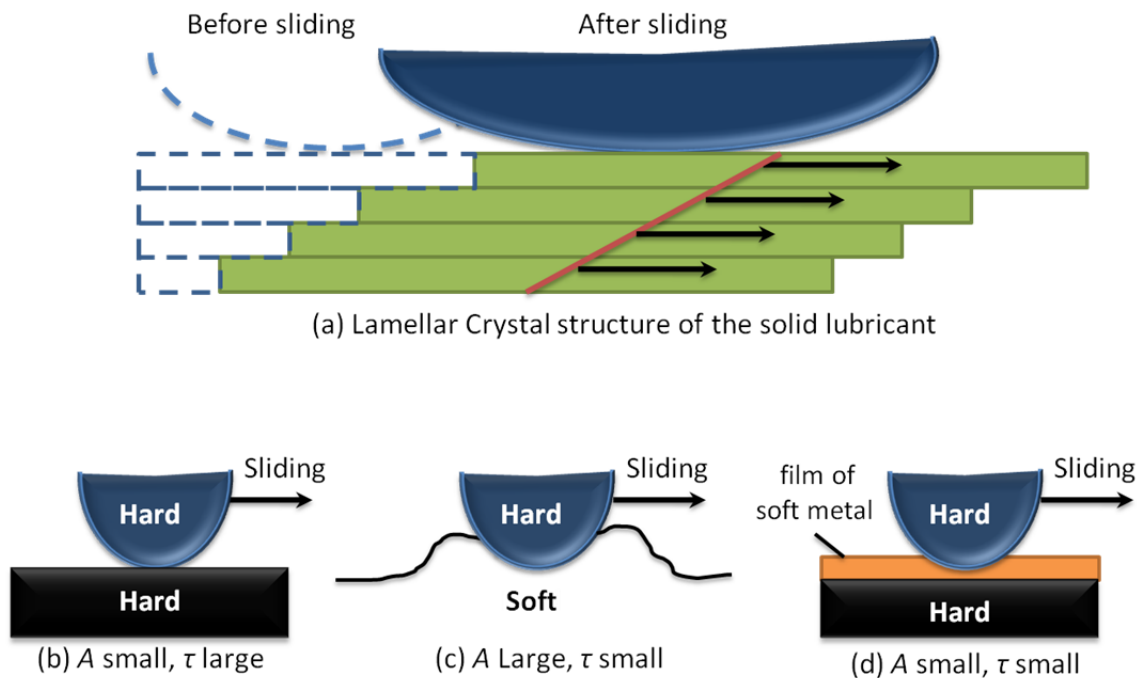
Figure 2.9: Mechanisms of solid lubrication (a) lamellar structure that provides low friction, (b-d) mechanism of friction reduction by application of a soft metallic film on the hard substrate, where *A* is the contact area and τ is interfacial shear strength [13].

Vacuum-based deposition techniques have been employed considerably to deposit solid lubricants, since contaminants, such as oxygen and water, are excluded in vacuum and the solid lubricant can be projected as a high-energy-plasma to the substrate. The significance of plasma deposition relies on deposition of individual atoms and ions of high energy on the surface which enhances the adhesion of the film as well as modification to its crystal structure. This eventually leads to longer life-time of the film [39-41]. It was reported that a 200nm film of sputtered molybdenum disulphide lasted more than five times longer than a 13 μm thick resin bonded disulphide film. The basic type of these coating systems includes PVD, CVD, ALD and ion implantation that are suitable for deposition of adaptive, self-lubricating thin films with composite or multilayered architectures.

2.2.4 Wear and Friction Behavior of Coated and Uncoated Carbon-Carbon Composites

It was outlined in section 2.1.1 that CCC is manufactured from carbon fibers of high elastic modulus and high strength embedded in a carbonaceous matrix. Depending on the processing parameters, the CCC's structure can include small, randomly oriented crystallites of graphite [1]. Within the a-b basal planes of hexagonal graphite, the atoms are bonded with strong covalent bonds, while in the c-direction there are very weak physical bonds (VDW) between the a-b basal planes. The lamellar structure provides low interfacial shear stress, which is why graphite is a good solid lubricant.

But the tribological behavior of the graphite is strongly dependent upon the environment and graphite is not an intrinsic solid lubricant. It was shown that under the

active environment rich in oxygen and water vapor, sliding friction coefficient of 0.02-0.1 was reported for polycrystalline graphite ball on the polycrystalline electro-graphite at load of 4N and sliding speed of 0.03-0.05 m/s [42]. During the abrasive wear test the dangling bonds are formed and this increases the friction coefficient, but water vapor and oxygen passivate these bonds and lead to friction mitigation, since their atoms insert themselves between the basal plane of hexagonal graphite and separate them by intercalation mechanism that facilitates the cleavage [43]. The presence of water vapor causes the re-orientation of graphite basal plane parallel to the sliding direction, and these crystallites constitute a smooth third-body on the entire sliding surface, which leads to pronounced decrease in friction coefficient and wear rate [44]. Graphite exhibited less decrease in friction in an inert gas environment, since the inert gas is unable to passivate the dangling bonds and the friction reduction is related to the atomic insertion which relies on the size and pressure of gas atoms.

Processing history of CCC, fibers architecture, wear test parameters (counterface, load, sliding speed, normal load, etc.) and environment factors (temperature, humidity, etc.), all will affect the tribological performance of CCC [45-47]. For instance, by increasing the frictional temperature the wear rate of CCC is increased due to the oxidation losses on the surface in contact and this leads to a transition of friction coefficient from low to high value. Application of tribological coatings that can be a good inhibitor to oxygen diffusion was shown to enhance the friction and wear performance of CCC [7, 43].

Tolde et. al. reported that 0.25-0.7 mm of pyrolytic carbon coating deposited on an unground CCC substrate can enhance the wear resistance considerably (wear rate = 78×10^{-9} mm^3/N.m) and the CCC which was ground by silicon carbide papers exhibited lowest friction coefficient ($\mu= 0.106$) [43]. Similarly, low friction coefficient and low wear rate was reported by infiltration of 4% of $MoSi_2$ into the CCC, this was related to the formation of an adherent interface between carbon fibers, matrix and $MoSi_2$ and formation of a lubricious tribolayer [7].

2.3 Oxide Ceramics

Oxide ceramics are the ionic compounds (made up of oxygen and metal) which exhibit superior strength, hardness, chemical and thermal resistance. The large difference in electronegativity between electronegative-oxygen and electropositive-metal(s) leads to strong bond, low density, high hardness, high elastic modulus, chemical inertness and preserving the mechanical properties at elevated temperature. Besides having limited number of slip systems, dislocation glide requires the charge disruption around cations and anions that results in breaking the bonds. This gives a rise to low fracture toughness character of oxides ceramics that is known as the main concern for engineering designs [48, 49].

Although the low fracture toughness has restricted the usages of oxide ceramics in structural applications, they have found significant attention in tribological aspects, such as ball bearings, mechanical seals, extrusion dies, cutting tools and prosthetic device [50]. Even in these applications the low fracture toughness leads to significant surface damage

and wear, therefore minimization and controlling the wear by tailoring the microstructure of oxide ceramics is the main challenge for materials engineers.

2.3.1 Tribological Characteristics of Bulk Oxide Ceramics

The term 'bulk' is given to ceramic oxides when they have grain size of more than one micron, various engineering applications using the oxide ceramics with this range of grain size. As it was indicated in the previous section, having few slip systems and large Burgers vector are the main reason to observe low fracture toughness in oxide ceramics. For tribological applications this can causes significant abrasive wear and surface damage [51].

Depending on the severity of the tribological contact, wear in ceramics is classified into 'mild' and 'severe' wear regimes [50, 52]. In the mild wear regime, a relatively thin and soft surface layer, which is mechanically delaminated from the surface as thin flakes, is formed due to the tribochemical reaction. In this regime the wear rate is less than 10^{-6} mm^3/ (Nm) and the surface roughness is smaller than the grain size. In the severe wear regime, which causes the failure, wear debris is formed due to the mechanical cracking of the grains and tribofilm delamination, the size of wear debris is comparable to the grain size of the ceramic and surface roughness is in the order of the grain size. The wear rate is higher than 10^{-6} mm^3/ (Nm).

Wear and friction can be modified significantly by formation of tribofilm (third-body) during the mild wear process, several mechanisms by Singer and co-workers were proposed to explain this behavior [53]: (a) the third-body can isolate the surfaces in

contact and this will reduce the wear, (b) the interfacial sliding between the third-body and the surfaces can mitigate the friction, (c) mitigation of the friction by third-body will affect the wear rate and the wear life and (d) depending on the contact, the third-body can be restored in and out of wear track and this leads into higher endurance.

The transition from mild wear to severe wear is recognized by an increase in wear rate and onset of brittle fracture on the surface. Various system properties such as speed, load, environment, time of operation etc. determine this transition, but the nature of the transition is clearly related to the fracture toughness of the ceramic. Rainforth proposed several strategies to improve the reliability of the engineering ceramics [50]: (a) a general reduction in microstructure scale, especially grain size and density, in order to reduce the size of defects within the materials; (b) formation of duplex structure such as nanocomposites, where one phase has a nano-scopic dimensions and (c) application of transformation toughening.

All of these three strategies were significantly investigated by Romanes [49] and Mensah [15], where the nano-structure of the atomic layer deposited monolayer toughened tetragonal-ZrO_2, bilayer wurtzite-ZnO/tetragonal-ZrO_2 and trilayer $ZnO/Al_2O_3/ZrO_2$ were in detail characterized and tailored as tribological coatings for MEMS device and steel bearings. But the main purpose of this research is to investigate the role of these solid lubricants in providing tribological enhancements and oxidation resistant for carbon-carbon composites. In the following chapters further details of tribological studies and characterization techniques that were employed to elucidate the underlying mechanisms on the surface and subsurface, will be presented.

2.3.2 Plastic Deformation Behavior of Nanocrystalline Oxides

Plastic flow can cause inelastic deformation in crystalline materials and this can lead to a large permanent and non-recoverable strain, known as plastic deformation. Plastic deformation is normally associated with dislocation slip (glide) and it occurs on particular crystallographic planes in well-defined directions that these crystallographic plane along with the crystallographic directions form a slip systems [54].

Dislocations are line defects that isolate the sheared portion of the crystal from unsheared portion. Fundamentally there two types of dislocation, edge and screw. Dislocations often have mixed character, which means they exhibit a combination of the pure edge and screw characteristics. Edge dislocations in general are often illustrated as an extra half plane of atoms, with dislocation line being at the termination of the half-plane. But edge dislocations are more complicated than just a single half-plane of atoms, since ceramics usually include two or more type of atoms and the associated unit of dislocation displacement, Burgers vector, is larger for ceramic in comparison to metals.

In the presence of applied shear stress, the edge dislocation will move parallel to the applied shear stress in the same direction as its Burgers vector and the screw dislocation will move perpendicular to the applied shear stress or perpendicular to its Burgers vector. The actual stress is required for dislocation to move (glide) along the slip plane is less than theoretical shear stress and is known as the Peierls-Nabarro stress (τ):

$$\tau = \mu ex\,p\left(-\frac{2\pi w}{b}\right) \hspace{5cm} \text{(Eq. 2.7)}$$

where μ is a material's constant and w is known as the dislocation width and b is the Burgers vector. The dislocation width (w) is primarily governed by the nature of atomic bonding and the crystal structure. In covalent solids, where the bonds are strong and highly directional, the dislocations are very narrow ($w\sim b$), in FCC metals the dislocations are wide ($w>10b$) and in ionic solids and BCC metals the dislocations are moderately narrow.

Since the dislocation activities within individual grain are constrained by the deformation of the adjacent grains, the plasticity in polycrystalline materials is substantially different and considerably difficult in comparison to single crystals. Hence, the plastic deformation in ceramics, that lacks sufficient number of slip systems and exhibit high Peierls-Nabarro stress, results in brittleness except under high extreme conditions of high stress or high temperature [51, 54]. Therefore, any mechanism that eases the plastic deformation in ceramics at low temperature and prevents the brittle fracture is demanding.

In ceramics the fracture toughness is not controlled by dislocation motion, since dislocations are either immobile or insufficient slip systems exist. Hence, fracture toughness of ceramics is directly governed by the microstructure on the crack tip. The toughening mechanisms of ceramic include the modification of the microstructure at the vicinity of the crack tip that alleviates the stress concentration at the crack tip. This is achievable by processes such as crack tip deflection/shielding and transformation toughening.

As was pointed out by Rainforth [50], the reliability of engineering ceramics can be increased by a general reduction in microstructural features, especially grain size and density. Similarly, in 1987 Karch and co-workers reported significant enhancement in plastic deformation behavior of TiO_2 and CaF_2 at ambient temperature, where polycrystalline ceramics with the crystal size of few nanometer (~1-10nm) was generated. In this case, the diffusional creep rate ($\dot{\varepsilon}$) of polycrystalline materials at low temperature, where the boundary diffusivity dominates, is given by:

$$\dot{\varepsilon} = B\sigma\Omega\delta D_b/d^3 kT \tag{Eq.2.8}$$

where B is a numerical constant, σ is the tensile stress, the Ω is the atomic volume, δ is the thickness of the boundaries, d is the average crystal size, D_b is the boundary diffusivity, T is the temperature and K is the Boltzmann's constant. The enhanced ductility was related to the (i) reduction of the crystalline size (d) and (ii) the enhanced boundary diffusivity (D_b) [55].

The mechanical softening at ambient temperature with decreasing the grain size to the nanostructured level was first observed experimentally by Chokshi and the co-workers in 1989 [56], and it was called inverse Hall-Petch effect. The classical Hall-Petch relationship expresses the variation in yield stress (σ) to the grain size of the material (d):

$$\sigma = \sigma_0 + fd^{-1/2} \tag{Eq.2.9}$$

where σ_0 is the lattice friction stress required to move individual dislocations and f is a constant, which is often referred to as the Hall-Petch slope and is material dependent. The

hardness of crystalline materials with grain size of larger than ~ 1μm complies very well with classical Hall-Petch relationship.

The analysis of the experimental Hall-Petch data in variety of materials revealed three different regions in the plot of σ versus $d^{-1/2}$, viz.: (i) a region from single crystal to a grain size of ~ 1 μm, where the classical Hall-Petch relationship is valid, (ii) a region for grain sizes spans from ~ 1 μm to ~ 30 nm, in this region the Hall-Petch relation almost holds, but deviates from the classical 0.5 exponent and approaches zero and (iii) a region beyond a small critical grain size, where the strength actually decreases with reduction in grain size [57].

Since Chokshi and co-workers used low density compacts (nanocrystalline Cu and Pd) and employed annealing to alter the grain size of these compacts, their observation of inverse Hall-Petch relationship was debated by other researchers [58]. Only limited number of non-controversial cases, all for metals, were reported as the inverse Hall-Petch relationship, such as laser ablated Zn, electrodeposited Ni, electrodeposited Ni tested by nanoscratch tester and pulsed laser deposited Cu (Table 1 of [59]). Grain boundary sliding that occurs by the diffusional creep in ultra fine grained materials at room temperature, which is akin to the well-known Coble creep, is known to be the mechanism responsible for inverse Hall-Petch relationship.

Besides the experimental observations, Padmanabhan et. al. [58] developed a model to explain the strain-rate dependent deformation in nanostructured materials, and accurately predicted the grain size dependence of hardness, where the inverse Hall-Petch relationship is observed. Similarly a computer simulation of the deformation of the

nanocrystalline copper revealed that the large number of sliding events of atomic planes at the grain boundaries is the major mechanism responsible for softening. It was shown that the dislocation activity at the grain boundaries play a minor role in the softening [60].

A sophisticated molecular dynamic simulation by Wolf and the co-workers theoretically showed that there is a transition from dislocation-based deformation (classical Hall-Petch relationship) to grain boundary-mediated deformation (inverse Hall-Petch) and the transition point is known by a critical grain size (crossover grain size, d_c) at which an alteration in the mechanical behavior from hardening to softening takes place [59]. By considering the transition of the classical Hall-Petch mechanism to the Coble creep mechanism at the critical crossover grain size (d_c), Pande and Masumura proposed a generalized form of yield stress applicable to any polycrystalline materials[57]:

$$\sigma = \sigma_0 + kd^{-1/2} + k_1 + B_0/d + Bd^3 \qquad\qquad \text{(Eq. 2.10)}$$

where K_1 and B_0 are constants and B is both temperature and strain rate dependent. By equating the first two terms ($\sigma_0 + kd^{-1/2}$), which signifies the classical hall-Petch and the last three term ($k_1 + B_0/d + Bd^3$), which represent the Coble creep, the critical crossover grain size is (d_c) obtainable. The breakdown for Hall-Petch hardening reported at $d_c = $ 12-14nm for electrodeposited nanocrystalline nickel by manifesting itself as an abrupt change in hardness data and the abrasive wear behavior [61]. For these ranges of grain size the average friction coefficient, which was measure by nanoscratch experiment, was 0.25± 0.01 and optical microscopy and atomic force microscopy

examinations of the wear track exhibited uniform and smoothed trenches with no particulate debris.

The breakdown in mechanical behavior can be utilized in order to develop nanostructured material that exhibit different properties than their bulk counterparts, for instance in tribological coating, where brittleness and fracture of the coating is a major issue, engineering a nanostructure can improve the wear and friction behavior significantly. Following section will explain how controlling the microstructure can lead into the good tribological properties.

2.3.3 Low-Temperature Lubricious Oxides

From lubrication perspective the major shortcoming with natural oxide is that they are brittle at ambient temperature, and they can only be lubricious and hinder the surface damage at elevated temperatures (> 0.5 T $_{melting}$). Various investigations have shown that microstructure engineering of oxide ceramics can lead into optimization of their tribological properties [55, 62]. For instance, in 1977, Prasad and Zabinski reported significant reduction in friction coefficient of pulsed laser deposited (PLD) ZnO (μ~0.2 for nanostructured PLD ZnO with (0001)- highly textured vs. μ~ 0.7 for hot pressed bulk ZnO with 1-2 μm grains of random orientation) by controlling the nanocrystalline grain structure and oxygen substoichiometry.

The underlying mechanism was explained in terms of enhanced grain boundary sliding that contributes to plastic deformation and low friction. Furthermore, the oxygen adsorption at the topmost layer improves the dislocation motion within ZnO which leads

to further reduction in friction coefficient by lowering the shear strength, therefore, the transfer film slide over each other with little wear [63].

Obviously nanostructured oxides exhibited considerable potential to be used as a solid lubricant at low temperature. One of the major applications of these oxides is in micro/nanoelectromechanical systems (MEMS/NEMS). Since MEMS/NEMS devices include high-aspect-ratio features, atomic layer deposition (ALD) by far is known as the best deposition technique for these applications that can enhances their reliability, wear resistance [64]. The capabilities of ALD in coating surface and subsurface porosities were applied in this research, where ALD infiltrated various solid lubricants into the CCC and the mechanisms of wear behavior were investigated.

2.4 Atomic Layer Deposition (ALD)

ALD with alternative name of atomic layer epitaxy (ALE) was originally developed in 1970s for fabrication of thin film electroluminescent (TFEL) flat panel display (e.g. ZnS:Mn and amorphous Al_2O_3 insulator films) [65]. ALD, as a variant of CVD, is a surface reaction with a self-limiting characteristic, in which the source vapors (precursor) are pulsed into the reactor sequentially, one at a time, and after certain dwell time in the reactor the byproduct are purged by an inert gas like nitrogen [66]; the reactions are separated by purging or evacuation. The resultant coating exhibits highly uniform thickness and excellent conformality especially advantageous for high aspect ratio structures. ALD is capable of depositing element, binary and ternary compounds [37, 67, 68].

44

For instance, to deposit a binary *XY* coating two half reactions (*A* and *B*) will generally take place: (i) pulsing of first precursor (*X*) into the reactor chamber, (ii) purge volatile byproducts, excess reactant and unreacted precursor from the reaction chamber, (iii) pulsing of the second precursor (*Y*), and (iv) purge or evacuation:

A reaction: surface $+X \rightarrow$ surface:X (Eq.2.11)

B reaction: surface: $X + Y \rightarrow$ surface:XY (Eq.2.12)

A schematic representation of reactions mechanism in ALD growth of TiN film was shown in Fig. 2.10, where including two self-limiting steps by using two different precursors ($TiCl_4$ and NH_3). The first half reaction provides metal (Ti) in the form of volatile inorganic complex and the second half reaction as a reducing, oxidizing, displacing or nitridation agent assists to remove the undesired ligands of the first precursor and providing the missing element for film growth [69].

Because of the self-limiting behavior of each *AB* ALD cycle, which is referred to growth per cycle (GPC), precise control of the film thickness, with subnanometer precision, is achievable by performing desired number of AB cycles. It was shown that the growth per cycle in ALD depends upon precursors that are employed, ALD processing temperature (150-400 ºC for most metal oxides) and sometimes sensitive to substrate materials. In this case, to achieve a low deposition temperature, very reactive precursors with completely self-limiting surface reactions are needed [70]. Where the ALD processing temperature plays a major role in the extent of the reaction and desorption of the ligands and byproducts, the substrate heating ensures reliable gas delivery and uniform growth rate.

The growth mechanisms in ALD were explained by derivation of a mathematical model as a function of the chemistry of the growth from the reactant compounds [71]. The chemisorptions growth may include two main mechanisms: (i) ligand exchange reaction, where the ligands are removed from the surface as a gaseous compound and (ii) dissociation and association, when all parts of the reactant are attached to the surface.

The ALD growth is not often proceeds in a one layer-per-cycle manner, since there can be limited number of reactive surface site in addition to the steric hindrances between bulky ligands in the chemisorptions layer and this can further reduces the growth rate and eventually lead into manner of self-saturation in ALD film growth [68]. Fong et. al. monitored the growth of ALD-ZnO by employing *in situ* synchrotron through a combination of x-ray reflectivity and x-ray fluorescence. It was found that amorphous ZnO films grow as islands, and after the tenth cycles of growth, the growth rate decreases from 4.2 to 3.0 Å per cycle and then it continues based on the self-saturation in a steady-state manner [72]. This growth mechanism was explained as a substrate-inhibited growth model and was observed for other ALD films such as Al_2O_3, ZrO_2 and HfO_2 [73].

(a) Pulsing of TiCl$_4$ precursor into the reaction chamber

(b) Purge of byproducts and unreacted compounds

(c) Pulsing of NH$_3$ precursor into the reaction chamber

(d) Purge of byproducts and unreacted compounds
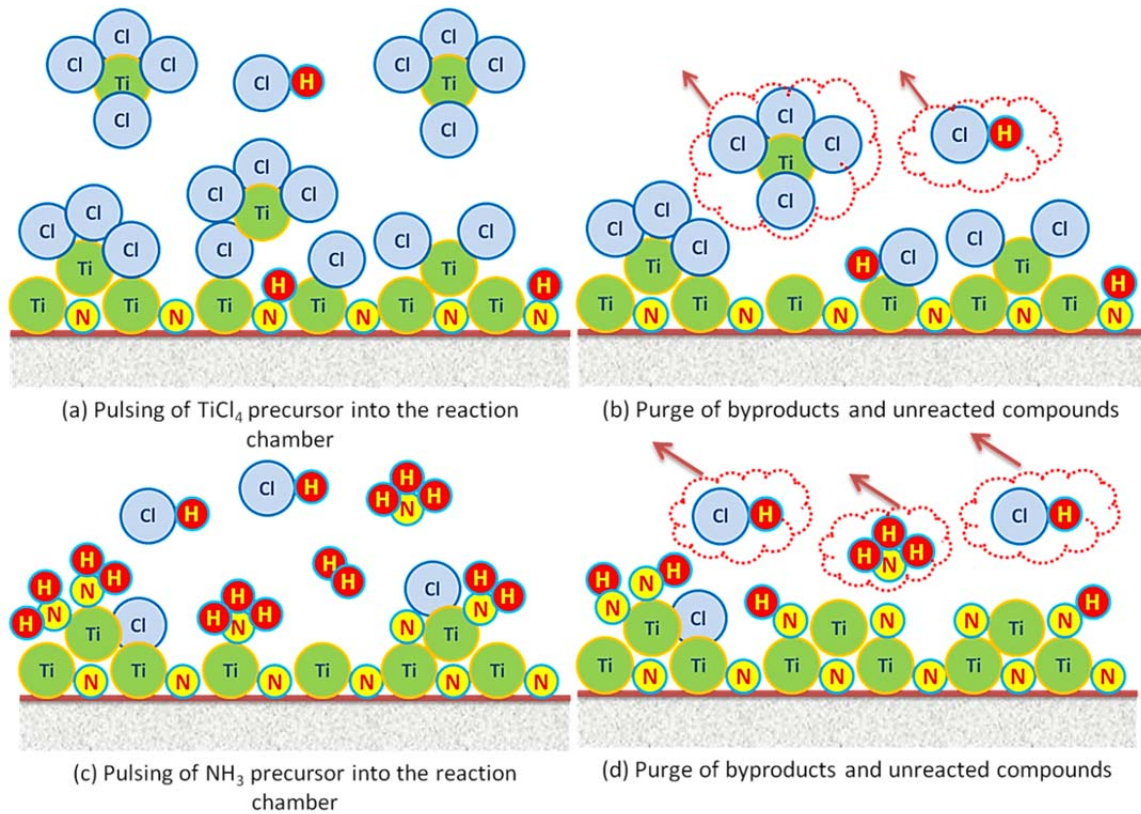
Figure 2.10: Schematic representation of atomic layer deposition of TiN [68].

The major limitations of ALD can be listed as:

- Long duration is required to deposit a thick film (typical GPC for monolayer is 100-300 nm.h^{-1}) and this is compensated by the large-area or large-batch deposition,

- No selective deposition,

- Growth chemistry is different from the nucleation chemistry,

- Lack of good and cost-effective ALD processes and compatible precursors for some important materials, e.g. metals, Si, SiO_2, Si_3N_4,, and several ternary and multicomponent materials, and

- The precursor vapor pressure which limits the types of reactant [37].

The low GPC rate in ALD is compensated with the diminution of devices and this makes the ALD competitive with other deposition techniques. The benefits of ALD include [68]:

- Producing highly conformal film with accurate thickness over the large area

- Large-batch compatibility,

- Insensitivity to non-uniform precursor vaporization rate,

- Precursor flux homogeneity is not required for self-limiting growth

- Good reproducibility,

- Straightforward scale-up by increasing the deposition cycles,

- Composition control down to atomic level,

- Possibility to interface modification

- Capability of producing sharp interfaces and superlattices,

- Lack of gas phase reactions which favors use of highly reactive precursors and leads to effective materials utilization,

- Low processing temperature, and

- Capability to prepare multilayer structures in a continuous manner due to having large processing temperature window

The achievement of abovementioned benefits requires appropriate chemistry fulfilling by proper selection of precursors. The properties required for ALD precursors are [68]:

- Optimized volatility for efficient vapor transportation,
- Resistant to self-decomposition,
- Aggressive and complete reaction to ensure fast completion of surface reactions in short cycle of time,
- No etching of the film and substrate, or dissolution into the film or substrate,
- Unreactive volatile byproducts,
- Sufficient purity
- Inexpensive, easy to synthesis and handle, nontoxic and environmentally friendly

2.4.1 ALD ZnO

Because of the interesting electrical, optical and piezoelectric properties, thin films of wurtzite structured wide band gap ZnO have numerous applications like chemical sensors, light emitting diodes, surface acoustic wave device, display panel and transparent conducting electrodes for solar cells. Deposition techniques such as CVD, PVD, ALD, electron beam evaporation, reactive magnetron, sol-gel and recently plasma-enhanced ALD are employed to deposit thin films of ZnO [74-76]. Diethyl zinc $(Zn(C_2H_5)_2)$ (DEZ) and H_2O are the most commonly used precursors to deposit thin film

of ZnO with atomic layer deposition. In this case, Zn- and O- containing molecules react with available surface nucleation sites sequentially and exhibit excellent self-saturation ALD mechanism to grow ZnO, according to these two half reactions:

A: $ZnOH* + Zn(CH_2CH_3)_2 \rightarrow ZnOZn(CH_2CH_3)* + C_2H_{6(g)}$ (Eq.2.13)

B: $ZnOZn(CH_2CH_3)* + H_2O \rightarrow ZnOH* + C_2H_{6(g)}$ (Eq.2.14)
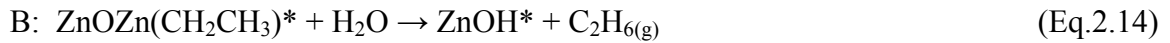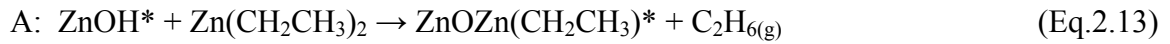
The asterisks indicate the surface species, By using the same precursor, it was shown that the resulting microstructure for ALD ZnO is wurtzite structure (Fig. 2.11 [77])with (100) orientation for low ALD growth temperature and (002) preferred orientation at substrate temperature above 200 ºC [74, 78-80].
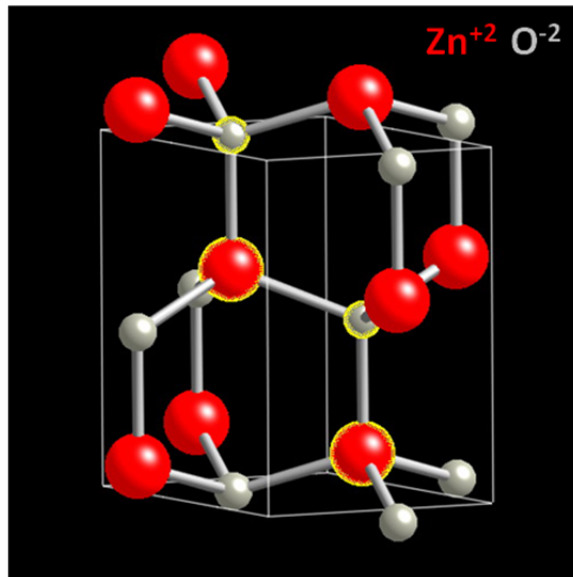
Figure 2.11: Wurtzite structure of ZnO,
space group # 186: P6$_3$mc [73].

2.4.2 ALD Al_2O_3

Trimethylaluminum (TMA) (Al $(CH_3)_3$), the most commonly used aluminum source in ALD, and water are the metal and oxidant precursors respectively used to grow ALD-Al_2O_3. TMA and H_2O are highly reactive and this makes the TMA/H_2O as an ideal case which results in high growth rate (GPC ~ 30-40% of a monolayer). In this case the reactions are self-terminating and the reaction byproduct is methane (CH_4) that is rather inert and does not interfere with the growth [81, 82]:

A: $OAlOH^* + Al(CH_3)_3 \rightarrow OAl(CH_3)^* + CH_4(g)$ (Eq.2.15)

B: $OAl(CH_3)^* + H_2O \rightarrow OAlOH^* + CH_4(g)$ (Eq.2.16)
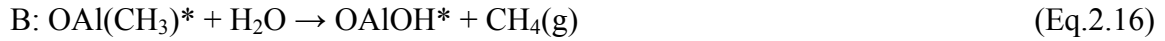
The asterisks represent the surface species. Growth mechanism involved in above reaction is ligand exchange and the growth rate (GPC) was found to be linearly related to the concentration of surface reactive sites (OH-groups) [81]. It was shown that increasing the processing temperature reduces the OH-groups concentration and in the absence of hydroxyls groups, dissociation/association will be the dominant growth mechanism. The deposition temperature for ALD Al_2O_3 is normally below 300 ºC, which results in amorphous microstructure.

2.4.3 ALD ZrO_2

Due to the high relative dielectric constant, ZrO_2 is used in electronic devices as a dielectric, such as metal-oxide-semiconductors (MOS), and because of its wide band gap and high refractive index it has variety of applications in optical coatings. The performance of any device which is based on ZrO_2 is reliant on the crystal structure of

ZrO$_2$. It exists in the four crystalline polymorphs of monoclinic (m), tetragonal (t), and cubic(c) and orthorhombic (o) (Fig. 2.12). The m-, t- and c-ZrO$_2$ are known as the low pressure polymorphs, while the o-ZrO$_2$ is stable at high pressures (10-42GPa: orthorhombic I, II and III). Table 1 displays the crystal structure and lattice parameter associated with each of these polymorphs. Among these three phases the monoclinic phase has the lowest density, the phase transformation takes place at these temperature ranges [83, 84]:

$$m - ZrO_2 \xleftrightarrow{1400K} t - ZrO_2 \xleftrightarrow{2570K} c - ZrO_2 \xleftrightarrow{2980K} Melt \qquad \text{(Eq.2.17)}$$
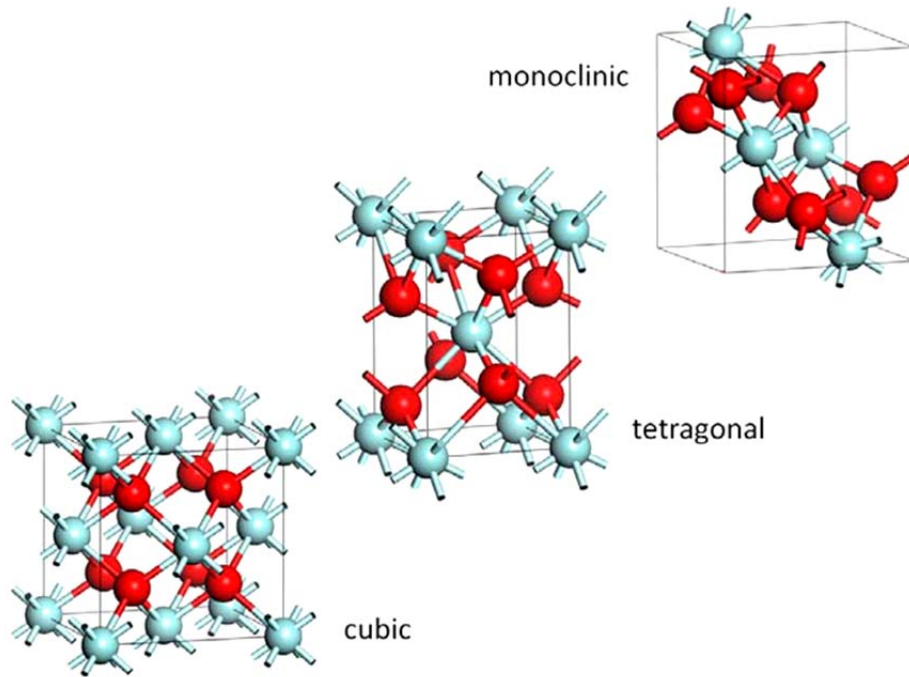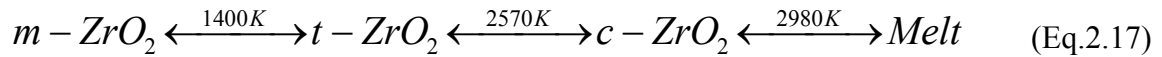
Figure 2.12: Low-pressure polymorphs of ZrO$_2$, Where red and blue spheres represent oxygen and zirconium atoms respectively [courtesy of Jincheng Du, The University of North Texas].

An important concept which is often utilized in zirconia ceramics is to alloy pure ZrO$_2$ with another oxide, such as MgO (magnesia), CaO (calcia) and rare earth (RE)

oxides such as Y_2O_3 (yttria) and CeO (ceria), to fully or partially stabilize high temperature polymorphs (c and t) of ZrO_2 to lower temperatures. The volume expansion associated with the tetragonal to monoclinic transformation can be used to advantage for improving toughness and strength. For instance tetragonal zirconia can transform to monoclinic under the influence of a crack tip stress and this transformation may cause the crack tip to deflect and this leads to significant toughening [83, 85]. Making structure of small grains [86], growing as a thin film [83, 87] and using substoichiomeric compositions [88] are other ways of stabilizing t- zirconia.

Studies showed that ALD is capable of producing t-ZrO_2 and c-ZrO_2 that are stable at room temperature and in this case, the structure of ALD-ZrO_2 is highly dependent upon precursors used, growth temperature and film thickness [91, 92]. For instance, Romanes [49] used Tetrakis (dimethylamido) Zirconium (IV) and DI H_2O as ALD precursors to deposit ZrO_2 at temperature window of 200-350ºC, according to the following reactions:

A: $ZrOH^* + Zr(NC_2H_6)_4 \rightarrow ZrOZr(NC_2H_6)^* + NC_2H_7(g)$ (Eq.2.18)

B: $ZrOZr(NC_2H_6)^* + H_2O \rightarrow ZrOH^* + NC_2H_7(g)$ (Eq.2.19)
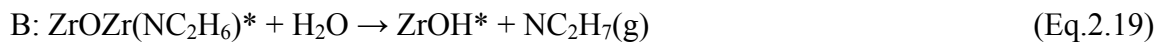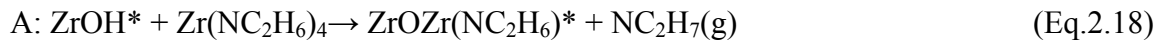
Where asterisks designate the surface species, it was found that the tribological performance of the ALD- ZrO_2 is reliant on the growth temperature and the film which was grown at 250 ºC and obtained tetragonal crystal structure, exhibited lowest friction and lowest wear. The reason for such a superior behavior was related to the small grain size and high ratio of the (101) tetragonal to (110) tetragonal grain orientations.

Table 2.1: Low-pressure polymorphs of ZrO_2 and associated unit cell and physical properties [49,89,90]

Property		Monoclinic ZrO_2	Tetragonal ZrO_2	Cubic ZrO_2
Lattice Parameters (Å)	a	5.098	5.037	5.034
	b	5.171	5.037	5.034
	c	5.264	5.113	5.034
Temperature (K)		<1400	1400-2570	2570-2980
Coordination		Zr=7, O_1=3, O_2=4	Zr=8, O_1=4, O_2=4	Zr=8, O_1=4, O_2=4
Volume ($Å^3$)		136.77	129.73	127.57
Density (g/cc)		5.814	6.172	6.17
Space Group		$P2_1/c$	$P4_2/nmc$	Fm3m

2.5 Chapter References

1.   Doğan, C.P., *Properties and Performance of Ceramic-Matrix and Carbon-Carbon Composites* ASM Handbooks Online, 2003. 21.

2.   Devi, G.R.a.R.R., K., *Carbon-Carbon Composites -An Overview.* Defence Science Journal, 1993. 43(4): p. 369-383.

3.   Bacos, M.P., *Carbon-carbon composites : oxidation behavior and coatings protection.* Le Journal de Physique IV, 1993. 03(C7): p. C7-1895-C7-1903.

4.   Sheehan, J.E., Buesking, K. W. , and Sullivan, B. J. , *Carbon-Carbon Composites.* Annual Review of Materials Science, 1994. 24: p. 19-44.

5.   Huang, J., et al., *Oxidation resistant yttrium silicates coating for carbon/carbon composites prepared by a novel in-situ formation method.* Ceramics International, 2007. 33(5): p. 887-890.

6.   Lobiondo, N.E., L.E. Jones, and A.G. Clare, *Halogenated glass systems for the protection of structural carbon-carbon composites.* Carbon, 1995. 33(4): p. 499-508.

7.   Park, S.-J., M.-K. Seo, and J.-R. Lee, *Effect of oxidation inhibitor on the low energy tribological behavior of carbon-carbon composites.* Carbon, 2002. 40(6): p. 835-843.

8.   Jian-Feng, H., et al., *Mullite-Al_2O_3-SiC oxidation protective coating for carbon/carbon composites.* Carbon, 2003. 41(14): p. 2825-2829.

9.   Luthra, K.L., *Oxidation of carbon/carbon composites--a theoretical analysis.* Carbon, 1988. 26(2): p. 217-224.

10. Manocha, L.M., *High performance carbon–carbon composites.* Sadhana, 2003. 28(1&2): p. 349-358.

11. Morimoto, T., et al., *Multilayer coating for carbon-carbon composites.* Carbon, 1995. 33(4): p. 351-357.

12. Smeacetto, F., *Multilayer coating with self-sealing properties for carbon–carbon composites.* Carbon, 2003. 41(11): p. 2105-2111.

13. Stachowiak, G.W.a.B., Andrew W. , *Engineering Tribology*. 3 ed, ed. Elsevier2006.

14. Larsen-Basse, J., *Solid friction*, in *ASM Handbook 18: Friction, Lubrication, and Wear Technology*1992, ASM International.

15. Mensah, B.A., *Growth, structure and tribological properties of atomic layer deposited lubricious oxide nanolaminates*, in *Department of Materials Science and Engineering*2010, University of North Texas: Denton.

16. De Celis, B., *Theoretical analysis of dry friction in brittle and ductile materials.* Wear, 1987. 116(3): p. 287-298.

17. Krim, J., *Resource Letter: FMMLS-1: Friction at macroscopic and microscopic length scales.* American Journal of Physics, 2002. 70(9): p. 890-897.

18. Bowden, F.P.a.T., D. , *The Friction and Lubrication of Solids*. Vol. Part 1. 1986: Clarendon, Oxford.

19. Padture, N.P., *Hertzian Contacts*, in *Encyclopedia of Materials: Science and Technology*2001. p. 3750-3752.

20. Bhushan, B., *Nanoscale tribophysics and tribomechanics.* Wear, 1999. 225: p. 465-492.

21. Hogmark, S., S. Jacobson, and O. Vingsbo, *Surface Damage.* ASM Handbook 18: Friction, Lubrication, and Wear Technology. Vol. 18. 1992: ASM International.

22. Matthews, A., S. Franklin, and K. Holmberg, *Tribological coatings: contact mechanisms and selection.* Journal of Physics D-Applied Physics, 2007. 40(18): p. 5463-5475.

23. Tylczak, J.H., *Wear: Abrasive Wear*, in *ASM Handbook 18: Friction, Lubrication, and Wear Technology*1992.

24. Ludema, K.C., *Sliding and Adhesive Wear*, in *ASM Handbook 18: Friction, Lubrication, and Wear Technology*1992, ASM International.

25. Holmberg, K. and A. Matthews, *Coatings tribology*2009: Elsevier. 560.

26. Waterhouse, R.B., *Fretting Wear*, in *ASM metals handbook volume frictio lubrication and wear technology*1992, ASM International.

27. Berthier, Y., L. Vincent, and M. Godet, *Fretting fatigue and fretting wear.* Tribology International, 1989. 22(4): p. 235-242.

28. Bill, R.C., *Fretting Wear and Fretting Fatigue—How Are They Related?* ASME Journal of Lubrication Technology, 1983. 105(2): p. 230-238.

29. Fouvry, S., P. Kapsa, and L. Vincent, *An elastic-plastic shakedown analysis of fretting wear.* Wear, 2001. 247(1): p. 41-54.

30. Sauger, E., et al., *Tribologically transformed structure in fretting.* Wear, 2000. 245(1-2): p. 39-52.

31.   Beard, J., *An investigation into the mechanisms of fretting fatigue*, in *University of Salford*1982.

32.   Berthier, Y., et al., *Fretting Wear Mechanisms and Their Effects on Fretting Fatigue.* Journal of Tribology, 1988. 110(3): p. 517-524.

33.   Waterhouse, R.B., *Fretting Corrosion*1972, Oxford: Pergamon Press.

34.   Nishioka, K. and K. Hirakawa, *Fundamental Investigations of Fretting Fatigue : (Part 5, The Effect of Relative Slip Amplitude).* Bulletin of JSME, 1969. 12(52): p. 692-697.

35.   Korsunsky, A.M., A.R. Torosyan, and K. Kim, *Development and characterization of low friction coatings for protection against fretting wear in aerospace components.* Thin Solid Films, 2008. 516(16): p. 5690-5699.

36.   Fouvry, S., P. Kapsa, and L. Vincent, *Fretting behaviour of hard coatings under high normal load.* Surface and Coatings Technology, 1994. 68-69: p. 494-499.

37.   Doll, G.L., et al., *Chemical Vapor Deposition and Atomic Layer Deposition of Coatings for Mechanical Applications.* Journal of Thermal Spray Technology, 2010. 19(1/2): p. 510-516.

38.   Jentgen, R., *Solid Lubricants: How They Work and Where to Use Them.* Parts, Hybrids, and Packaging, IEEE Transactions on, 1971. 7(2): p. 86-93.

39.   Donnet, C. and A. Erdemir, *Historical developments and new trends in tribological and solid lubricant coatings.* Surface and Coatings Technology, 2004. 180-181: p. 76-84.

40. Spalvins, T., *Friction Charactristics of Sputtered Solid Film Lubricants*, in *NASA TM X-5281*1970.

41. Chhowalla, M. and G.A.J. Amaratunga, *Thin films of fullerene-like MoS$_2$ nanoparticles with ultra-low friction and wear.* Letters to Nature, 2000. 407(6801): p. 164-167.

42. Zaïdi, H., et al., *Correlation between the tribological behaviour of graphite and its mechanical properties versus the interplan distance.* Applied Surface Science, 1993. 70-71(Part 1): p. 103-108.

43. Tolde, Z., V. Stary, and T. Kubart, *Tribological Properties of Carbon-Carbon Composite and of a Surface Layer of Pyrolytic Carbon.* Ceramics-Silikáty, 2008. 52(1): p. 37-44

44. Zaïdi, H., H. Néry, and D. Paulmier, *Stability of lubricating properties of graphite by orientation of the crystallites in the presence of water vapour.* Applied Surface Science, 1993. 70-71(Part 1): p. 180-185.

45. Awasthi, S. and J.L. Wood, *C/C composite materials for aircraft brakes.* Adv Ceram Mater 1988. 3: p. 449-451.

46. Gouider, M., et al., *Mass spectrometry during C/C composite friction: carbon oxidation associated with high friction coefficient and high wear rate.* Wear, 2004. 256(11-12): p. 1082-1087.

47. Venkataraman, B. and G. Sundararajan, *The influence of sample geometry on the friction behaviour of carbon-carbon composites.* Acta Materialia, 2002. 50(5): p. 1153-1163.

48. De Graef, M. and M.E. McHenry, *Structure of Materials: An Introduction to Crystallography, Diffraction and Symmetry* 2007.

49. Romanes, M.C., *Structure and Low-Temperature Tribology of Lubricious Nanocrystaline ZrO_2 Monofilms and ZnO/Al2O3 Nanolaminates Grown by Atomic Layer Deposition*, in *Department of Materials Science & Engineering* 2008, University of North Texas: Denton.

50. Rainforth, W.M., *The wear behaviour of oxide ceramics-A Review.* Journal of Materials Science, 2004. 39(22): p. 6705-6721.

51. Wiederhorn, S.M., *Brittle Fracture and Toughening Mechanisms in Ceramics.* Annual Review of Materials Science, 1984. 14: p. 373-403.

52. Kato, K. and K. Adachi, *Wear of advanced ceramics.* Wear, 2002. 253(11-12): p. 1097-1104.

53. Singer, I.L., et al., *Role of Third Bodies in Friction and Wear of Protective Coatings.* J. Vacuum Science and Technology A, 2003. 21(5): p. 232-240.

54. Green, D.J., *An Introduction to the Mechanical Properties of Ceramics* 1998: Cambridge University Press.

55. Karch, J., R. Birringer, and H. Gleiter, *Ceramics ductile at low temperature.* Nature, 1987. 330(6148): p. 556-558.

56. Chokshi, A.H., et al., *On the validity of the hall-petch relationship in nanocrystalline materials.* Scripta Metallurgica, 1989. 23(10): p. 1679-1683.

57. Pande, C.S. and R.A. Masumura, *Grain growth and deformation in nanocrystalline materials.* Materials Science and Engineering: A, 2005. 409(1-2): p. 125-130.

58. Padmanabhan, K.A., et al., *Inverse Hall-Petch effect and grain boundary sliding controlled flow in nanocrystalline materials.* Materials Science and Engineering: A, 2007. 452-453: p. 462-468.

59. Wolf, D., et al., *Deformation of nanocrystalline materials by molecular-dynamics simulation: relationship to experiments?* Acta Materialia, 2005. 53(1): p. 1-40.

60. Schiotz, J., F.D. Di Tolla, and K.W. Jacobsen, *Softening of nanocrystalline metals at very small grain sizes.* Nature, 1998. 391(6667): p. 561-563.

61. Schuh, C.A., T.G. Nieh, and T. Yamasaki, *Hall-Petch breakdown manifested in abrasive wear resistance of nanocrystalline nickel.* Scripta Materialia, 2002. 46(10): p. 735-740.

62. Prasad, S.V. and J.S. Zabinski, *Tribological behavior of nanocrystalline zinc oxide films.* Wear, 1997. 203-204: p. 498-506.

63. Zabinski, J.S., et al., *Lubrication using a microstructurally engineered oxide: performance and mechanisms.* Tribology Letters, 2000. 8(2): p. 103-116.

64. Hoivik, N.D., et al., *Atomic layer deposited protective coatings for micro-electromechanical systems.* Sensors and Actuators A: Physical, 2003. 103(1-2): p. 100-108.

65. SuntolaT. and A. J., *Method for producing compound thin films* U. Patent, Editor 1977.

66.	Elam, J.W., M.D. Groner, and S.M. George, *Viscous flow reactor with quartz crystal microbalance for thin film growth by atomic layer deposition.* Review of Scientific Instruments, 2002. 73(8): p. 2981-2987.

67.	Leskelä, M. and M. Ritala, *Atomic layer deposition (ALD): from precursors to thin film structures.* Thin Solid Films, 2002. 409(1): p. 138-146.

68.	Ritala, M. and M. Leskelä, *Atomic layer deposition*, in *Handbook of Thin Films*, N. Hari Singh, M.Sc, and Ph.D, Editors. 2002, Academic Press: Burlington. p. 103-159.

69.	Tiznado, H., et al., *Mechanistic details of atomic layer deposition (ALD) processes for metal nitride film growth.* Journal of Molecular Catalysis A: Chemical, 2008. 281(1-2): p. 35-43.

70.	Hausmann, D.M., et al., *Atomic Layer Deposition of Hafnium and Zirconium Oxides Using Metal Amide Precursors.* Chemistry of Materials, 2002. 14(10): p. 4350-4358.

71.	Puurunen, R.L., *Growth Per Cycle in Atomic Layer Deposition: A Theoretical Model.* Chemical Vapor Deposition, 2003. 9(5): p. 249-257.

72.	Fong, D.D., et al., *In situ synchrotron x-ray characterization of ZnO atomic layer deposition.* Applied Physics Letters, 2010. 97(19): p. 191904.

73.	Puurunen, R.L. and W. Vandervorst, *Island growth as a growth mode in atomic layer deposition: a phenomenological model.* Journal of Applied Physics, 2004. 96(Copyright 2005, IEE): p. 7686-95.

74.   Keun Kim, S., et al., *Comparison between ZnO films grown by atomic layer deposition using H$_2$O or O$_3$ as oxidant.* Thin Solid Films, 2005. 478(1-2): p. 103-108.

75.   Kim, D., et al., *The properties of plasma-enhanced atomic layer deposition (ALD) ZnO thin films and comparison with thermal ALD.* Applied Surface Science, 2011. 257(8): p. 3776-3779.

76.   King, D.M., et al., *Low-temperature atomic layer deposition of ZnO films on particles in a fluidized bed reactor.* Thin Solid Films, 2008. 516(23): p. 8517-8523.

77.   De Graef, M. and M.E. McHenry, *Appendix 1:Crystal Structure Descriptions*, in *Structure of Materials: An Introduction to Crystallography, Diffraction and Symmetry* 2007, Cambridge University Press.

78.   Lujala, V., et al., *Atomic layer epitaxy growth of doped zinc oxide thin films from organometals.* Applied Surface Science, 1994. 82-83: p. 34-40.

79.   Yousfi, E.B., J. Fouache, and D. Lincot, *Study of atomic layer epitaxy of zinc oxide by in-situ quartz crystal microgravimetry.* Applied Surface Science, 2000. 153(4): p. 223-234.

80.   Pung, S.-Y. and et al., *Preferential growth of ZnO thin films by the atomic layer deposition technique.* Nanotechnology, 2008. 19(43): p. 435609.

81.   Puurunen, R.L., *Surface chemistry of atomic layer deposition: A case study for the trimethylaluminum/water process.* Journal of Applied Physics, 2005. 97(12): p. 52.

82.	Burgess, D.R., et al., *Atomic Layer Deposition — Process Models and Metrologies.* AIP Conference Proceedings, 2005. 788(1): p. 141-146.

83.	Kukli, K., et al., *Atomic layer deposition of zirconium oxide from zirconium tetraiodide, water and hydrogen peroxide.* Journal of Crystal Growth, 2001. 231(1-2): p. 262-272.

84.	Leger, J.M., et al., *Pressure-induced structural phase transitions in zirconia under high pressure.* Physical Review B, 1993. 47(21): p. 14075.

85.	Banerjee, S. and P. Mukhopadhyay, *Phase transformations: examples from titanium and zirconium alloys*. 1 ed2007: Elsevier Science.

86.	Vollath, D., et al., *Phases and phase transformations in nanocrystalline ZrO_2.* Journal of Nanoparticle Research, 2006. 8(6): p. 1003-1016.

87.	Tkachev, S.N., et al., *Micro-Raman spectroscopy and X-ray diffraction studies of atomic-layer-deposited ZrO_2; and HfO_2 thin films.* Journal of Materials Science, 2005. 40(16): p. 4293-4298.

88.	Djuricic, B., et al., *The properties of zirconia powders produced by homogeneous precipitation.* Ceramics International, 1995. 21(3): p. 195-206.

89.	Zhao, X. and D. Vanderbilt, *Phonons and lattice dielectric properties of zirconia.* Physical Review B, 2002. 65(7): p. 075105.

90.	Zhao, X., D. Ceresoli, and D. Vanderbilt, *Structural, electronic, and dielectric properties of amorphous ZrO_2 from ab initio molecular dynamics.* Physical Review B, 2005. 71(8): p. 085107.

91.   Aarik, J., et al., *Growth kinetics and structure formation of ZrO$_2$ thin films in chloride-based atomic layer deposition process.* Thin Solid Films, 2002. 408(1-2): p. 97-103.

92.   Kukli, K., et al., *Influence of thickness and growth temperature on the properties of zirconium oxide films grown by atomic layer deposition on silicon.* Thin Solid Films, 2002. 410(1-2): p. 53-60.

CHAPTER 3

EXPERIMENTAL PROCEDURE

3.1 Substrate Preparation

Samples of carbon-carbon composite (CCC) consisting of ~40% amorphous carbon and ~60% graphite, supplied by Poco Graphite Inc., were used for this investigation. Table 3.1 represents the summary of the physical and mechanical properties of this composite. An important criterion in designing a coating system is an appropriate match between coefficient of thermal expansion (CTE) of the substrate and the coating [1]. As shown in Table 3.1, the CTE of CCC ($7.6 \times 10^{-6}/°C$) is in the proximity of the CTE of tetragonal zirconia ($5\text{-}10 \times 10^{-6}/°C$) and, therefore [2, 3], less mismatch and decohesion is anticipated at the interface of ZrO_2 coating and the carbonaceous substrate.

Diamond saw, Techcut 4^{TM} from ALLIED High Tech Products Inc. at the low speed of 50-100 RPM was employed to dry-section samples of CCC prior to deposition. All the fixtures, which were used to hold the sample in the sectioning position, were degreased by using acetone and methanol to remove any residual of cutting oil and other contaminants. Following the sectioning, the CCC samples were cleaned by using the high purity nitrogen gas blow to remove all the loose debris and weakly bonded particles from the surfaces.

Approximately 1in x 1in pieces of (100) silicon wafer were degreased by using Cole-Parmer ultrasonic cleaner (EW-08891-01), each for a 10-minutes-cycle of: acetone, methanol and deionized water, followed by blasting of a high purity nitrogen gas. The

silicon wafer pieces were positioned at the vicinity of each CCC sample in the ALD reactor and used for calibration of ALD parameters and subsequent characterization such as thin-film thickness measurement with ellipsometer and phase identification of coatings with x-ray diffraction.

Table 3.1: Physical and mechanical properties of carbon-carbon composite [4]

Particle size (µm)	5	Tensile strength (N/mm^2)	69
Pore size (µm)	0.8	Modulus of Elasticity (N/mm^2)	11000
Total Porosity (%)	21	Tensile strain to failure (%)	0.62
Open porosity (%)	75	Hardness (HRC)	67
Apparent Density (g/cc)	1.77	Electrical resistivity (µ.Ohm.cm)	2460
Compressive strength (N/mm^2)	186	Coefficient of Thermal Expansion (micron/m) ° C	7.6
Flexural strength (N/mm^2)	97	Thermal conductivity (Watt/m K)	60

3.2 ALD Film Deposition

CCC samples and pieces of (100) silicon wafer were loaded into the reactor chamber of the atomic layer deposition (ALD) system, a Cambridge Nano Tech Savannah 100 (Fig. 3.1[5]), which was controlled by Savannah10 ALD software. The reactor design is similar to the ALD viscous flow hot wall reactor that was developed by Elam et.al [6]. The ALD deposition parameters were considered for deposition of monolayer of ~200nm ZrO_2 (depositions 1 and 2) and trilayers of $ZnO/Al_2O_3/ZrO_2$ with the total thickness of ~200nm (depositions 3, 4 and 5) are shown in Tables 3.2 and 3.3 respectively. A total of five depositions were conducted on CCC samples by using ALD. The deposition variable parameters in ALD include type of precursor, deposition temperature, pulse and exposure time of precursor, purging time of byproducts, number of cycles, nitrogen flow rate, inner disk/substrate and the outer disk temperature were all

controlled by the Savannah software. The base pressure for abovementioned five depositions was maintained between 0.5 to 0.9 torr, the precursor valve temperature was set at 120 ºC, stop valve tee temperature was set at 150 ºC and bellows temperature was 150 ºC.
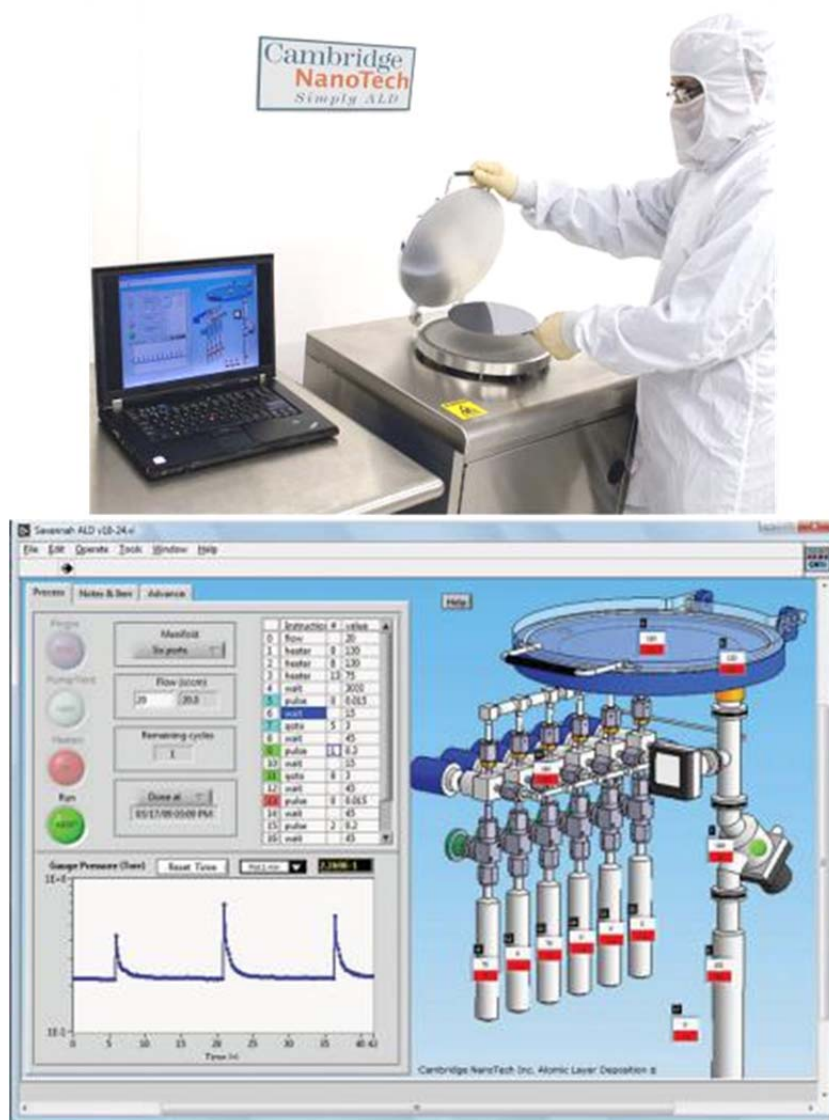
Figure 3.1: ALD system Savannah S200 and the Savannah software interface.

Table 3.2: Two sets of ALD deposition parameters to deposit ~ 200nm monolayer of ZrO_2 (P=pulse, E=exposure, PU=purge, C= number of cycle, F= nitrogen flow rate, T=deposition temperature)

Deposition #	Precursor	P(s)	E(s)	PU(s)	C	F(sccm)	T(°C)
1	Tetrakis dimethylamido Zirconium IV(TDZ)	0.4	1	60	2127	20	250
	Deionized H_2O	0.025	1	60		20	250
2	Tetrakis dimethylamido Zirconium IV(TDZ)	0.4	2	80	2127	20	250
	Deionized H_2O	0.025	2	80		20	250

3.2.1 ALD Monolayer ZrO_2

Deposition of ZrO_2 at 250°C on the CCC was performed by using Tetrakis (dimethylamido) Zirconium (IV) and deionized (DI) H_2O precursors as Zr and O sources, respectively. The precursors were supplied by Sigma Aldrich. According to Table 3.2, one ALD cycle for deposition 1 includes: (i) pulse of Zr $(Nme_2)_4$ for 0.4 s this precursor dwelled in the reactor for exposure time of 1 s, (ii) purge the byproducts and unreacted species by using N_2 with flow rate of 20 standard cubic centimeters per minute (sccm), (iii) pulse of DI H_2O for 0.025 s that stays for 1 s in the reactor and (iv) purge the byproducts with N_2. The N_2 was supplied via a mass flow controller (MFC) with throughput of 20 (sccm) and 0.5 (torr) base pressure. In an ALD process, the role of N_2 as an inert gas is to ensure the uniform transport of the precursors to the reactor and purging the reaction byproducts. The flow rate of N_2 is optimized with the total pressure and the reactor geometry to give the best utilization and efficiency of the reactants [7].

These four steps were repeated for total number of 2127 cycles in deposition 1 to achieve ~200nm thick monolayer ALD-ZrO_2 on top of CCC substrate and then samples

were air-cooled after depositions. Identical procedure were followed for the deposition 2 and the only variant was the exposure time of precursor (2s) that allowed the precursors to dwell for longer time in the reactor, in comparison to deposition 1 with 1 s exposure time. Likewise, purging time of the byproducts increased to 80 s to ensure complete removal of any unreacted or highly reactive vapor from the reactor. In the following chapters the influence of this increment in the exposure of precursor will be discussed with further details.

3.2.2 ALD Trilayer $ZnO/Al_2O_3/ZrO_2$

For ALD of trilayer(s) of $ZnO/Al_2O_3/ZrO_2$ nanolaminate ceramic coatings, different metal and oxidant precursors, sourced from Sigma Aldrich, were utilized. First deposition of ZrO_2 at 250°C on the CCC was performed by using Tetrakis (dimethylamido) Zirconium (IV) and de-ionized (DI) H_2O precursors, similar to deposition 1 explained in section 3.2.1. Second, Al_2O_3 film was then grown at 200°C by using ALD sequence of Trimethyl aluminum (TMA) and DI H_2O precursors, and in the third stage, Diethyl zinc (DEZ) and DI H_2O precursors used to grow ZnO at 200°C. The N_2 throughput was 20 (sccm) and base pressure was 0.5 (torr). After depositions, the samples were air-cooled in atmosphere at ambient temperature prior to storage. The growth rate (GPC) measurements performed by using ellipsometry on the silicon wafer pieces are given on Table 3.3.

Table 3.3: Parameters for ALD deposition of one trilayer (ZnO /Al$_2$O$_3$/ ZrO$_2$) with ~ 220nm thickness, number of cycles for two and four trilayers are half and quarter of number of cycles for one trilayer, respectively (P=pulse, E=exposure, PU=purge, C= number of cycle, F= nitrogen flow rate, T=deposition temperature, GPC=growth per cycle)

Deposition # trilayer # cycles#: ZnO:Al$_2$O$_3$:ZrO$_2$	Precursor	P (s)	E (s)	PU (s)	F (sccm)	T (°C)	GPC (Å/cycle)
3 1 680:204:1283	Tetrakis dimethylamido Zirconium IV (TDZ)	0.4	1	60	20	250	0.78
	Deionized H$_2$O	0.025	1	60			
4 2 340:102:642	Trimethylaluminum (TMA) (Al(CH$_3$)$_3$)	0.015	1	20	20	200	0.98
	Deionized H$_2$O	0.015	1	20			
5 4 170:51:321	Diethyl Zinc (DEZ)((CH$_2$CH$_3$)$_2$)	0.015	1	60	20	200	1.47
	Deionized H$_2$O	0.015	1	60			

3.3 Film Characterization

3.3.1 Ellipsometry

For thickness measurements of individual layers of ALD-ZrO$_2$ Al$_2$O$_3$ and ZnO films, a J.A. Woolam variable angle spectroscopic ellipsometer (VASE) was employed. Measurements were between 400 and 1200 nm under 65º, 70º and 75º incidence angle. The VASE is equipped with a Czerny-turner scanning monochromator with a focal length of 160 mm and an effective aperture ratio of f/4.5. It was operated in the 400-1000 nm spectral range for all measurements. The Wvase32 software was used to acquire and model the data points.

3.3.2 X-ray Diffraction

A Rigaku Ultima III for glancing incident X-ray diffraction (GIXRD) analysis with source of CuK_α and wavelength of $\lambda=1.54\text{Å}$, 40 KV and 44 mA, was employed in the parallel beam mode using a thin film stage and a scintillation detector. The GIXRD scan performed from 20 to 90º 2tetha. For each scan these scan parameters remained constant: 0.45º incident angle, 0.03º step size,10 mm divergence height limiting slit, 5º incident side Soller slit, open attenuator, 0.5º diffracted side parallel beam (PB) slit and 1.0mm for all divergence, scattering and receiving slits (DS/SS/RS). Jadev7.0 was used to analyze the scan results for GIXRD.

3.3.3 Optical Microscopy

A Nikon Eclipse ME600 optical microscope was used at various magnifications (10x, 20x, 50x and 100x) for imaging the surface of each ALD-coated CCC samples and the corresponding counterface (pin) before and after the tribological testing.

3.3.4 Scanning Electron Microscopy and Focused-Ion Beam

A FEI Nova 200 NanoLab-focused ion beam (FIB/SEM) was used for elemental mapping with energy dispersive x-ray spectroscopy (EDS), surface imaging and specimen preparation (lift-out, thinning and polishing) for cross-sectional transmission electron microscopy (TEM). Cross- sectional EDS elemental mapping was used to trace the penetration depth of ALD coatings into the porous CCC substrates. More details about this investigation will be presented in the proceeding chapter.

Surface imaging included image of the CCC samples coated with ALD nanolaminates and the related counterface before and after each tribological test. Surface images were obtained at various voltage, current and magnification. Immersion mode of SEM was employed for high resolution imaging of the surface features such as wear debris and wear tracks.

Most of the SEM/FIB hours were used to prepare thin (<100nm) and transparent specimens for TEM studies. The capabilities of the FIB/SEM in lifting out site-specific samples for TEM investigation are beneficial to investigate the microstructure of unworn and worn ALD nanolaminates. The procedure of sample preparation is represented by the flowchart in Fig.3.2. The corresponding SEM images of sample preparation procedure were shown in Fig.3.3.

```
┌─────────────────────────────────────────────────────────────────────┐
│        Selection and patterning of a 20μm x 2.5μm area of the region of interest        │
└─────────────────────────────────────────────────────────────────────┘
                                    ↓
┌─────────────────────────────────────────────────────────────────────┐
│              Electron beam Pt deposition:3 KV, 4.3 nA, 20 minutes              │
└─────────────────────────────────────────────────────────────────────┘
                                    ↓
┌─────────────────────────────────────────────────────────────────────┐
│                  Ion beam Pt deposition:10 KV, 0.1 nA, 500nm                  │
└─────────────────────────────────────────────────────────────────────┘
                                    ↓
┌─────────────────────────────────────────────────────────────────────┐
│                 Ion beam Pt deposition:30 KV, 0.12 nA, 1000nm                 │
└─────────────────────────────────────────────────────────────────────┘
                                    ↓
┌─────────────────────────────────────────────────────────────────────┐
│        Rough milling of the area around and beneath of the specimen: 30KV, 7nA        │
└─────────────────────────────────────────────────────────────────────┘
                                    ↓
┌─────────────────────────────────────────────────────────────────────┐
│           Lift out the specimen by using nano-manipulator: 30KV, 50pA           │
└─────────────────────────────────────────────────────────────────────┘
                                    ↓
┌─────────────────────────────────────────────────────────────────────┐
│         Attaching the lift-out to the copper post by Pt gas injection welding         │
└─────────────────────────────────────────────────────────────────────┘
                                    ↓
┌─────────────────────────────────────────────────────────────────────┐
│    Parallel double side milling of the 2.5μm thick sample down to 1μm: 30KV, 1nA    │
└─────────────────────────────────────────────────────────────────────┘
                                    ↓
┌─────────────────────────────────────────────────────────────────────┐
│   Parallel double side milling of the 1μm thick sample down to 500 nm: 30KV, 0.1nA   │
└─────────────────────────────────────────────────────────────────────┘
                                    ↓
┌─────────────────────────────────────────────────────────────────────┐
│  Parallel double side milling of the 500 nm thick sample down to < 100nm: 5KV, 70 pA  │
└─────────────────────────────────────────────────────────────────────┘
                                    ↓
┌─────────────────────────────────────────────────────────────────────┐
│    TEM sample was subsequently plasma cleaned by using Ar to remove carbon and other    │
│                                  contaminants                                  │
└─────────────────────────────────────────────────────────────────────┘
```

Figure 3.2: Flowchart showing the sequence of TEM specimen preparation by using FIB/SEM.
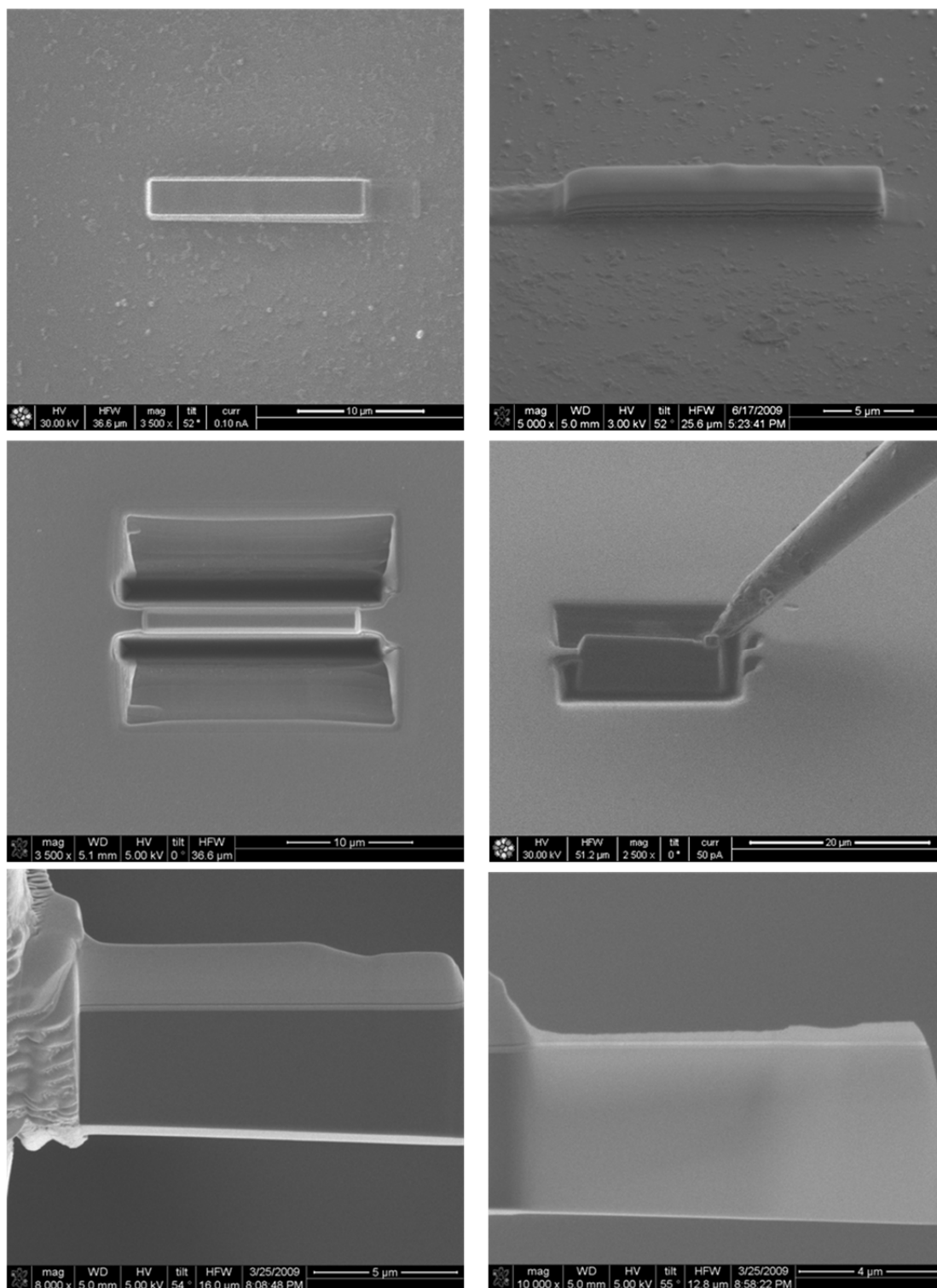
Figure 3.3: SEM images that display sequence of specimen preparation for cross-sectional TEM analysis, the specimen has silicon substrate coated with one ALD Trilayer of $ZnO/Al_2O_3/ZrO_2$.

3.3.5 Transmission Electron Microscopy and Scanning Transmission Electron Microscopy

A FEI Tecnai G2 F20 S-twin TEM equipped with a Schottky field-emission gun operated at 200keV was used to interrogate the ALD films nanostructures and deformation mechanisms due to wear tests. The Tecnai is equipped with a high angle annular dark field detector (HAADF) for Z-contrast imaging in STEM mode, and an EDAX® energy dispersive X-ray spectrometer (EDS).

3.3.6 X-ray Tomography

A SkyScan 1172 Desktop X-ray Microtomograph (Micro-CT) with the X-ray spot size of < 5μm, source voltage of 20-100kV, source current of 0-250 μA and spatial resolution of 0.8 μm was employed for non-destructive three-dimensional tomography analysis of the internal structure of the ALD-coated CCC foams. The X-ray detector includes a 12-bit digital cooled CCD with fiber-optic coupling to scintillator with automatic filter changer for beam-hardening compensation and multi-energy scanning. The resulting internal structure can be fully reconstructed and modeled non-destructively.

SkyScan 1172 produces two-dimensional shadow images of complete internal three-dimensional structures, but in a single two-dimensional shadow projection the depth information is completely mixed. No specific sample preparation or chemical fixation is required. It is equipped with micro-positioning, heating, cooling and compression/tension stages that allows to conduct in-situ tomography analysis.

3.3.7 Nanoindentation

Mechanical properties of ALD coatings such as stiffness and hardness were measured by Nanoindenter XP system from MTS Corporation, and using a diamond Berkovich indenter tip (tip radius ~50nm), which is preferred for low-load indentation testing. The NanoIndenter performs indentation tests by driving a diamond indenter into a flat specimen's surface and dynamically collects the applied force and displacement data. Material properties such as hardness and modulus are derived from the load and depth data.

One whole loading and unloading cycle of nanoindenter is illustrated in Fig 3.4. Herbert and co-workers showed that for all axisymmetric indenters, there is a constant relationship between the elastic contact stiffness, S (slope of the unloading curve), the projected area of contact, A ($=\pi a^2$), and the reduced or indentation modulus, E_r [8] :

$$E_r = \frac{\sqrt{\pi}}{2}\frac{S}{A} \qquad\qquad \text{(Eq. 3.1)}$$

E_r is related to the elastic modulus of the sample, E_s, through the elastic modulus of the Berkovich indenter, E_i, and Poisson ratio of the indenter, υ_i, and sample υ_s:

$$E_r = \left[\frac{1-\upsilon_i}{E_i} + \frac{1-\upsilon_s}{E_s}\right]^{-1} \qquad\qquad \text{(Eq. 3.2)}$$

Also hardness, H, with respect to indenter load, P, and contact area, A, is determined as:

$$H = \frac{P}{A} \qquad\qquad \text{(Eq. 3.3)}$$

The continuous stiffness measurement (CSM) was incorporated in nanoindentation to acquire Young's modulus and hardness with respect to indentation depth during the indentation, based on the indentation method that was proposed by Oliver and Pharr [9]. The continuous measurement of stiffness during the indentation is achieved by application of a small oscillation of high frequency (75 Hz) on the force signal and recording the displacement responses.

The maximum indentation depth in CSM is 500 μm with depth resolution of < 0.01 nm and the maximum load is 500 mN with resolution of 50 nN. ALD coated silicon wafers were mounted by using crystal bond on the 1-1/4" (31.75 mm) diameter aluminum cylinder and the cylinder was fixed onto the stage of the Nanoindenter XP system for indentation test. The poison's ratio was set at 0.3 for ALD ZnO and ALD ZrO_2.
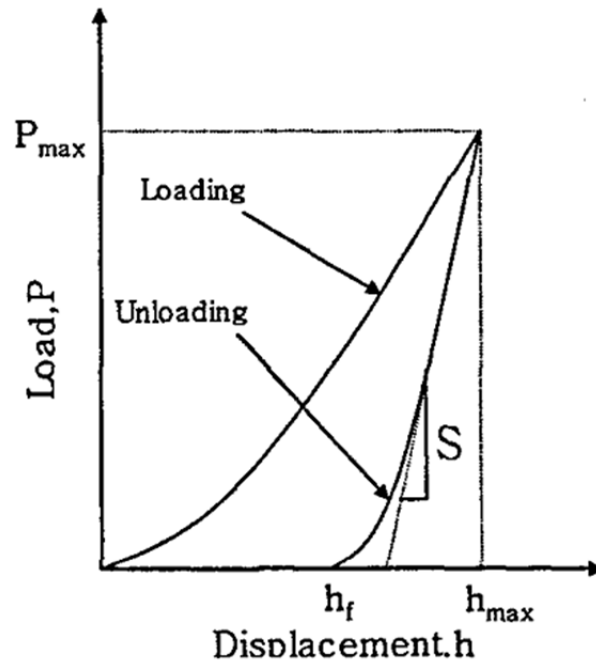
Figure 3.4: Schematic of indentation load-displacement data for
one complete cycle of loading and unloading [8].

3.4 Tribological Tests

3.4.1 Pin-on-disk Tribometer

A Falex ISC-200 from Implant Sciences Corp. pin-on-disk (POD) tribometer at ambient temperature with relative humidity of ~35% was used to measure the coefficient of friction (COF). The ALD films on CCC were subjected to the unidirectional sliding test against stationary ball of 1/8 inch diameter with various hanging loads of 100, 200 and 500 gram. Prior to each test, the ball was degreased and cleaned with methanol, acetone and distilled water and each test was ran on the fresh surface of the ball and substrate by changing the test radius. The revolution per minute (RPM) was adjusted to have linear speed of 21 mm/s for all POD tests. The ball travelled the total path of 2.0 x 10^5 mm for each wear track. The COF is calculated by taking the ratio of the tangential load, measure by a strain gauge transducer, to the normal load. Details of running POD test was outline in Table 3.4. For each deposition condition six POD test were conducted that varied based on the load (100-500g) and counterface materials (stainless steel440 (SS440) and Si_3N_4).

Following to each set of POD tests, a Veeco Dektak 150 Profilometer was employed to measure the wear depth and wear area and subsequently Eq. 3.4 was used to calculate the volumetric wear factor (loss) for each wear track:

$$Wear\ Factor\ (WF) = \frac{volumeloss}{Load\ .\ distance} = \left(\frac{mm^3}{N.m}\right)$$
(Eq. 3.4)

In order to investigate the tribological behavior of the ALD films infiltrated into the CCC under the unidirectional sliding test (POD), Hertzian contact model was used to

Table 3.4: POD tests frame to investigate the tribological behavior of ALD-infiltrated CCC

Deposition	Wear Track #	Load (g)	Counterface Material
1	1 & 4	100	SS440 & Si_3N_4
ALD ~200nm	2 & 5	200	SS440 & Si_3N_4
ZrO_2	3 & 6	500	SS440 & Si_3N_4
2	1 & 2	100	SS440 & Si_3N_4
ALD ~200nm	3 & 4	200	SS440 & Si_3N_4
ZrO_2	5 & 6	500	SS440 & Si_3N_4
3	1 & 2	100	SS440 & Si_3N_4
ALD One Trilayer	3 & 4	200	SS440 & Si_3N_4
~200nm **$ZnO/Al_2O_3/ZrO_2$**	5 & 6	500	SS440 & Si_3N_4
4	1 & 2	100	SS440 & Si_3N_4
ALD Two Trilayer	3 & 4	200	SS440 & Si_3N_4
~200nm **$ZnO/Al_2O_3/ZrO_2$**	5 & 6	500	SS440 & Si_3N_4
5	1 & 2	100	SS440 & Si_3N_4
ALD Four Trilayer	3 & 4	200	SS440 & Si_3N_4
~200nm **$ZnO/Al_2O_3/ZrO_2$**	5 & 6	500	SS440 & Si_3N_4

determine the contact parameters. Where the counterface (ball) is stationary and the ALD coated CCC sample was attached to a rotating disc by using crystal bond. This configuration (Fig. 3.5) is best described by Hertzian point contact in the elastic regime. Where the contact radius, *a*, is given by:

$$a^3 = \frac{3WR}{4\,E^*} \qquad \text{(Eq. 3.5)}$$

F_n is indication of the normal load, *R*, is the composite radius and E^*, is the composite (reduced) elastic modulus and they are defined below:

$$\frac{1}{R} = \frac{1}{R_1} + \frac{1}{R_2} \qquad \text{(Eq. 3.6)}$$

R_1 and R_2 are the radii of the contacting surfaces, in this case radii of the pin and disc. For concave surfaces the radius is negative while for convex surfaces it is positive. For flat surfaces, like disc, infinity is used as radii.

$$\frac{1}{E^*} = \frac{1 - v_1{}^2}{E_1} + \frac{1 - v_2{}^2}{E_2}$$

(Eq. 3.7)

E and v, are designating the elastic modulus and Poisson's ratio of the two contacting surfaces. In a point contact the mean pressure, P_m, is calculated by:

$$P_m = \frac{F_n}{\pi a^2}$$

(Eq. 3.8)

center of the point contact experiences the maximum pressure (Hertz pressure) (P_0):

$$P_0 = \frac{3P_m}{2}$$

(Eq. 3.9)

The kinetic friction coefficient is defined as the ratio of the frictional force, F_f, (lateral force) to the normal force:

$$\mu = \frac{F_f}{F_n} = \frac{A.\tau}{F_n}$$

(Eq. 3.10)

The frictional force (F_f) is represented as a product of the real area of the contact (A) and the interfacial shear strength, τ, a resistance to shearing that has to be overcome to have sliding. As it was assumed by Bowden and Tabor [10] in order to observe the sliding of two bodies relative to each other: (i) asperities should plastically deform and (ii) the interfacial stress component should correspond to the shear strength of the materials of lower shear strength ($\tau_{critical}$).

The Tresca criterion is used to compute the load required to initiate yield, W^y,:
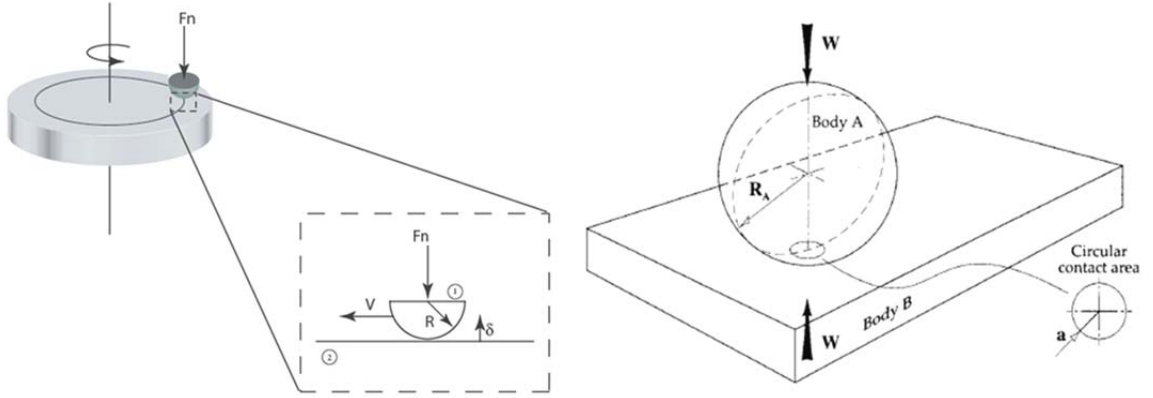
Figure 3.5: Contact configuration between pin and the flat disc in pin-on-disc method [1].

$$W^y = \frac{21.17 R^2 Y^3}{\left(E^*\right)^2} \qquad\qquad (Eq.3.11)$$

where, Y, represents the yield strength of the material of the contacting surfaces and is related to hardness (H) by H ~ 2.83 Y.

By using the above equations, Hertzian point contact parameters for both Si_3N_4 and SS440 ball were calculated by Romanes [11] (Table 3.5). The elastic moduli and hardness for both ALD-ZnO and ALD-Al_2O_3 were included, but Romanes used bulk values for silicon and tetragonal-ZrO_2, since there is not data presently reported for ALD film.

Through the frictional processes the velocity differences between two contacting bodies are accommodated and the mechanical energy, which is required to overcome frictional resistance, is transformed into internal energy or heat. This energy dissipation is responsible for the temperature rise in the contacting bodies, especially within the contact region on their sliding surfaces, where the temperatures are highest.

Table 3.5: Hertzian point contact conditions in POD test of Si (100) wafer and ALD film calculated by Romanes[11]

Property	Si (100)	Al₂O₃	ZnO	Stabilized-ZrO₂
R(mm)	infinite	Infinite	infinite	infinite
E(GPa)	125[b]	160	145	200[b]
Poisson's ratio, ν	0.22	0.30	0.30	0.31
Hardness (GPa)	8.7[b]	11	9	12.7[b]
F_n (N), normal load	0.196/0.49	0.49	0.49	0.196
W^y (N), Yield	239	342	209	416
Contact condition for using SS440 C pin with: R=1.6mm, E=203 GPa, ν=0.29				
E* (GPa)	82.48	98.05	92.70	110.73
a (μm)	14.2/19.2	18.2	18.5	12.9
P_m (GPa)	0.31/0.42	0.47	0.46	0.38
P_0 (GPa)	0.47/0.63	0.71	0.68	0.57
Contact condition for using Si₃N₄ pin with: R=1.6mm, E=310 GPa, ν=0.27				
E* (GPa)	94.45	115.23	107.92	133.15
a (μm)	13.6/18.4	17.2	17.6	12.1
P_m (GPa)	0.34/0.46	0.53	0.50	0.43
P_0 (GPa)	0.51/0.69	0.79	0.76	0.64

Frictional heating and resulting contact temperature (is called "flash temperature") and can have a siginificant influence on the tribological behvior and failure of the components in contact. For instance, it can cause changes in the structure and properties of the sliding materials (metallurgically transformed surface layer), oxidation of the surfaces, alteration of local geometery and possibly even melting of the contacting bodies [1, 12].

Set of formulation to calculate the flash temperature (T_{fa}) for various velocity ranges and contact geometries were developed by Blok in 1937, Jaeger in 1944 and Archard in 1958, that are fully addressed by Stachowiak and Batchelor [1]. The flash temperature, T_{fa}, for a circular point contact and a fast moving heat source was computed as below:

$$T_{fa} = T_0 + 0.308 \frac{\mu\, F_n |U_A - U_B|}{Ka} \left(\frac{\chi}{Ua}\right)^{0.5} \qquad \text{(Eq. 3.12)}$$

Where T_0 indicates the initaila temperature (ambient temprature), μ is the friction coefficient, F_n is the normal applied load (N), U_A and U_B are the surface velocities of solid A and solid B, respectively (m/s), U is the velocity of A or B, a is the contact radius (μm), and χ is the thermal diffusivity (m^2/s) equal to $K/\rho c$ in which K is the thermal conductivity (W/mK), ρ is density (kg/m^3) and c is specific heat (J/kgK).

To calculate the flash temperature, it is essential to know the rate of heat penetration into the contacting bodies, and this is expressed by Peclete number (Pe), which is the ratio of the speed of the surface to the rate of thermal diffusion into the solid. it describes whether there is sufficient time for the surface temperature distribution of the contact to diffuse into the stationary solid. A higher Peclet number indicates a higher surface velocity for constant material characteristics [1]:

$$Pe = \frac{Ua}{2k} \qquad \text{(Eq. 3.13)}$$

Where U indicates the speed of the half-surface beneath of the stationary source of heat (m/s), a is the radius of the contact and k is the thermal diffusivity (m^2/s).

For the POD test conditions that were outlined in Table 3.4, the Hertzian point contact (Table 3.5) was considered by Romanes [11] to calculate the Peclet number and flash temperature for contact between pins (Si$_3$N$_4$ & SS440 C) and different discs (Si (100) p-type, ALD-ZnO and ALD-ZrO$_2$ nanolaminates). By using slow moving heat source equation, Romanes showed that only minimal heating (~25-40ºC) takes place

during the unidirectional sliding test and this interfacial heating should not cause any thermally-induced transformation into the films (Table 3.6).

Table 3.6: Analysis of flash temperature for Hertzian point contact in unidirectional POD test

Properties	Si (100)	ZnO	Stabilized-ZrO$_2$
Density (kg/m^3)	2330	5600	6000
Specific Heat (J/kg K)	700	520	450
Thermal Conductivity(W/mK) @ RT	156	2.50	2.00
Normal Load (N)	0.20	0.49	0.20
Contact radius (m)	1.42E-05	1.82E-05	1.29E-05
Coefficient of friction	0.12	0.20	0.12
Therm. Diffusivity (m^2/s)	9.56E-05	8.59E-07	7.41E-07
Peclete number	0.002	0.233	0.191
Ave. Flash Temp (ºC)	25.06	37.85	30.45

3.4.2 Fretting Test

A high frequency reciprocating rig (HFRR) from PCS Instruments at ambient temperature, 150 °C and 400 °C with ~35% RH was used in order to simulate the fretting wear behavior of ALD-coated and uncoated CCC samples. Normal load of 0.2-1.0 N with a 6.0 mm diameter ANSI E-52100 pin under a reciprocating length of 1 mm and reciprocating frequency of 20-200 Hz were applied for 130 minutes. A Veeco Dektak 150 Profilometer was employed to measure the wear area and wear depth of each wear track. Then wear factor was computed by dividing the cross-sectional areas of the wear track by the load and by the number of cycles (Eq.3.4) where, number of cycles can be converted to the total distance that pin travelled on the sample, by knowing the reciprocating frequency.

Maximum flash temperature was calculated for Hertzian point contact between ANSI E-52100 pin and ALD-ZnO in fretting wear test. By converting the frequency to the linear speed and using the Eq. 13.3, the Peclet number was determined to be in the slow moving heat source range (Table 3.7). It was shown that the maximum flash temperature is too (~37 ºC) low that is unable to induce significant microstructural changes into the ALD-ZnO nanolaminates.

Table 3.7: Analysis of flash temperature for Hertzian point contact between ANSI E-52100 pin and ALD-ZnO in a fretting wear test which was conducted for 130 minutes by using 20Hz, reciprocating frequency, 1mm stroke length and 100 gram hanging load at ambient temperature

Properties	ANSI E-52100 pin	ZnO	Remarks
Density (kg/m^3)	7810	5600	
Specific Heat (J/kg K)	475	520	
Thermal Conductivity(W/mK) @ RT	46.6	2.50	Since the Peclet number is <0.1 the slow moving heat source equation is considered to calculate the maximum flash temperature:
Normal Load (N)	0.98		
Radius (mm)	3	infinity	T_{fMax}
Contact radius (m)	28.59E-6		
Coefficient of friction	0.429		$= 0.222 \dfrac{\mu U \left(P_y W \right)^{0.5}}{K}$
Therm. Diffusivity (m^2/s)	12.56E-6		Where P_y is yield stress of the ALD ZnO was taken from the Table 3.6
Peclete number	45.52E-3		
Max. Flash Temp (ºC)	36.997		

3.5 Chapter References

1. Stachowiak, G.W. and A.W. Batchelor, *Engineering Tribology*. 3 ed, ed. Elsevier2006.

2. *Engineering Properties of Toughened Zirconia*. Zirconium Oxide, ZrO_2; Available from: http://www.accuratus.com/zirc.html.

3. Sheppard, R.G., D.M. Mathes, and D.J. Bray, *Properties and Characteristics of Graphite for Industrial Applications*2001: POCO Graphite, Inc.

4. *ACF-10Q*. 2010; Available from: http://www.poco.com/MaterialsandServices/Graphite/IndustrialGrades/ACF10Q/tabid/88/Default.aspx.

5. *Savannah*. Available from: http://www.cambridgenanotech.com/products/savannah.php.

6. Elam, J.W., M.D. Groner, and S.M. George, *Viscous flow reactor with quartz crystal microbalance for thin film growth by atomic layer deposition*. Review of Scientific Instruments, 2002. 73(8): p. 2981-2987.

7. Ritala, M. and M. Leskelä, *Atomic layer deposition*, in *Handbook of Thin Films*, N. Hari Singh, M.Sc, and Ph.D, Editors. 2002, Academic Press: Burlington. p. 103-159.

8. Herbert, E.G., et al., *On the measurement of stress-strain curves by spherical indentation*. Thin Solid Films, 2001. 398-399: p. 331-335.

9. Oliver, W.C. and G.M. Pharr, An improved technique for determining hardness and elastic modulus using load and displacement sensing indentation experiments. Journal of Materials Research 1992. 7: p. 1564-1583

10. Bowden, F.P. and D. Tabor, *The Friction and Lubrication of Solids*. Vol. Part 1. 1986: Clarendon, Oxford.

11. Romanes, M.C., Structure and Low-Temperature Tribology of Lubricious Nanocrystaline ZrO_2 Monofilms and ZnO/Al_2O_3 Nanolaminates Grown by Atomic Layer Deposition, in Department of Materials Science & Engineering2008, University of North Texas: Denton.

12. Kennedy, F.E., Frictional Heating and Contact Temperature, in Modern Tribology Handbook2000, CRC Press.

CHAPTER 4

CHARACTERIZATION OF SLIDING WEAR MECHANISMS OF ATOMIC LAYER
DEPOSITED ZrO_2 AND TRILAYER $ZnO/Al_2O_3/ZrO_2$ NANOLAMINATE FILMS

The nanolaminate ALD films were deposited on three different substrates: (a) carbon-carbon composite, (b) carbon foam and (c) silicon wafer. The aim was to investigate the tribological behavior (friction and wear) of each of these samples at ambient temperature and humidity. Approximately 200 nm of the ALD ZrO_2 was deposited on the three substrates. The deposition parameters were outlined in Table 3.2, where deposition 2 has a higher exposure time of Tetrakis dimethylamido Zirconium IV (TDZ) precursor (2(s) in comparison to deposition 1 (1s)). The ALD trilayer of $ZnO/Al_2O_3/ZrO_2$ (deposition 3, 4 & 5 in Table 3.3) with total thickness of roughly 220 nm were also coated on the above substrates.

Prior to tribological testing the microstructure characterization of each ALD film was conducted by using XRD, cross-sectional TEM, cross-sectional EDS elemental mapping with FIB/SEM. Following the unidirectional pin-on-disc pure sliding test, the cross-sectional TEM analyses inside the worn surfaces were used to determine the mechanical wear and friction mechanisms.

4.1 Carbon-Carbon Composite Infiltrated with ALD ZrO_2

Approximately 200nm ALD ZrO_2 was deposited on carbon-carbon composite, according to the depositions parameters that were outlined in Table 3.2. Fig. 4.1 schematically shows the application of ALD to infiltrate ceramic thin film of ZrO_2 into

the CCC. The carbon-carbon substrate (Poco ACF-10Q) contains ~40 % amorphous carbon and ~60 % graphite crystal structure (space group P6$_3$/mmc). The ACF-10Q contains ~21 % porosity that 75 % of these porosities are open porosity, where the average pore size is 0.8 μm. Table 4.1 shows physical and mechanical properties of ACF-10Q, which unlike conventional graphite, has highly isotropic structure with isotropic factor of 0.97-1.03 that this gives the ACF-10Q maximum utilization for various applications.
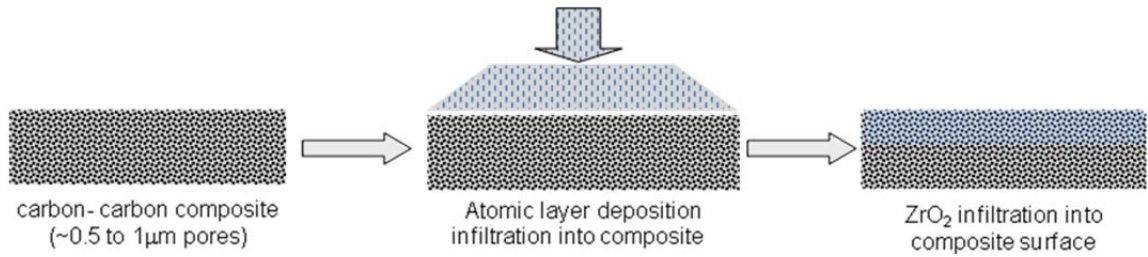

Figure 4.1: Illustration of the ALD ZrO$_2$ infiltration into the porous carbon-carbon composite.

It is expected that ALD-filled holes, with ceramic oxides such as ZrO$_2$, will contribute to the higher wear resistance and thermal stability of the CCC. Furthermore, at elevated temperatures (above 1650 ºC) the interface between carbonaceous substrate and the ALD-ZrO$_2$ can potentially undergo in-situ phase transformation into ZrC by the following carbothermal reduction of ZrO$_2$ layer:

$$3C_{graphite} + ZrO_2 = ZrC + 2CO_{(g)} \tag{Eq.4.1}$$

This is the subject of ongoing research at UNT. For this purpose the capabilities of ALD in depositing the films into the subsurface pores are advantageous and will provide further thermal and wear protection to the CCC substrate.

90

Table 4.1: Physical and mechanical properties of ACF-10Q [1]

Particle size (micron)	5	Tensile strength (N/mm^2)	69
Ave. Pore diameter (micron)	0.8	Modulus of Elasticity (N/mm^2)	11000
Total Porosity (%)	21	Tensile strain to failure (%)	0.62
Open porosity (%)	75	Hardness (HRC)	67
Apparent Density (g/cc)	1.77	Electrical resistivity (μ.Ohm.cm)	2460
Compressive strength (N/mm^2)	186	Coefficient of Thermal Expansion (micron/m) ° C	7.6
Flexural strength (N/mm^2)	97	Thermal conductivity (Watt/m K)	60

The most important criterion in designing a coating system is a reasonable match between coefficient of thermal expansion (CTE) of the substrate and coating. As is shown in Table 4.1, the CTE of CCC (7.6 x 10^{-6}/°C) is close to the CTE of tetragonal zirconia (5-10 x 10^{-6}/°C) [2, 3] therefore, less expansion mismatch and decohesion is anticipated at the interface of coating and CCC substrate.

4.1.1 ALD ZrO$_2$ Films Microstructure

The cross-sectional TEM micrograph in Fig. 4.2(a) shows as-deposited ALD ZrO$_2$ with approximate thickness of 200 nm on the CCC substrate. The unique capabilities of ALD in providing high conformal coating is obvious in Fig 4.2 (a), where the ALD ZrO$_2$ coated all the pre-existing asperities on the surface of CCC. Higher magnification micrograph in Fig. 4.2(b) illustrates how conformal ALD ZrO$_2$ was deposited on a ~20 nm thick asperity of the CCC and the curvature of the asperity was preserved during the ALD of ZrO$_2$.
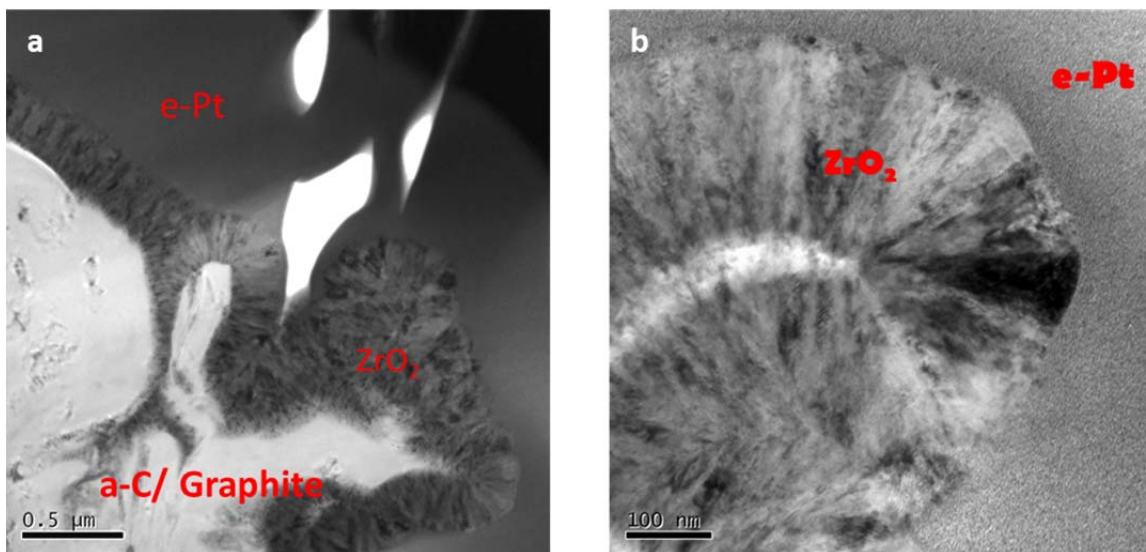
Figure 4.2: Cross-sectional TEM micrographs of conformal ALD ZrO_2 on CCC: (a) low magnification image shows thickness uniformity and (b) higher magnification image exhibits the coating conformality.

Fig. 4.3 shows the XRD result of depositions 1 and 2. With the negligible difference in the intensity of the peaks, the existence of same peak reflections is clear for both depositions. Tetragonal (101), (110) and (112) planes of ZrO_2 are the peaks of high intensity. Also hexagonal (0002), (10$\bar{1}$1) and (10$\bar{1}$3) observed due to the crystallinity of the graphite phase in the CCC. Furthermore, from the cross-sectional high resolution TEM micrograph in Fig. 4.4(a), measurement of atomic planes spacing and indexing the corresponding Fast Fourier Transform (FFT) (Fig. 4.4(b)) pattern, identified the crystallinity of graphite with (0002) texture related to basal planes that are surrounded by (101) planes of ZrO_2 and amorphous carbon. The corresponding grains of ZrO_2 and graphite related to each reflection in FFT pattern were shown in Inverse FFT (IFFT)

micrographs in Fig. 4.4(c & d). As shown in Fig. 4.4(a), both ZrO_2 and graphite grains are surrounded by regions of amorphous carbon.
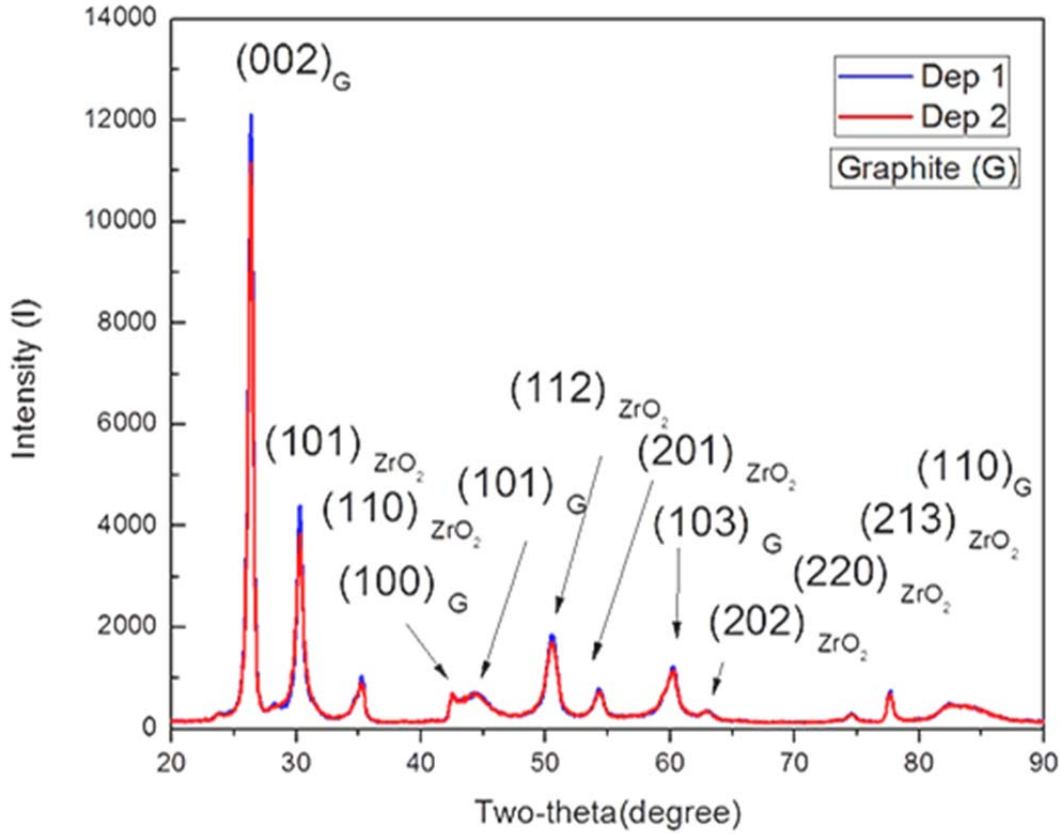

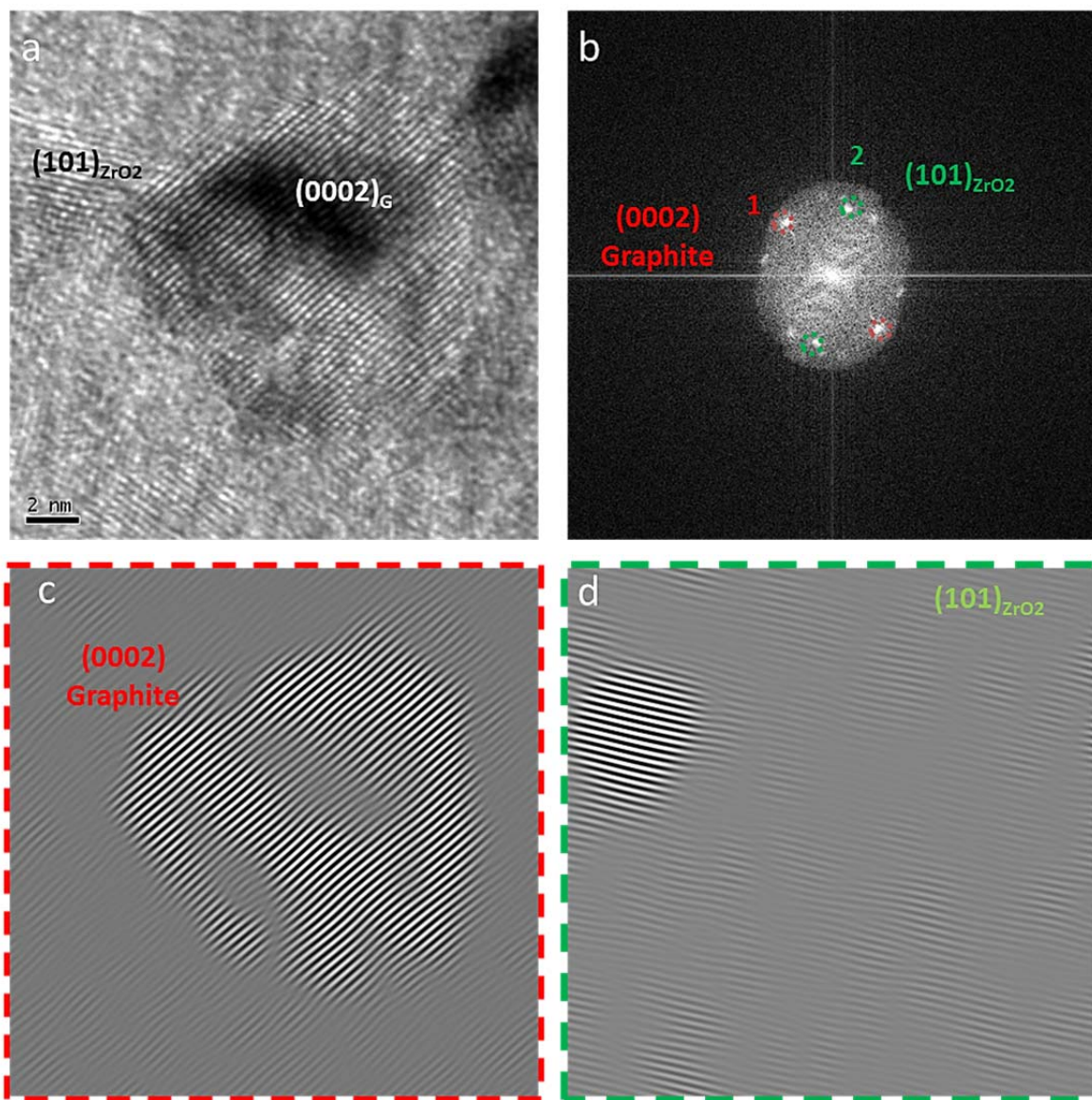Figure 4.3: XRD result of depositions 1and 2: ALD ZrO_2 on CCC Substrate.

Figure 4.4: (a) Cross-sectional HRTEM micrograph of Deposition 2 that shows atomic column of crystalline graphite and ZrO_2,(b) corresponding FFT pattern, (c) inverse FFT pattern of the $(0002)_G$ reflection, (d) inverse FFT pattern of the $(101)_{ZrO2}$ reflection.

4.1.2 Infiltration of ALD ZrO_2

Depositions 1 and 2 include the monolayer of ALD ZrO_2 on CCC. These depositions are varied based on the exposure time of Tetrakis (dimethylamido) Zirconium (IV) and de-ionized H_2O precursors, which are one and two seconds for deposition one and two, respectively. The results of EDS overlay elemental mapping in Fig. 4.5 display higher infiltration depth of ZrO_2 into CCC substrate for deposition 1(~100 μm) with 1 s exposure of precursor than deposition 2 (~75 μm) with 2 s exposure of precursor. This can be related to the near-to-surface pores closure in the CCC due to the longer exposure time of precursors that inhibits the vapor precursor to diffuse to the well-below-surface pores; hence the overall ALD penetration is deeper by using shorter exposure time. Furthermore, for both of these depositions, the top section of the ZrO_2 layer is denser than the bottom section and the denser section for deposition 2 (~50 μm) is slightly higher than the denser section of the deposition 1 (~40 μm).

4.1.3 Sliding Wear Behavior of ALD ZrO_2 Film

Steady-state friction coefficient (μ_{ss}) was measured for uncoated CCC and depositions 1 and 2 with hanging loads of 100, 200 and 500g. The surface image of as-deposited ALD ZrO_2 and the worn ALD ZrO_2 after POD test, were shown in Fig 4.6(a) and 4.6(b) respectively, where the tribological contact between SS440 ball and the CCC-ALD ZrO_2 gave rise to formation of smoother wear tracks. As shown in Fig. 4.7, steady-state friction coefficient (μ_{ss}) varied from ~ 0.20 to 0.25 against 440C SS ball for the above six conditions of depositions 1 and 2 (Fig.4.7 (b) and Fig.4.7(c)). The μ_{ss} for uncoated CCC substrate is ~ 0.20 (Fig.4.7 (a)), and there was not any remarkable change

in friction due to coating of CCC with monolayer of ZrO_2. A friction coefficient of ~0.2 is considered relatively low.
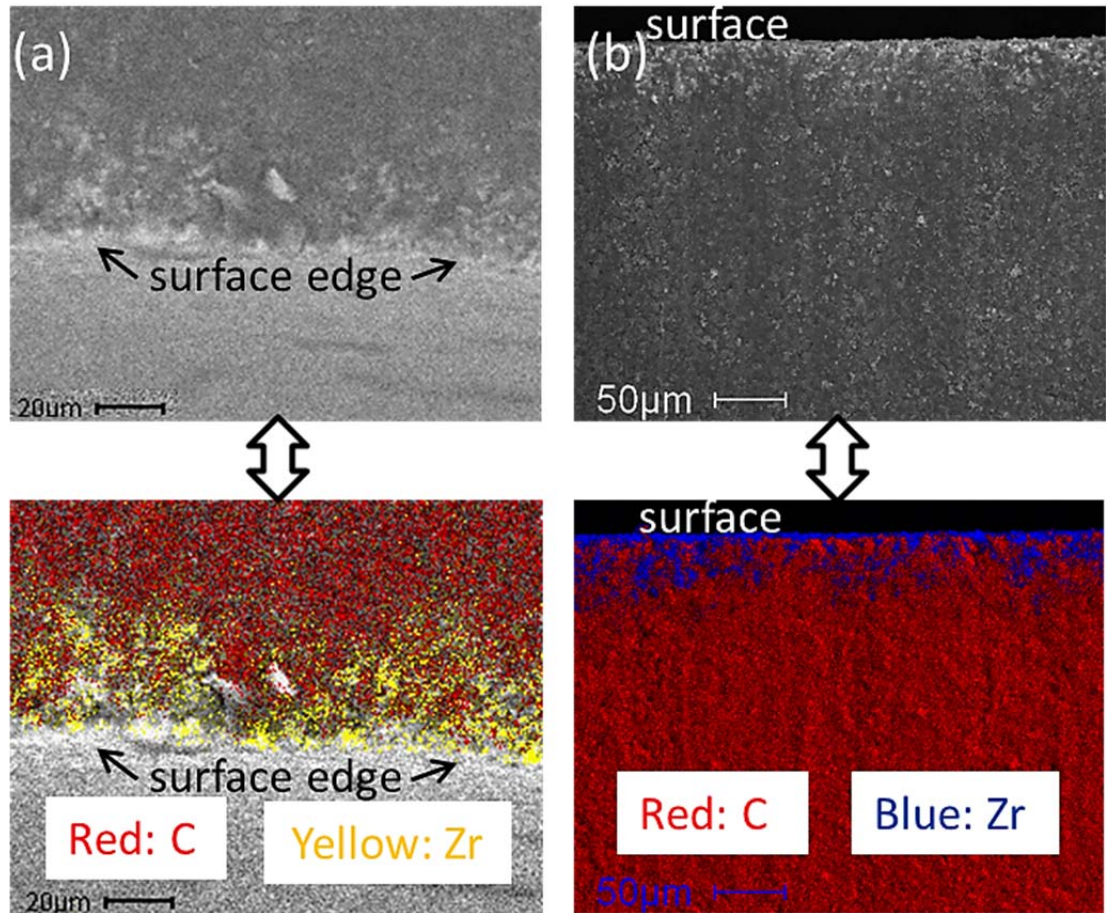

Figure 4.5: Cross-sectional SEM (top) and corresponding EDS elemental maps (bottom) of ~200 nm thick ALD ZrO_2 under exposure times of (a) 1s (deposition 1) and (b) 2s (deposition 2).
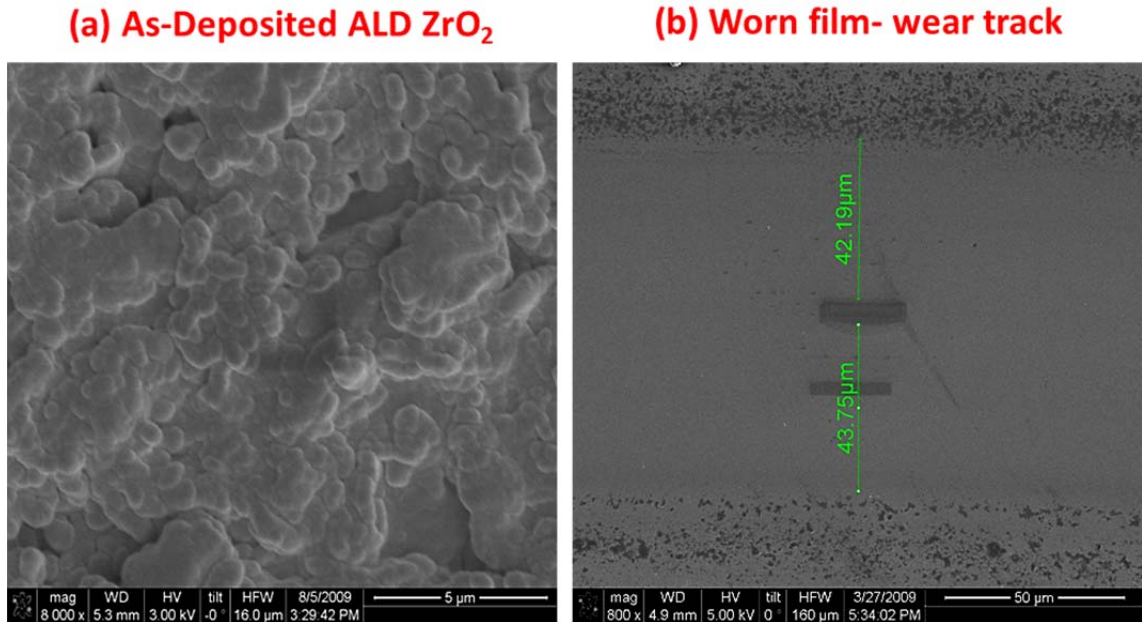
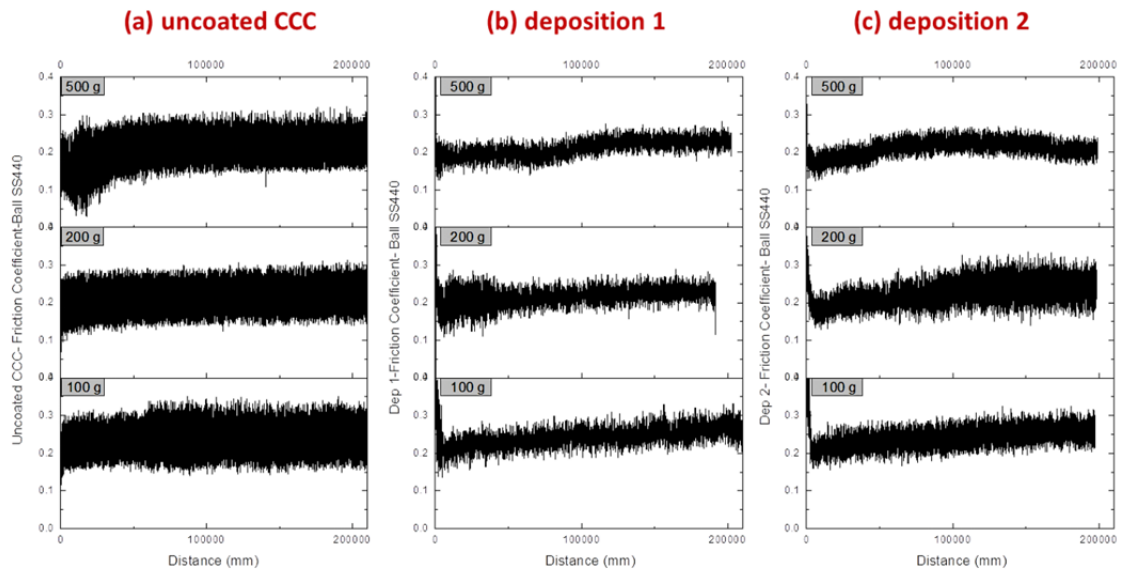Figure 4.6: Wear factor calculation for the uncoated C/C composite, deposition 1 and 2.

Figure 4.7: Friction coefficient in unidirectional sliding pin-on-disc test by using SS440 Ball.

In order to calculate the wear factor by using Eq.3.4, Veeco Dektak 150 Profilometer was employed to measure the wear track depth and wear track area. The result of wear factor calculations is shown in Fig. 4.8. Although based on the Archard's classification of the wear, the 10^{-6} wear rate is known as the mild wear regime, significant reduction in wear factor was observed by ALD ZrO_2 infiltration into CCC in comparison to uncoated CCC ($\sim 4 \times 10^{-6}$ for uncoated CCC to $\sim 2.5 \times 10^{-6}$ for deposition 1). Furthermore, with 2 second exposure time of precursors (deposition 2), the wear factor reduced considerably in comparison to uncoated CCC and depositions 1. As shown in the EDS elemental maps (Fig. 4.5), the lower wear factor in deposition 2 is related to the thicker dense region (~ 50 μm) of ALD ZrO_2 coating on the CCC. Furthermore, while there were no clear differences in the friction coefficients between uncoated CCC and ALD ZrO_2 coated CCC, clearly the wear factors were different. This suggests that low friction coefficients do not always translate to low wear factors.

The cross-sectional TEM analysis of the worn ALD ZrO_2 on CCC substrate (Fig 4.9) revealed the existence of tribologically transformed layer, known as the mechanically mixed layer (MML), at the contact which contained nanocrystalline ZrO_2 (fragmented coating) intermixed with an amorphous carbon matrix from the CCC. This mixture of amorphous carbon and harder ZrO_2 is responsible for the improved wear factors shown in Fig. 4.8, in comparison to the uncoated CCC. Additionally, depth of plastic strain for worn uncoated CCC is ~ 5 μm which is less than the worn ALD ZrO_2 on CCC with a ~ 2 μm-deep MML layer.
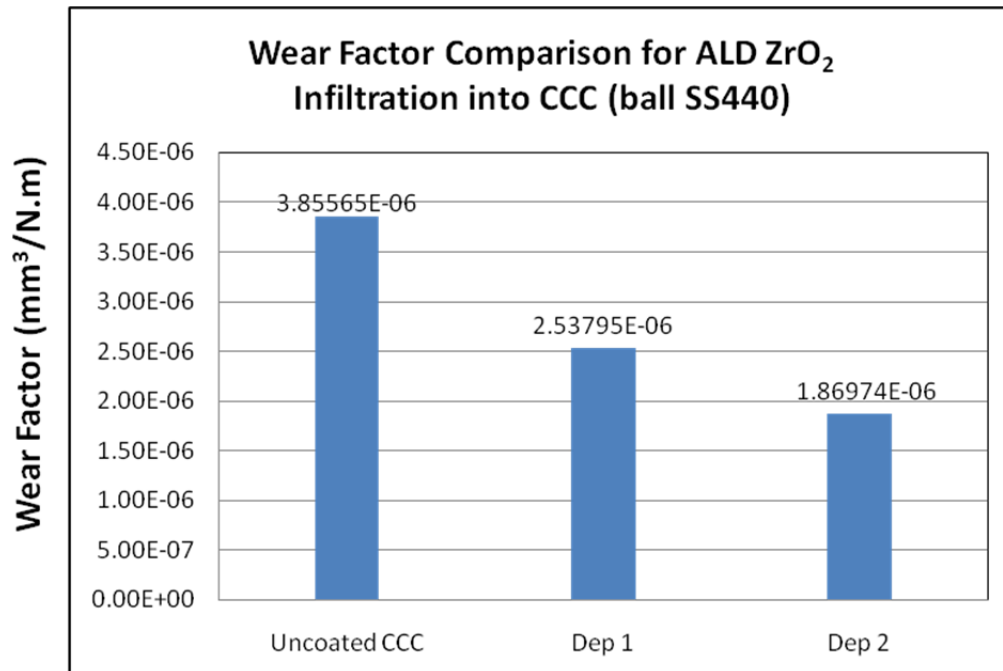
Figure 4.8: Wear factor calculation for the uncoated C/C composite, deposition 1 and 2.
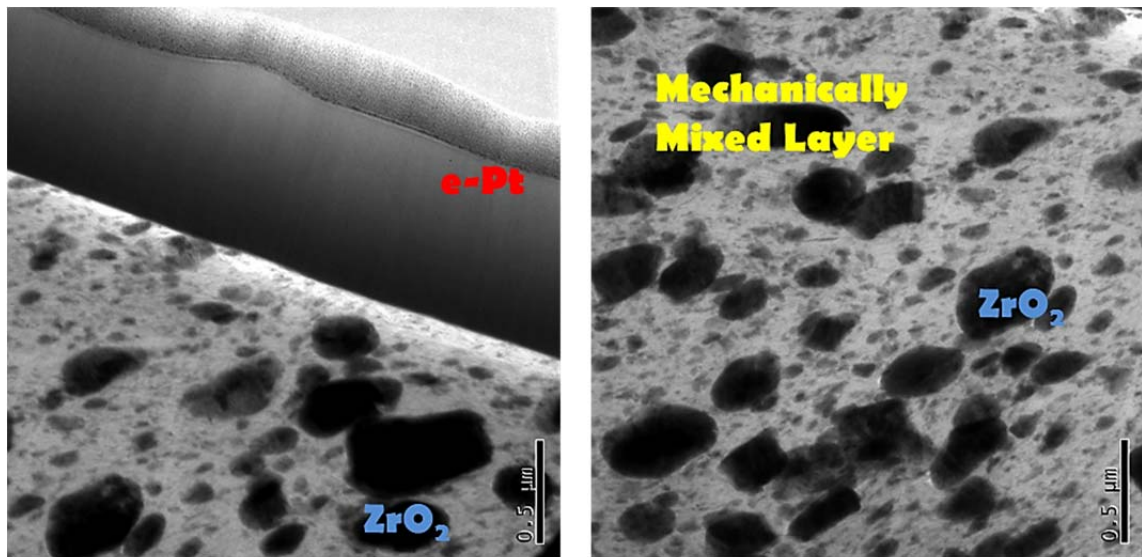

Figure 4.9: Cross-section TEM investigation of the worn ALD ZrO_2 shows formation of a mechanically mixed layer (MML) due to the contact in POD test.

4.2 Carbon Foam Infiltrated with ALD ZrO$_2$

The carbon foam (POCO HTC) is porous graphite that has low density, high thermal conductivity and very efficient thermal energy transfer characteristics. It contains ~61 % porosities that 95 % of these are open porosities. The average pore diameter is 350μm (Table 4.2).

Table 4.2: Physical and mechanical properties of carbon foam POCO HTC [4]

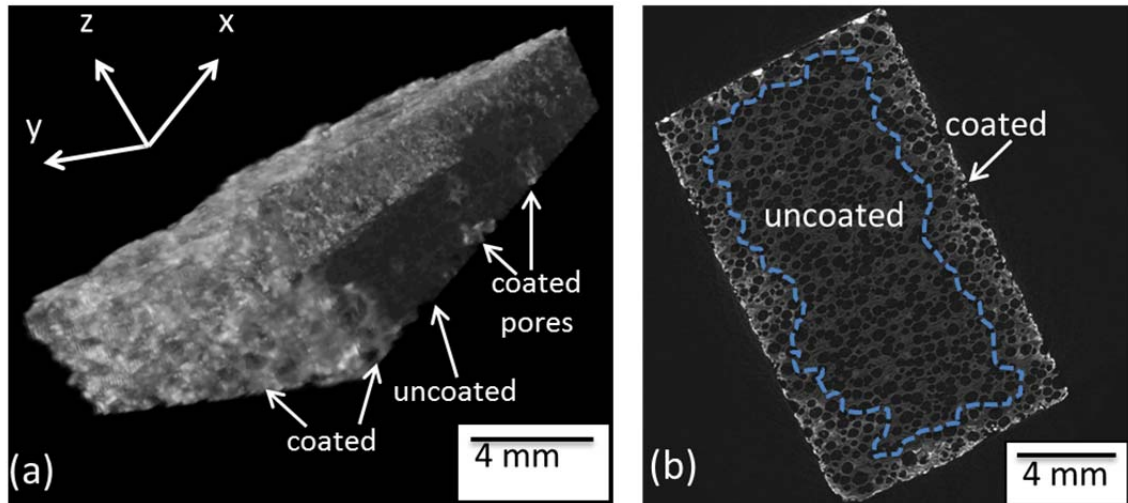| Ave Pore diameter (micron)	350	Thermal conductivity in x-y direction (Watt/m K)	70
Total Porosity (%)	61	Thermal conductivity in z direction (Watt/m K)	245
Open porosity (%)	95	Compressive strength (MPa)	5.90
Apparent Density (g/cc)	0.9		

Figure 4.10: X-ray tomography images in (a) 3-D and (b) 2-D (x-y plane slice) of ALD ZrO$_2$ infiltrated carbon foam.

The ALD deposition parameters were outlined in Table 3.2 (similar to deposition 1: Fig 4.1) were used to deposit approximately 200nm of ZrO_2 into the carbon foam. Fig. 4.10(a) and 4.10(b) represent the x-ray tomography reconstruction of the ALD-coated carbon foam. Fig. 4.10(b) is a cross-section and top-view of the 3-D image in Fig. 4.10(a). The dashed lines in Fig. 4.10(b) show the boundary of infiltrated ALD-ZrO_2 with a ~ 1.5 mm uniform infiltration depth into the porous carbon foam.

Fig. 4.11(a) is a cross-sectional TEM micrograph of ALD ZrO_2 infiltrated carbon foam that shows the abilities and effectiveness of ALD in filling most of the subsurface pores, besides having ~ 200nm ALD ZrO_2 on the surface. Similar to the CCC, the carbon foam subsurface pores are simultaneously being coated along with the foam surface until the pores are completely closed off and coating the surface only continues. This is the why the ZrO_2 coating thickness along the pores never reaches the ~200 nm coating thickness on the surface, as depicted in Fig. 4.11(a). It is expected that ALD-filled holes, with these ceramic oxides, will contribute to the higher wear resistance and thermal stability of the carbon substrates. Higher magnification of the carbon foam and ZrO_2 interfaces are shown in Figures 4.11(b) and 4.11(c). These interfaces play an important role in determining the properties of ALD-infiltrated carbon foam. It is believed that creating in-situ ZrC phase in carbon foam by carbothermal reduction of the ZrO_2 layer (Eq. 4.1) can further enhance the wear resistance of the carbon substrates, which is the study of ongoing and future research. Occurrence of the above reaction can potentially enable the ALD-ZrO_2 infiltrated CCC and carbon foam to undergo this in-situ modification during operation.
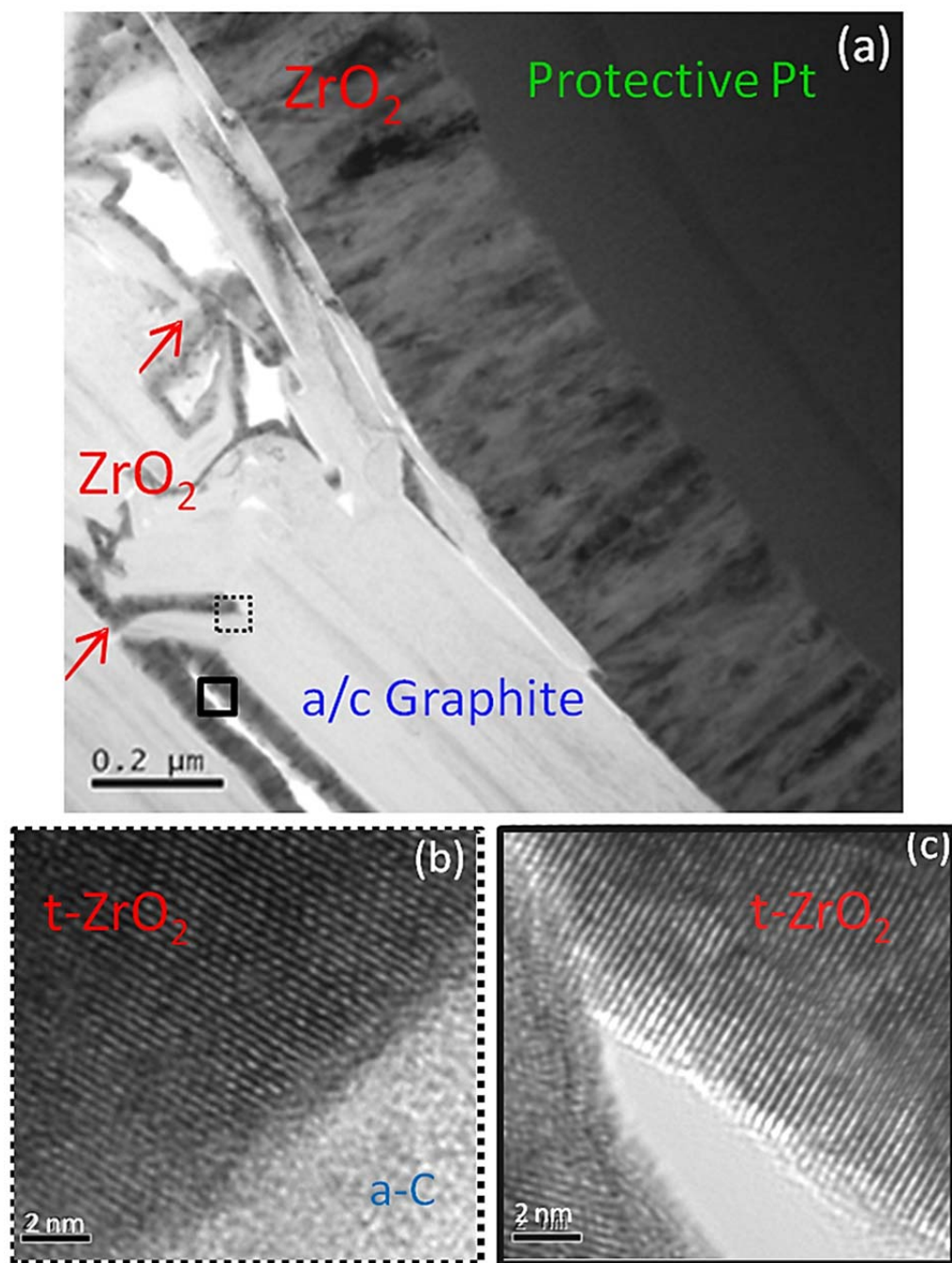
Figure 4.11: (a) Cross-sectional TEM image of ALD ZrO_2 infiltrated carbon foam that shows surface and subsurface ZrO_2 infiltration, and higher magnification images taken inside subsurface pores of (b) interface between amorphous carbon and ZrO_2, and (c) two ZrO_2 grains. Images were taken from the dashed and solid boxes shown in (a), respectively.

ALD, which is a step-like CVD, is known for its proven capabilities in coating of high-aspect ratios devices and features with complex shape. It provides excellent conformality and trench-filling abilities [5-7]. Hence, ALD was employed for this study to enhance the infiltration depth of ZrO_2 into porous CCC substrate and this is anticipated to enhance wear resistance and thermal resistance of the CCC. As depicted in Figures 4.10 and 4.11, monolayer ALD ZrO_2 uniformly filled the pores of less than ~300nm without any intermixing. This proves the capabilities of ALD in producing nano-scale conformality and creating sharp interfaces between different coatings and trilayer nanolaminates.

As was shown in Table 3.3, the growth rate of ALD ZrO_2 is 0.78 Å/cycle. A number of studies [8-10] showed that, depending on the type of precursor, the deposition temperature in ALD has significant influence on structure and growth rate of ZrO_2 layer. For instance Cassir et al. [8] used $ZrCl_4$ (99.9% purity) and de-ionized Millipore water as precursors and deposited ALD ZrO_2 at a range of temperatures (250-450 °C), maximum growth kinetic was found in the range of 380-400 °C with 5 Å/cycle.

ZrO_2 exists in four basic crystalline polymorphs, monoclinic (m-ZrO_2), tetragonal (t-ZrO_2), cubic (c-ZrO_2) and orthorhombic (o-ZrO_2). The m, t and c-ZrO_2 are known as the low pressure polymorphs and the o-ZrO_2 is stable at high pressure condition.
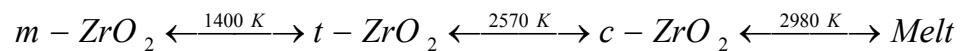
$$m - ZrO_2 \xleftrightarrow{1400\ K} t - ZrO_2 \xleftrightarrow{2570\ K} c - ZrO_2 \xleftrightarrow{2980\ K} Melt$$

An important concept which is often utilized in zirconia ceramics is to alloy pure ZrO_2 with another suitable oxide, such as MgO (magnesia), CaO (calcia) and rare earth (RE) oxides such as Y_2O_3 (yttria) and CeO (ceria), to fully or partially stabilize high

103

temperature polymorphs (m and t) of ZrO_2 to lower temperatures. The volume expansion associated with the tetragonal to monoclinic transformation can be used to advantage for improving toughness and strength. For instance tetragonal zirconia can transform to monoclinic under the influence of a crack tip stress and this transformation may cause the crack tip to deflect and significant toughening effect results [10, 11].

But without addition of the aforementioned oxides into pure ZrO_2, studies showed that ALD is capable of producing retained t-ZrO_2 and c-ZrO_2 that are stable at room temperature and in this case, the structure of ZrO_2 is highly dependent upon type of precursors used, growth temperature and film thickness [12, 13].

Similarly, from the XRD results in Fig. 4.3 for both depositions 1 and 2, the existence of retained tetragonal zirconia with texturing of (101) (2theta=30.5) grains was detected. Also other atomic plane reflections like (110) and (112) were observed. While it is difficult to distinguish between the cubic and tetragonal polymorphs of zirconia using XRD, previous selected area electron diffraction (SAED) patterns of the same films revealed the presence of higher order tetragonal zirconia reflections that are not present in cubic zirconia [14]. Furthermore, crystallinity of the CCC substrate with graphite structure of (0002) textured grains as well as (10$\bar{1}$1) and (10$\bar{1}$3) orientated grains was confirmed by XRD and cross-sectional HRTEM analyses. Therefore, the dominant crystallinity of the CCC is the presence of (0002) (2theta=26.5) basal planes of graphite and (101) of tetragonal zirconia that are responsible for the aforementioned tribological behavior of pure ZrO_2 (depositions 1 and 2).

For all of the POD tests on depositions 1 and 2 the steady-state friction coefficient (μ_{ss}), by using SS440C ball, is approximately 0.20-0.25 and μ_{ss} for uncoated CCC is almost 0.20 (Fig. 4.7(a)). This shows that application of ALD ZrO_2 does not lead to remarkable friction improvement, but it is capable of improving wear resistant of CCC, based upon the wear factor calculations (Eq.3.4) and is similar to other studies [15]. The low sliding friction of uncoated CCC in comparison to ALD ZrO_2 is related to the texture existence of low surface energy (0002)-basal planes in graphite that provided low sliding friction coefficient. However, the improvement in the wear resistance in the ALD ZrO_2 coated CCC, compared to uncoated CCC, is due to the sliding-induced MML that provides increased hardness/toughness to the CCC, both at the surface and subsurface.
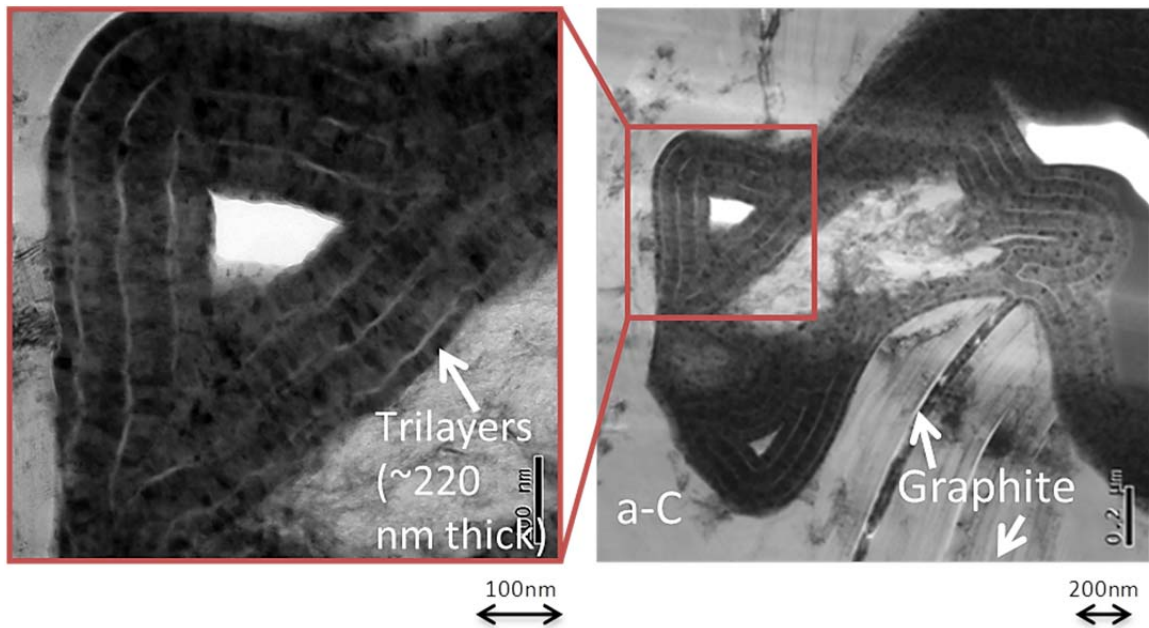

Figure 4.12: Cross-sectional TEM image of four $ZnO/Al_2O_3/ZrO_2$ trilayers infiltrated into CCC (a-C/graphite) displaying the capabilities of ALD to conformally and uniformly coat subsurface pores.

4.3 Carbon-Carbon Composite Infiltrated with ALD Trilayer $ZnO/Al_2O_3/ZrO_2$

The ALD deposition parameters were considered for deposition of trilayers of $ZnO/Al_2O_3/ZrO_2$ were shown in Table 3.3. Fig. 4.12 shows how different combination of ALD ceramic oxide trilayers can uniformly and conformaly coat the subsurface pores in a sequential manner. The existence of sharp interface between each individual layer is obvious and no intermixing between these layers occurred during the deposition. By knowing the GPC of each film under the ALD conditions (Table 3), it is possible to obtain precise thickness of each layer, where deposition 3 includes one trilayer (Fig 4.13 (a)), deposition 4 includes two trilayers (Fig 4.13 (b)) and deposition 5 includes four trilayers (Fig 4.13 (c)).
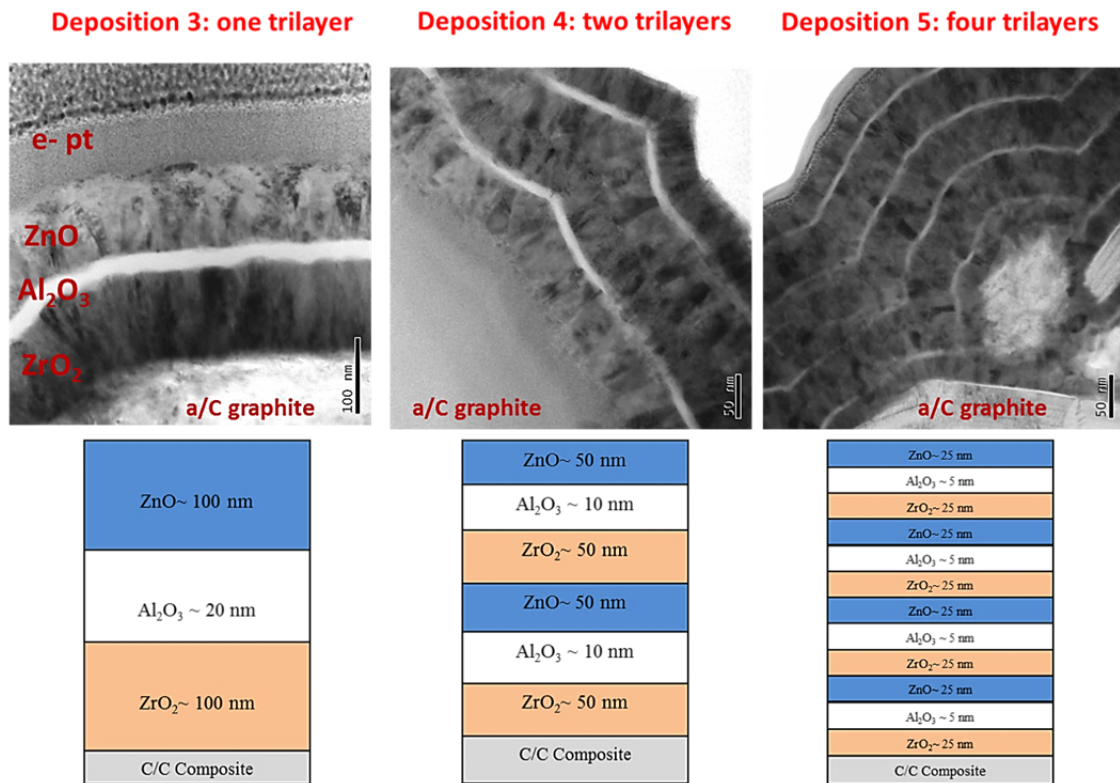

Figure 4.13: (a) Cross-sectional TEM micrographs of depositions 3, 4 and 5 of ALD trilayers of ZnO /Al_2O_3/ ZrO_2 (b) schematic of layers in each deposition with approximate thickness.

4.3.1 ALD Trilayer ZnO/Al$_2$O$_3$/ZrO$_2$ Microstructure

The XRD analyses that were conducted on deposition 3 with one ALD trilayer is shown in Fig. 4.14. The (0002) – graphite and (101) - ZrO$_2$ (tetragonal) and (0002)-orientated grains of wurtzite ZnO were determined. The existence of (0002), (10$\bar{1}$1) and (10$\bar{1}$1) ZnO peaks in XRD plot was confirmed by indexing the FFT pattern in Fig. 4.15.
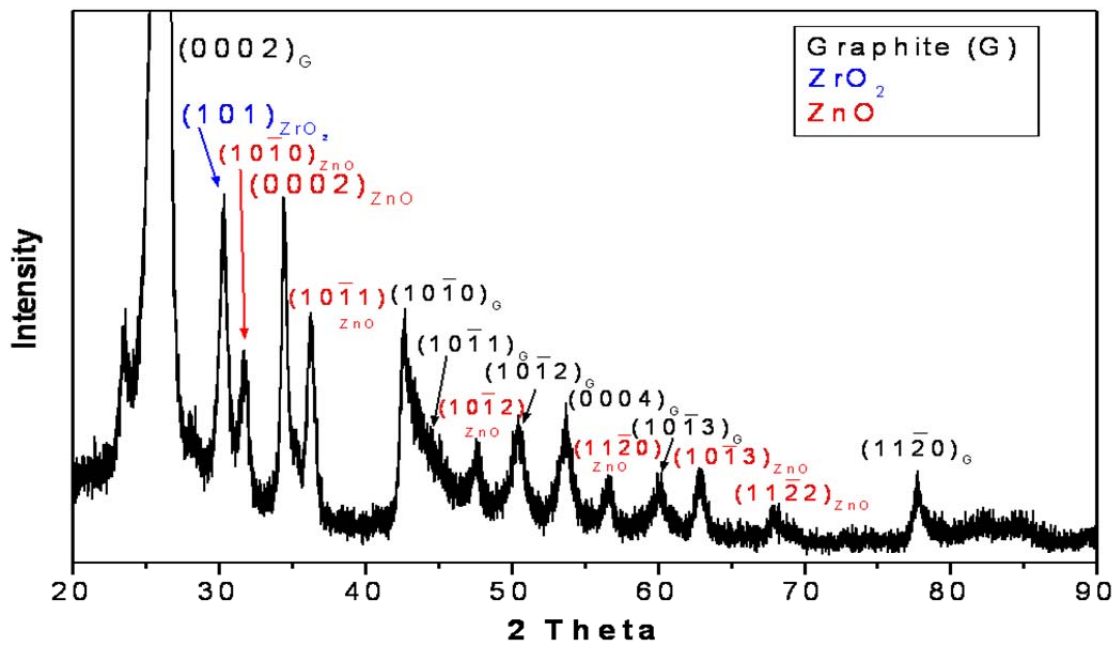
(hkl)	2-Theta	Material	(hkl)	2-Theta	Material
(0002)	26.603	Graphite	(10-12)	50.816	Graphite
(101)	30.409	ZrO$_2$	(0004)	54.794	Graphite
(10-10)	31.847	ZnO	(11-20)	56.744	ZnO
(0002)	34.338	ZnO	(10-13)	60.035	Graphite
(10-11)	36.304	ZnO	(10-13)	62.784	ZnO
(10-10)	42.466	Graphite	(11-22)	68.031	ZnO
(10-11)	44.666	Graphite	(11-20)	77.699	Graphite
(10-12)	47.532	ZnO			

Figure 4.14: XRD result of depositions 3 includes one ALD trilayer of
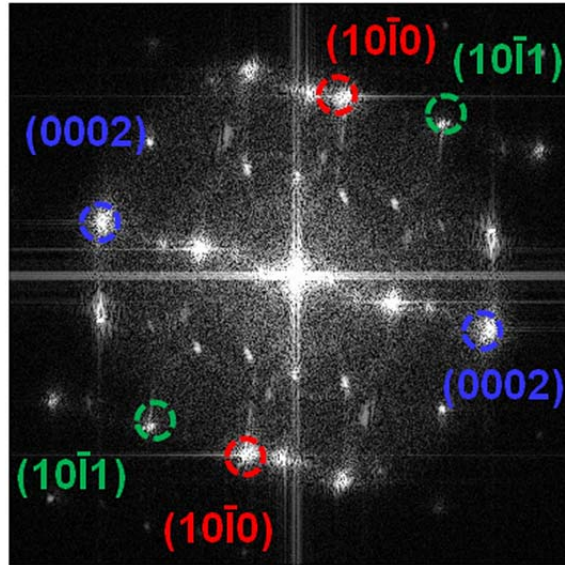ZnO /Al$_2$O$_3$/ ZrO$_2$ on CCC Substrate.

Figure 4.15: FFT pattern of ALD ZnO grain
looking down the [01$\bar{1}$0] zone axis that show the
reflections form basal {0002}, prismatic {10$\bar{1}$0} and
pyramidal {10$\bar{1}$1} planes of wurtzite ZnO.

Unlike deposition 3, in depositions 4 and 5 the ALD ZrO_2 was deposited on ALD ZnO (Fig. 4.13(b & c), and the texture of ALD ZnO layer in this case may give a rise to change in structure of ALD ZrO_2.

4.3.2 Sliding Wear Behavior of ALD Trilayer

Fig. 4.16 (a) shows the steady-state friction coefficient (μ_{ss}) of depositions 3, 4 and 5 and by comparison it is clear that μ_{ss} decreased from a range of ~0.20 to 0.25 (uncoated CCC and monolayer of ALD ZrO_2) to a range of ~0.14 to 0.16 (ALD trilayer ZnO /Al_2O_3/ZrO_2). It is clear that ALD ZnO provides more solid lubricity at the sliding surface in comparison to ALD- ZrO_2 infiltrated CCC. In addition, there is a slight reduction in the friction coefficient from ~0.16 to 0.14 when decreasing the number of ALD trilayers, Fig. 4.16 (b-d).
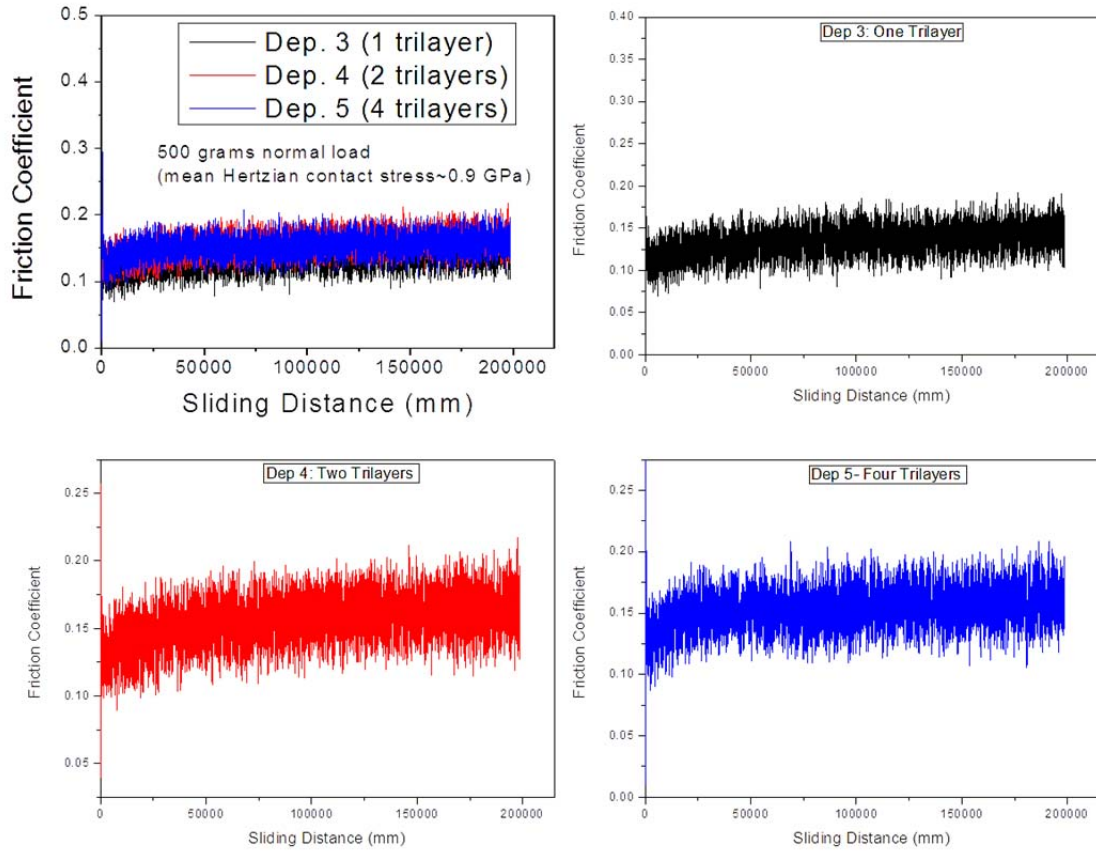
Figure 4.16: Steady state friction coefficient for the uncoated CCC, depositions 3, 4 and 5.

Although the mean Hertzian contact pressure is ~0.9 GPa for POD test in Fig 4.16, but observation of similar wear and friction behavior is expected for the actual CCC bushings. Since the contact for bushings is larger (tens of millimeter) and accordingly the contact pressure is ~0.1 GPa.

The influence of the application of higher applied normal loads in the pin-on-disc unidirectional sliding tribometer is clear by comparing the cross-sectional TEM micrographs in Fig. 4.17(a) and Fig. 4.17(b). Application of higher normal load resulted

in the fracture of surface and close-to-surface trilayers (area enclosed by dashed lines), i.e., thicker MML, but the subsurface porosities that were filled with trilayers were untouched (pointed out by arrows), and this is anticipated to be a contributing factor to the total enhancement in the wear behavior and potentially thermal resistance of CCC.
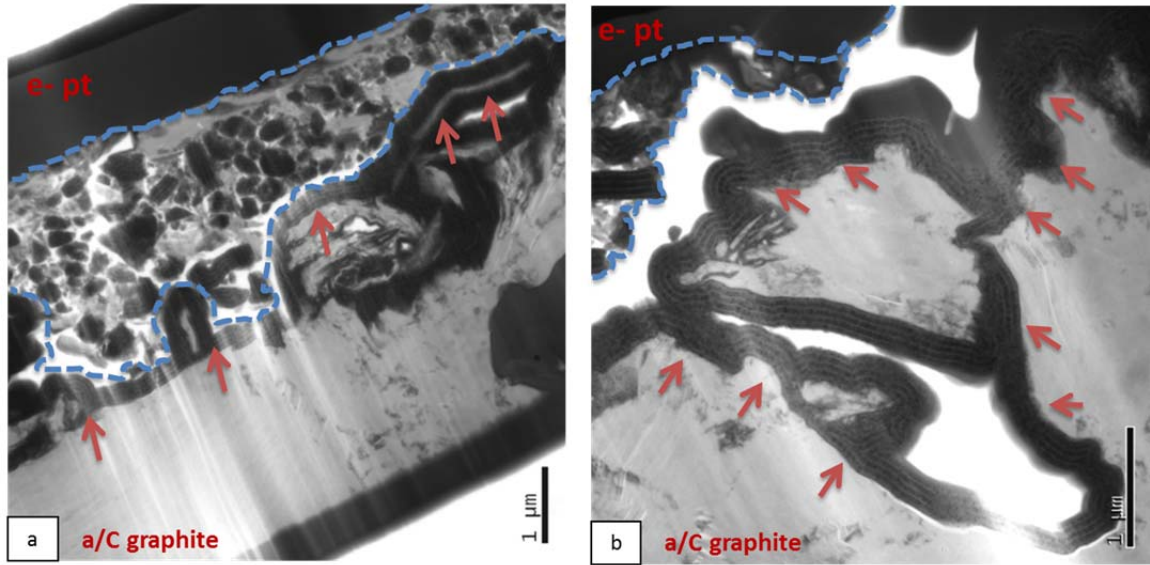

Figure 4.17: Low magnification cross-sectional TEM micrographs of inside the wear track of deposition 5 with four trilayers of ZnO /Al$_2$O$_3$/ ZrO$_2$, using Si$_3$N$_4$ ball with hanging weights of (a) 500g and (b) 200g.

In the crystalline region of deformed ZnO layer, inside the wear track, ZnO basal plane stacking faults were observed (arrows in Fig. 4.18 (b)) in the sliding direction. Indexing the FFT pattern (Fig.4.18(c)) showed that these reflections are due to the basal (0002) plane of wurtzite ZnO. Of importance are most of these basal stacking faults (BSF), denoted by the arrows, originate from incoherent boundaries between adjacent nanocolumnar grains or condensation of vacancies or interstitials, so that a missing or extra (0002) plane will be introduced into the lattice. Thus, the low angle grain

boundaries are acting as a source of BSF's in addition to the internal basal loops inside the grains. The HRTEM micrograph in Fig 4.18(d) displays clearly the transition in stacking sequence of (0002) basal planes, where *ABAB* stacking sequence changes to *CBCB*. This basal stacking fault is known as a type I intrinsic (ABAB|CBCB). The {0002}-basal planes are low surface energy planes and exhibit the lowest stacking fault energies (SFE) of ~ 24 mJ/m^2 (in comparison to the{10$\bar{1}$0}-prismatic planes which have higher surface energy planes and higher SFE of ~427 mJ/m^2. These SFE's were calculated using the Vienna Ab Initio Simulation Package (VASP), an *ab initio* density functional theory (DFT) technique, by UNT colleagues, Mr. Niraj Gupta and Dr. Srinivasan Srivilliputhur.

Therefore, there is evidence of some localized plasticity in the nanocolumnar ZnO grains where activating subsurface basal stacking faults will promote intrafilm shear/slip and accordingly improve friction. This ZnO Type I intrinsic stacking fault with the rigid body displacement (Burgers) vector b = $\overrightarrow{CB}$: 1/6 [02$\bar{2}\bar{3}$], is shown in Fig. 4.19(a). The stacking fault is bordered by the above partial dislocation (PD) and confirmed by the VASP-generated stacking fault sequence in Fig. 4.19(b). Fig. 4.19(c) shows the velocity accommodation mode of intrafilm shear where slip of these PD's likely occur by dislocation glide along the ZnO {0002} basal planes.

To summarize, a high density of sliding (shear)-induced stacking faults were observed inside the wear tracks of ALD nanolaminates (in comparison to unworn nanolaminates) which are responsible for solid lubrication. Intrafilm shear with this

friction induced subsurface (mechanically mixed layer) aids in shear accommodation (prevents brittle fracture).
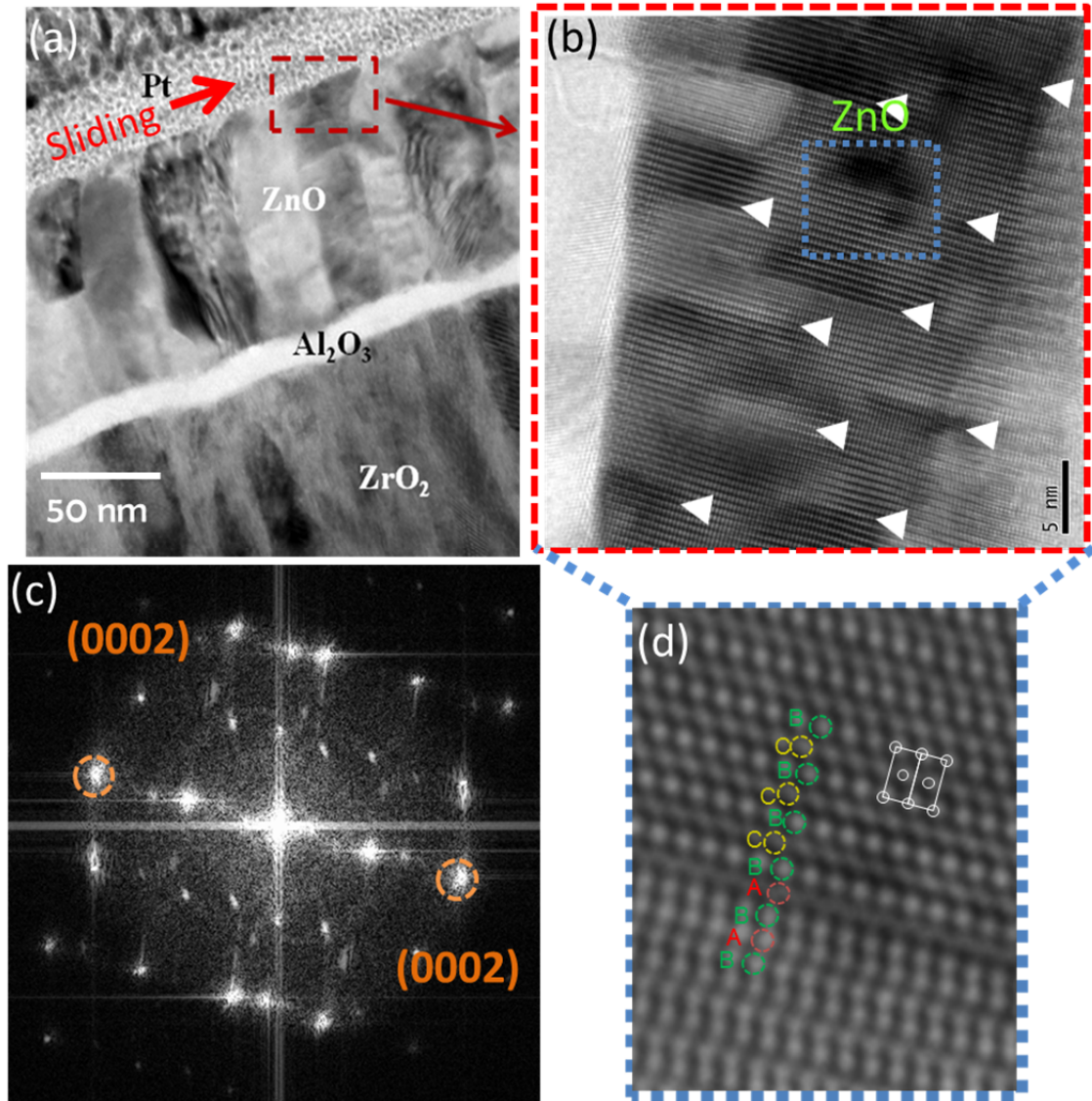

Figure 4.18: Cross-sectional HRTEM micrographs of the worn ALD ZnO nanolaminate that show (a & b) region with high density of sliding-induced basal stacking faults, (c) corresponding FFT pattern that shows the smeared {0002} reflections, and (d) the transition in stacking sequence for type-I intrinsic ZnO stacking fault from ABAB to CBCB.
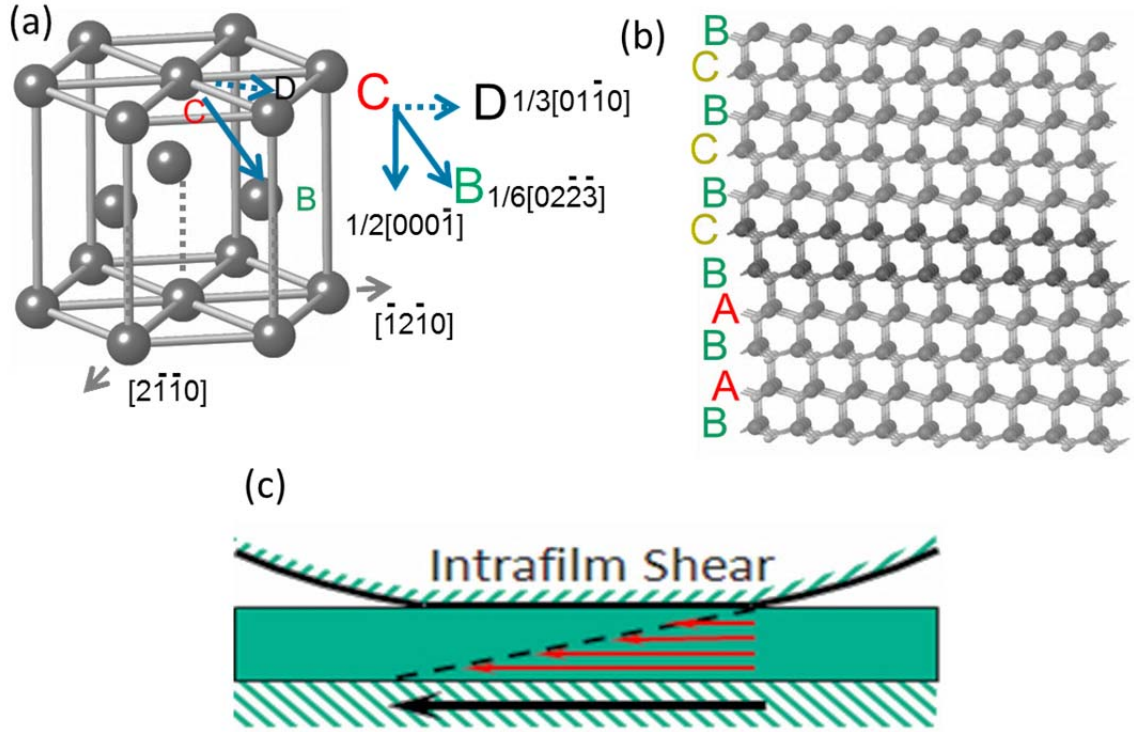
Figure 4.19: (a) Intrinsic type I basal plane stacking fault in wurtzite ZnO, (b) VASP generated stacking fault sequence, and (c) velocity accommodation mode of intrafilm shear where dislocation glide is active on ZnO {0002} basal planes during sliding.

4.4 Nanoindentation Analysis of Si wafer Coated with ALD ZrO_2 and ALD Trilayer

In order to compare and contrast the tribological properties to mechanical properties, nanoindentation was performed on the ALD coatings. Elastic modulus (E) and hardness (H) of ~200nm thick ALD coatings (monolayer ALD ZrO_2 and one ALD trilayer ZnO /Al_2O_3/ ZrO_2) were measured by using a Nanoindenter XP system from MTS Corporation. A diamond Berkovich indenter tip with radius of ~50nm, which is preferred for low-load indentation testing, was employed for the indentation studies. The continuous stiffness measurement (CSM) option was used to obtain E and H with respect to indentation depth during the indenting, based on the indentation method that was

originally proposed by Oliver and Pharr [16]. Prior to each set of indentation tests, experimental parameters such as the tip area function and frame compliance were calibrated by using a standard fused silica specimen.

To minimize the influence of substrate on the hardness and elastic modulus result, the load for indentation is chosen in such a way that the indentation depth is 10-20% of the film's thickness (e.g. 10-20nm indentation depth for a 100nm thick-film) [17, 18] [16, 17], as a rule-of-thumb, but the output of the test for indentation depths less than 100 nm on ALD coatings were not reliable. Furthermore, it is almost impractical to have a free-standing ALD films without any substrate. Hence, indentation depths of 100 nm and 200 nm were conducted for each of the ALD coated Si samples and the Poisson's ratio was set as 0.3 for the ALD films. To increase the level of accuracy several indents were made on each sample and the average E and H were calculated from the tests. The indents were sufficiently separated at 50 μm to prevent the overlap and interaction of strain fields.

Figs. 4.20 and 4.21 show the displacement dependence of H and E for 36 and 16 nanoindentation tests at a depth of 100 nm conducted on ~200 nm thick ALD ZrO_2 (Deposition 1) and ALD $ZnO/Al_2O_3/ZrO_2$ (Deposition 3) films on Si substrates , respectively. The indentation depth of 100 nm was chosen to avoid contributions from the underlying substrate.

From the figures, there is an increase in H and E with increasing indenter penetration depth. The absolute values of H and E at low indentation depths are affected by the changes in shape of the indenter tip (i.e. tip blunting), which makes quantification difficult. Furthermore, it is difficult to separate out the H and E contributions from the

ALD coatings from that of the Si substrate since they have similar reported H (9 to 12 GPa) and E (180 to 200 GPa) values.
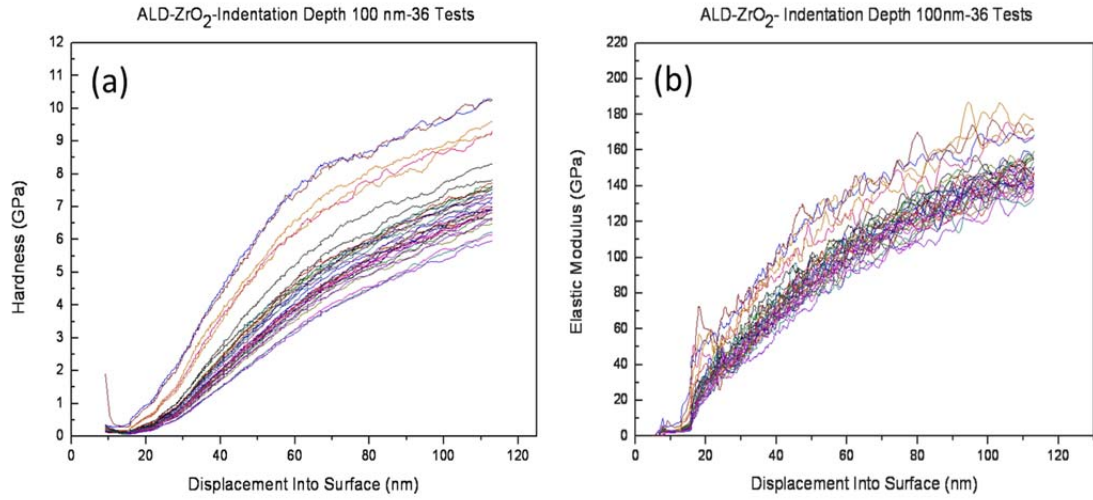

Figure 4.20: Variation in (a) hardness and (b) elastic modulus for ~200 nm thick ALD ZrO$_2$ coating deposited on Si wafer.
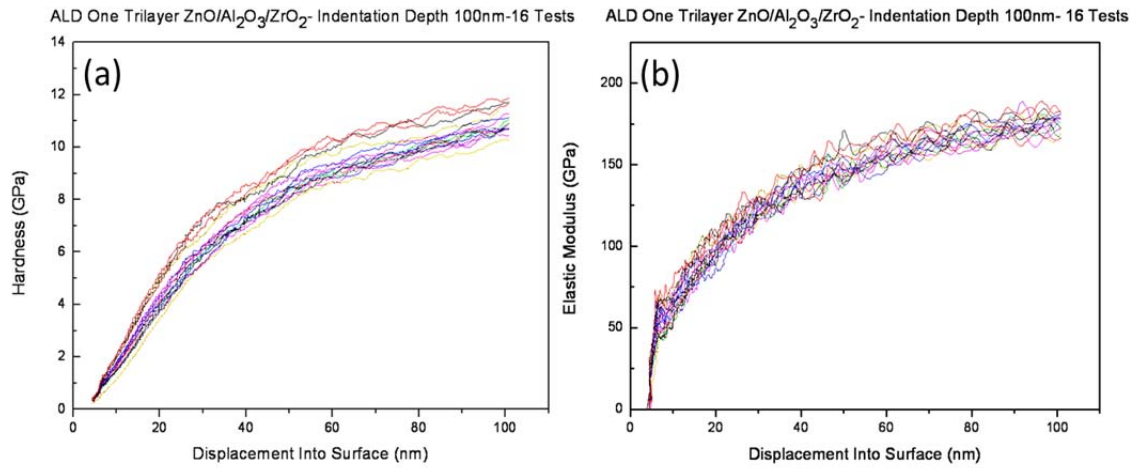

Figure 4.21: Variation in (a) hardness and (b) elastic modulus for ~200 nm thick ALD nanolaminate ZnO/Al$_2$O$_3$/ZrO$_2$ coating deposited on Si wafer.

Thus, a qualitative comparison between H and E values of ALD ZrO_2 and ALD one trilayer $ZnO/Al_2O_3/ZrO_2$ revealed that the ALD trilayer exhibits increased H and E values at any given indentation depth, suggesting it has higher H and E. This can be related to the using the tough ALD ZrO_2 after the Si substrate in the ALD trilayer that can impede the deformation.

4.5 Friction Behavior: Comparison between ALD ZnO with Textured Grains vs. ZnO Single crystals and ZnO with Randomly Oriented Grains

In order to further elucidate the underlying mechanisms that are responsible for tribological enhancement in ZnO, nanocrystalline textured grains (ALD ZnO), nanocrystalline randomly orientated grains, and single crystals of different orientations ($\{0001\}$-basal plane and $\{1\bar{1}00\}$-prismatic plane) were subjected to the unidirectional sliding test (POD) with linear speed 2.1 cm/s, hanging load 200g against a Si_3N_4 ball. Five POD tests with identical condition were conducted for each sample. After POD testing was completed, cross-sectional TEM investigations inside the worn surfaces were revealed the deformation behavior and mechanisms for each ZnO sample.

It was reported in section 4.3.2 that ALD ZnO provides solid lubricity by showing a low steady-state friction coefficient (μ_{ss}) of ~0.14 to 0.16. The high resolution cross-sectional TEM investigations of the crystalline region of deformed ZnO layer inside the wear track (Fig 4.18) revealed the existence of ZnO type I intrinsic basal plane stacking faults. These stacking faults are known to be responsible for discernible localized plasticity in the nano-columnar ZnO grains via a dislocation glide mechanism. Solid lubricity of ALD ZnO is attributed to activating subsurface basal stacking faults that will

116

promote intrafilm shear/slip and consequently lower friction and wear. In the following sections the tribological behavior of ALD ZnO will be compared to ZnO single crystals and nanocrystalline ZnO with randomly oriented grains.

4.5.1 Single-Crystal ZnO with {0001}-Basal Plane Orientation

The variation of friction coefficient with respect to the distance that Si_3N_4 ball travelled for 200 m on the single-crystal ZnO-{0001} is shown in Fig 4.22. After the run-in section out to ~25 m of sliding, the average steady-state friction coefficient (μ_{ss}) of ~0.5 is clear from the steady-state friction regime.
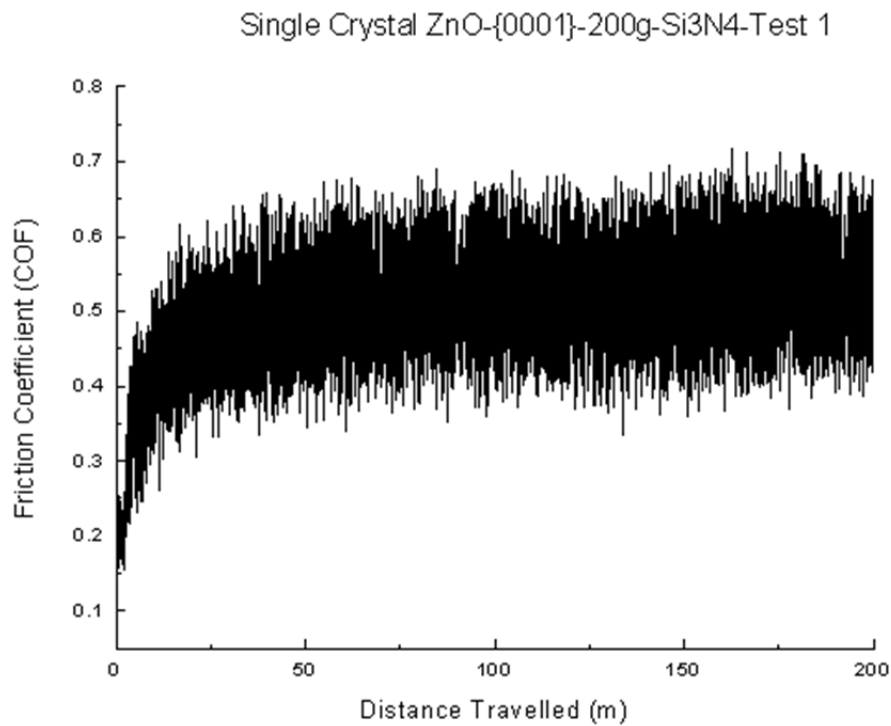

Figure 4.22: Friction coefficient for the single crystal ZnO-{0001} from unidirectional sliding POD test.

This is a much higher friction coefficient compared to ALD ZnO (μ_{ss} of ~0.14 to 0.16) under the same testing conditions. The optical images of the worn surfaces are shown in Fig 4.23. It is clear that the amount of wear on the ball as well as the wear track is appreciable for single crystal ZnO-{0001}. The width of the wear track is approximately ~400µm from the SEM micrographs in Fig. 4.24. It is obvious that the brittle (cleavage) fracture behavior of the single crystal ZnO-{0001} gives rise to high wear and high friction coefficient. The contact stress must be high enough to break Zn-O bonds along the basal planes. The SEM images show platelet (flake-like) wear debris in the track indicative of a delamination-type wear mechanism where the high cyclic compressive stresses during sliding result in surface fatigue. In this wear mechanism, subsurface cracks run parallel to the surface, and when the crack reaches a critical length, it breaks through to the surface and leads to eventual detachment of long thin wear particles. Since the crack grows parallel to the surface at a shallow depth, wear particles formed by delamination wear will be relatively long and thin.
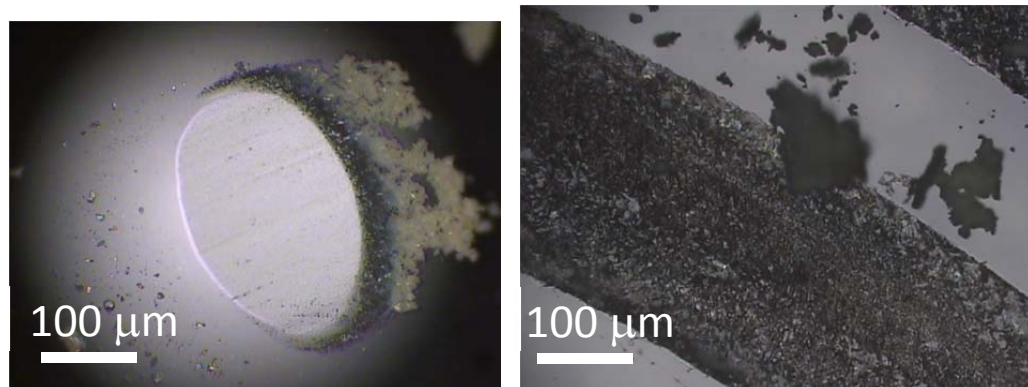

Figure 4.23: Optical images of the Si_3N_4 ball (left) and wear track (right) after POD test on single crystal ZnO-{0001}.

Cross-sectional TEM micrographs shown in Fig 4.25(a) and (b) show the structure of single crystal ZnO-{0001} prior to the sliding wear POD test. From Fig. 4.25(c), sharp diffraction spots in FFT pattern clearly indicate basal plane reflections with inter-planar spacing of 2.609Å that represent (0002) plane. Similar reflection peaks were also observed from the XRD analysis.
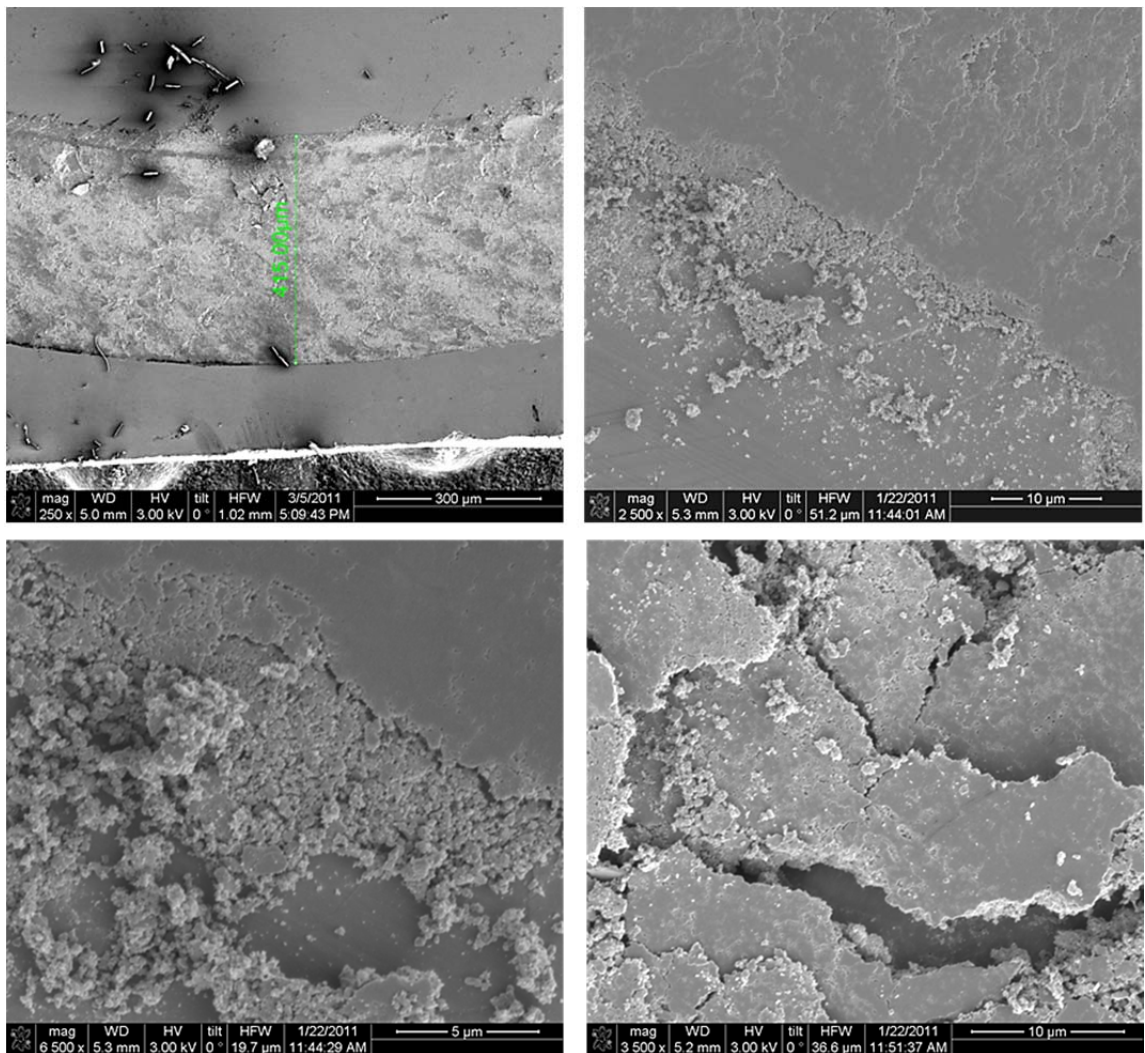

Figure 4.24: SEM micrographs of the wear track showing brittle (cleavage) fracture of single crystal ZnO-{0001} after POD test and formation of platelet (delamination) wear debris.

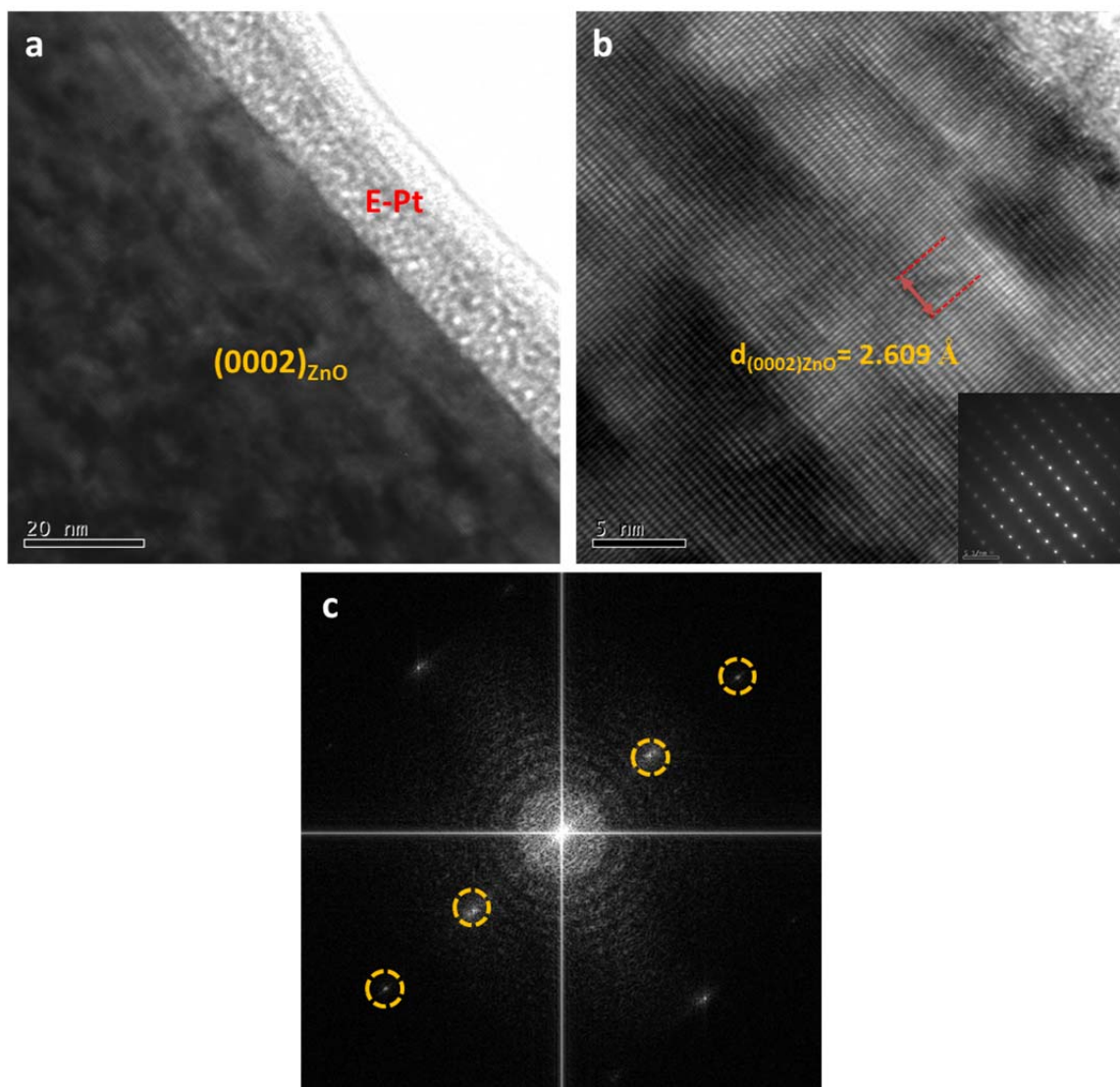Figure 4.25: (a) Cross-sectional TEM micrographs of the single crystal ZnO-{0001} before POD unidirectional sliding test, (b) a HRTEM micrograph that clearly shows the inter-planar spacing between {0002} planes and inset of the corresponding SAED pattern with non-diffuse and sharp diffraction spots and (c) corresponding FFT pattern with first and second order reflection of basal planes.
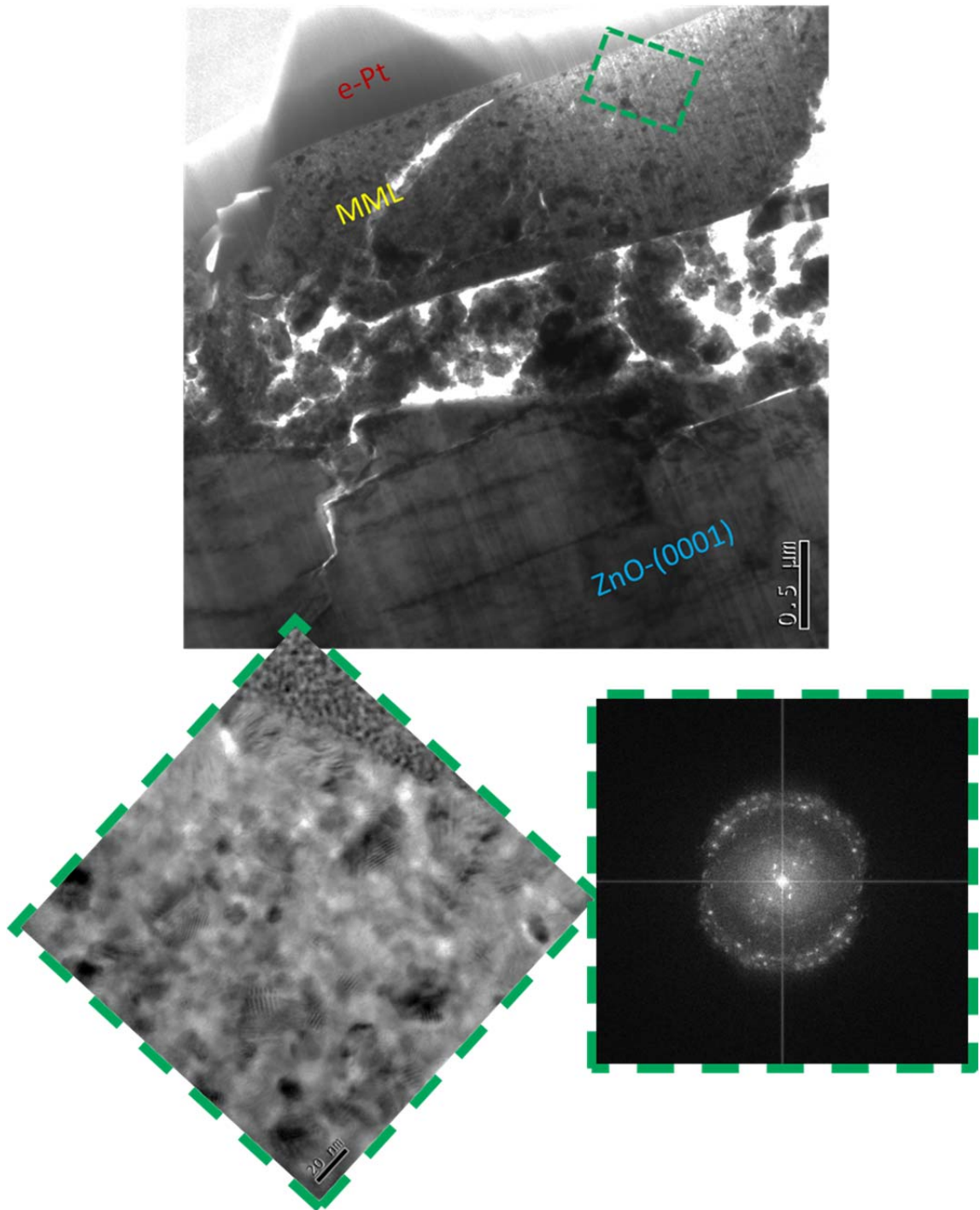
Figure 4.26: Cross-sectional TEM micrographs of the single crystal ZnO-{0001} after POD unidirectional sliding test showing the formation of a mechanically mixed layer (MML) on the wear surface on top of the subsurface cleavage cracks. The corresponding SAD pattern shows randomly orientated grains in the MML.

After POD sliding was completed, cross-sectional TEM was performed inside the wear tracks to determine the wear behavior and mechanisms. Fig. 4.26 clearly shows that the subsurface shear (compressive) stress during POD sliding wear resulted in formation of a mechanically mixed layer (MML) on the surface of the single crystal ZnO-{0001}. The corresponding FFT pattern contains numerous reflections and diffused rings which are clear indication of randomly oriented nanocrystalline grain. Furthermore STEM-HAADF and EDS analyses of the MML layer (Fig 4.27) revealed the presence of a small amount of Si and O (~150 nm in thickness) which was tribochemically (SiO_x) transferred from the Si_3N_4 ball onto the wear track during the POD test. This is in good agreement with optical image of the Si_3N_4 ball shown in Fig 4.23 where the surface of the ball was heavily abraded by ZnO. After this layer, bulk ZnO composition is shown by the EDS line scan.

In dramatic contrast to ALD ZnO, the deformation mechanism in single crystal ZnO-{0001} did not involve any plastic deformation, since cross-sectional TEM analysis of the structural features beneath the mechanically mixed layer exhibited cracks of various size with similar propagation pattern (Fig 4.28). These cracks are known as cleavage cracks that change their propagation direction along ZnO basal and prismatic planes.

The cleavage cracks along basal (0002) and prismatic (10-10) and (11-20) planes are responsible for brittle (cleavage) fracture and higher friction/wear. Also, unlike ALD nanocolumnar ZnO coatings, the single crystal does not exhibit grain boundaries, and, thus there are no available basal stacking faults/partial dislocations originating at low

122

angle columnar grain boundaries, as previously shown for the ALD ZnO coating in Fig. 4.l8 (b). Thus, there is no pathway for intrafilm shear/slip to occur that results in low friction and wear. To summarize, although the ALD ZnO coatings and ZnO single crystal have the same c-axis {0002} orientation, the role of grain boundaries (2-D defect) and increased basal stacking faults/partial dislocations (1-D defect) are responsible for the resultant friction and wear behavior.
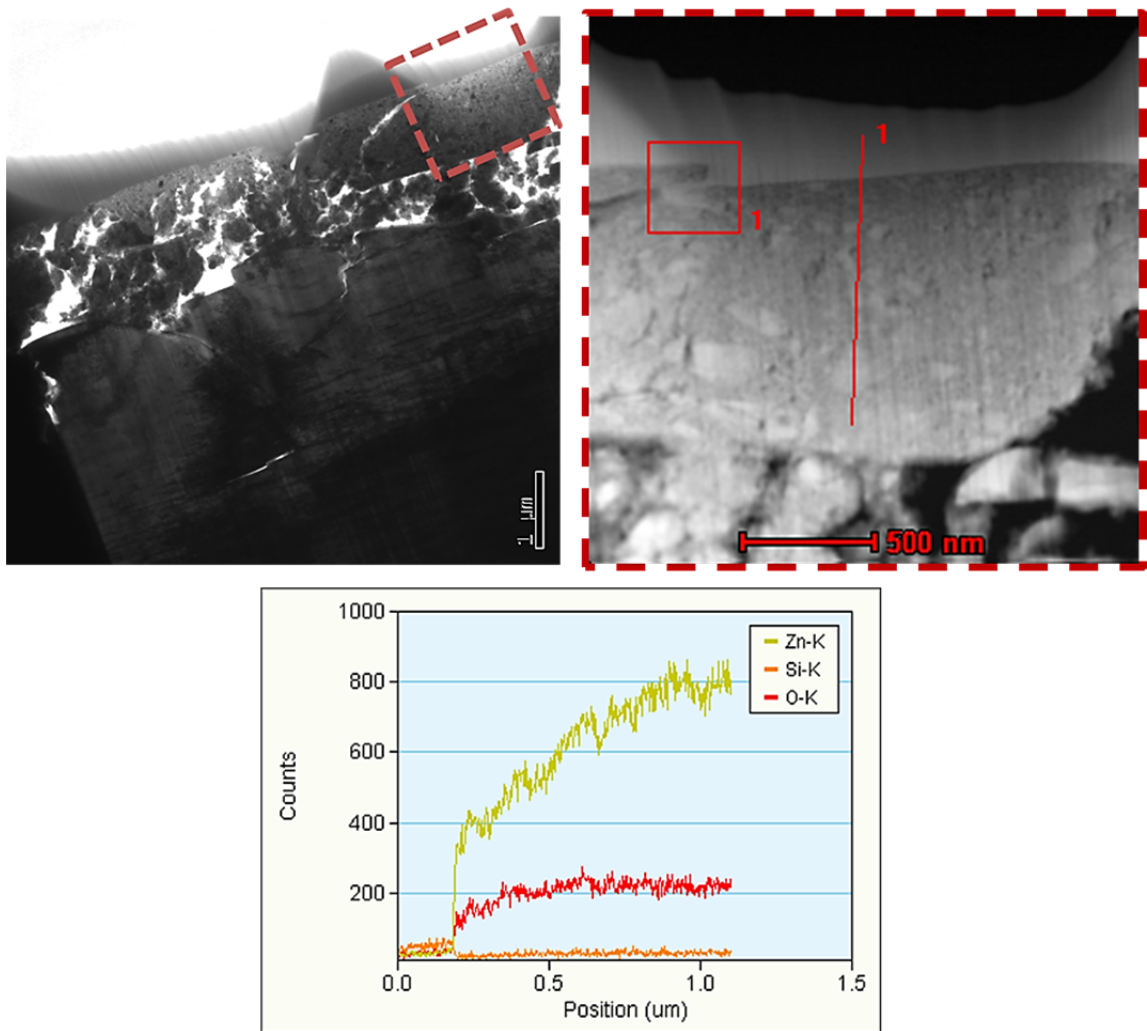

Figure 4.27: EDS drift-corrected line scan conducted in STEM mode by using HAADF detector shows the existence of silicon in the mechanically mixed layer after POD test.
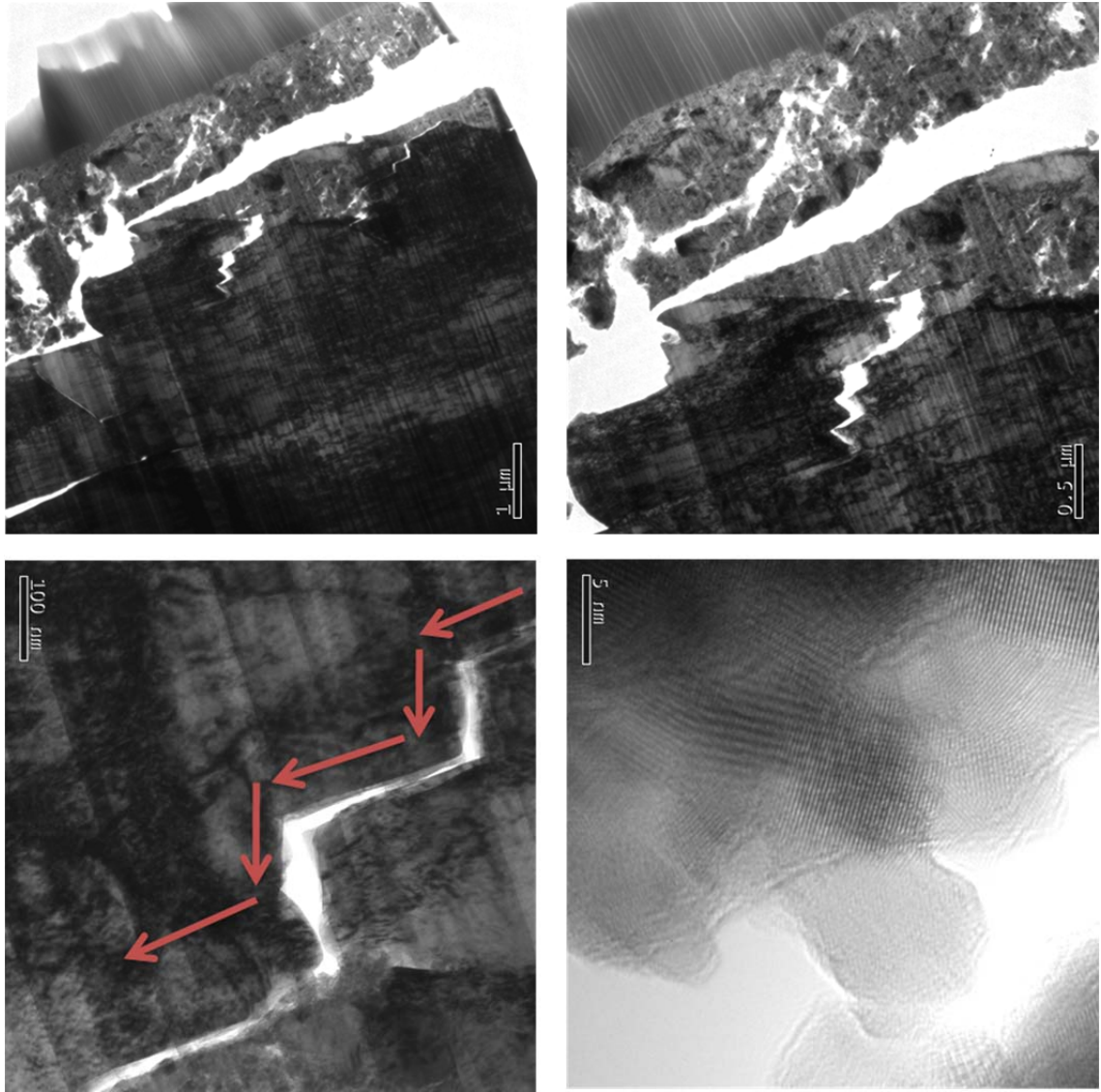
Figure 4.28: Cross-sectional TEM micrographs that represent the propagation pattern of cleavage cracks along the ZnO basal and prismatic planes.

4.5.2 Single-Crystal ZnO with {1$\bar{1}$00}-Prismatic Plane Orientation

Fig 4.29 shows the variation of friction coefficient with respect to the distance that Si_3N_4 ball travelled for 200 m on the single-crystal ZnO-{1$\bar{1}$00}. After the run-in section out to ~30 m of sliding, the average steady-state friction coefficient (μ_{ss}) of ~0.4 is clear from the steady-state friction regime.
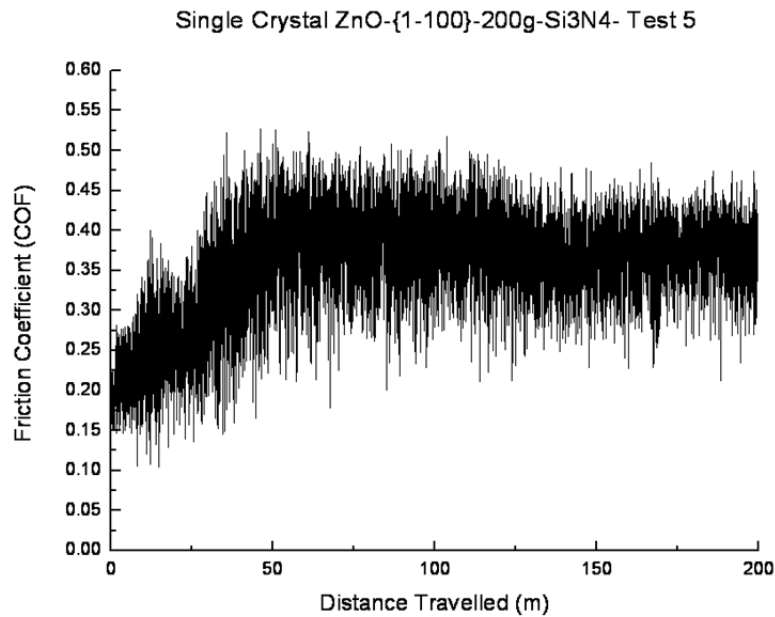

Figure 4.29: Friction coefficient for the single crystal ZnO-{1$\bar{1}$00} from unidirectional sliding POD test.

This is single crystal orientation also exhibits a much higher friction coefficient compared to ALD ZnO (μ_{ss} of ~0.14 to 0.16) under the same testing conditions, but slightly lower than the {0001}-orientated ZnO single crystal. Fig. 4.30 shows the optical images of the worn surfaces (Si_3N_4 ball and the wear track) after the POD test on single crystal ZnO-{1$\bar{1}$00}. Wear debris are clearly seen on the trailing edge of the Si_3N_4 ball

125

and either side of the wear track. In addition to wear debris, a large crack crossed the entire width of the wear track as shown in Fig 4.30(b), indicative of severe brittle fracture.   The width of the wear track is approximately ~400μm from the SEM micrographs in Fig. 4.31, similar to single crystal {0001}. Like single crystal ZnO-{0001}, it is obvious that the brittle (cleavage) fracture behavior gives rise to high wear and high friction coefficient. The SEM images in Fig. 4.31 also show platelet (flake-like) wear debris in the track indicative of a delamination-type wear mechanism.
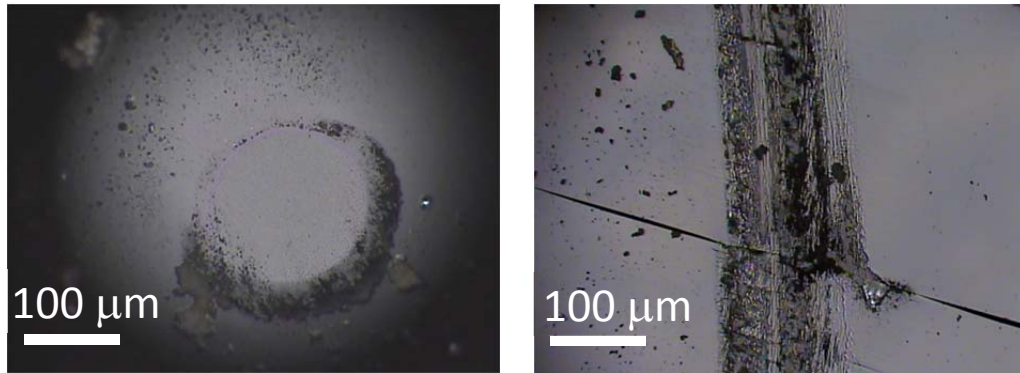

Figure 4.30: Optical images of the Si_3N_4 ball (left) and wear track (right) after POD test on single crystal ZnO-$\{1\bar{1}00\}$.

Fig 4.32 shows cross-sectional TEM images of single crystal ZnO-$\{1\bar{1}00\}$ prior to the POD sliding wear test. The inset SAED pattern clearly shows the diffraction spots along the [0001] zone axis that indicate prismatic plane reflections with inter-planar spacing of 2.807Å. Since the wear track morphology, platelet delamination wear debris and friction coefficient were similar to the single crystal {0001} sample, no cross-sectional TEM was performed inside the wear tracks after POD sliding was completed.
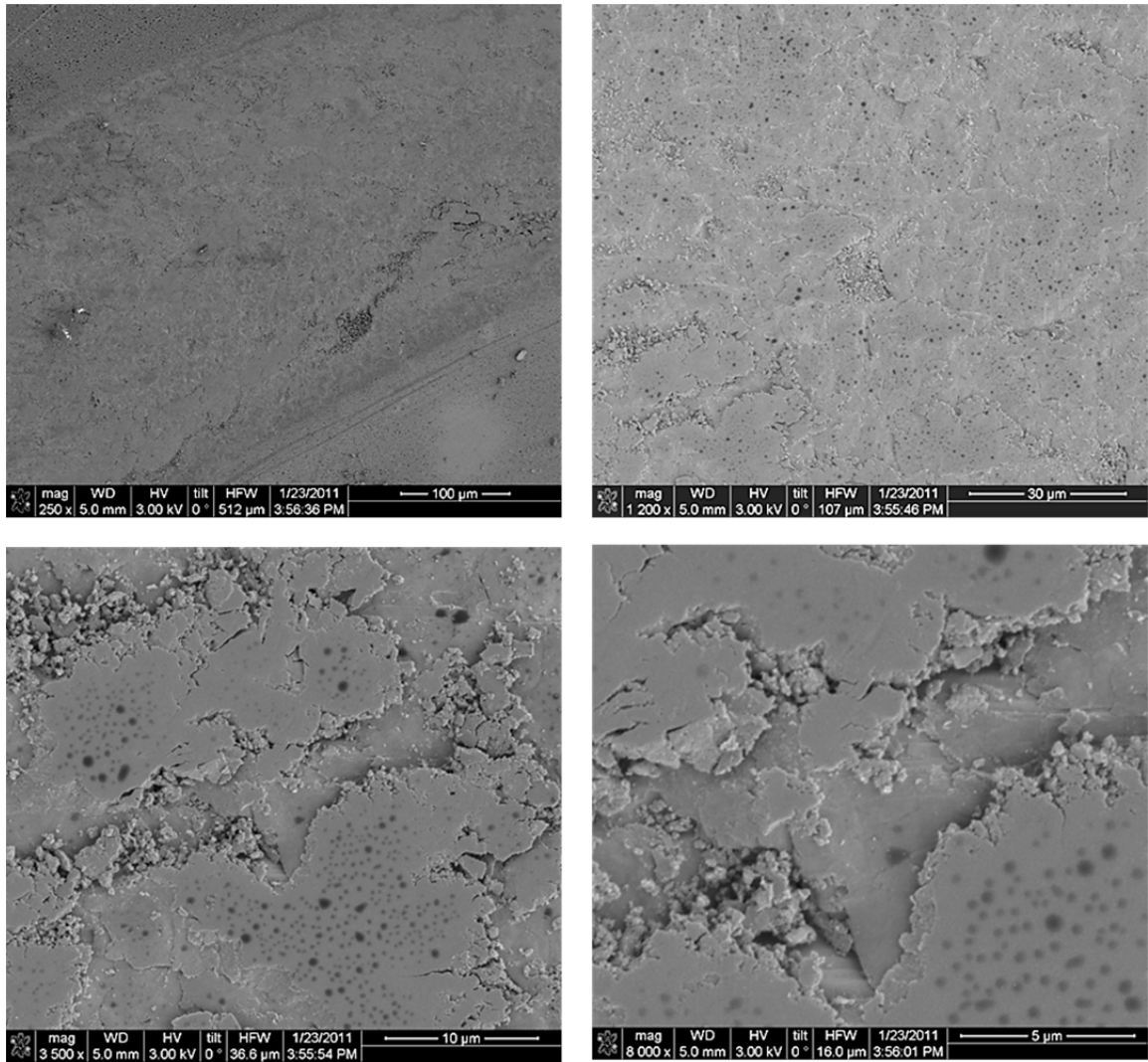
126

Figure 4.31: SEM micrographs of the wear track showing brittle (cleavage) fracture of single crystal ZnO-{1$\bar{1}$00} after POD test and formation of platelet (delamination) wear debris.
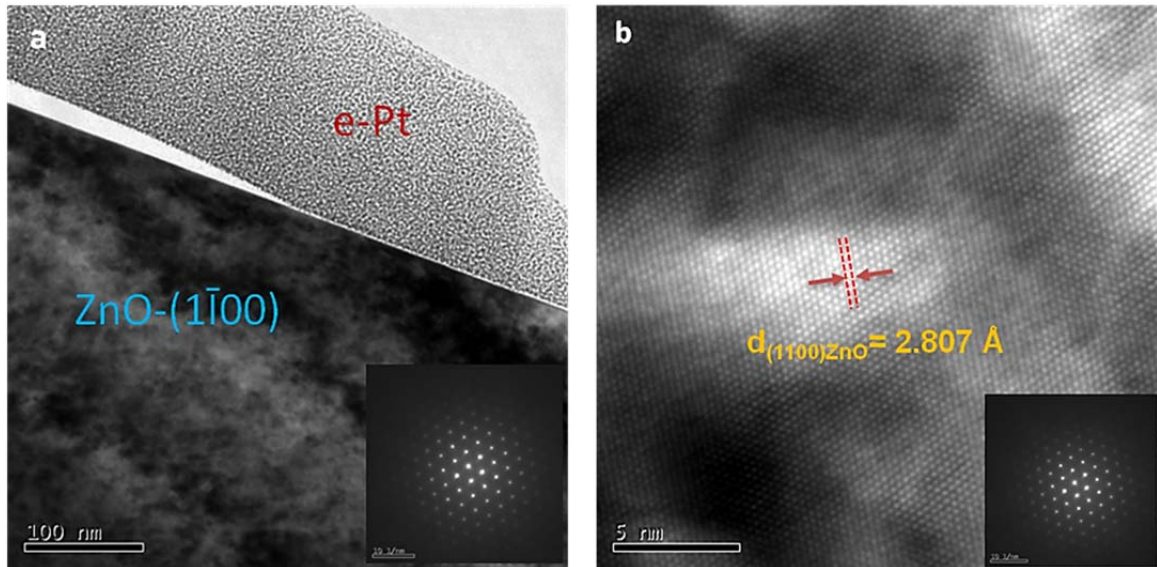
Figure 4.32: (a) Cross-sectional TEM micrographs showing single crystal ZnO-{1$\bar{1}$00} before POD sliding wear test, (b) a HRTEM micrograph that clearly shows the inter-planar spacing between {1$\bar{1}$00} planes.

4.5.3 Nanocrystalline ZnO with Randomly Oriented Grains

The random orientation of the grains in this nanocrystalline ZnO sample are shown by XRD analysis (Fig 4.33) and almost all the expected reflection ranges from 31 to 90º Bragg angle are present in the XRD scan. Using the Debye-Scherer equation, the grain size was estimated to be at ~ 50 nm. Similarly cross-sectional TEM micrographs in bright field and central dark field modes with SAED pattern, which were taken from the as-received sample, in Fig 4.34 clearly confirm the existence of randomly oriented grains. These cross-sectional TEM micrographs are in agreement with XRD showing randomly orientated nanocrystalline ZnO grains.
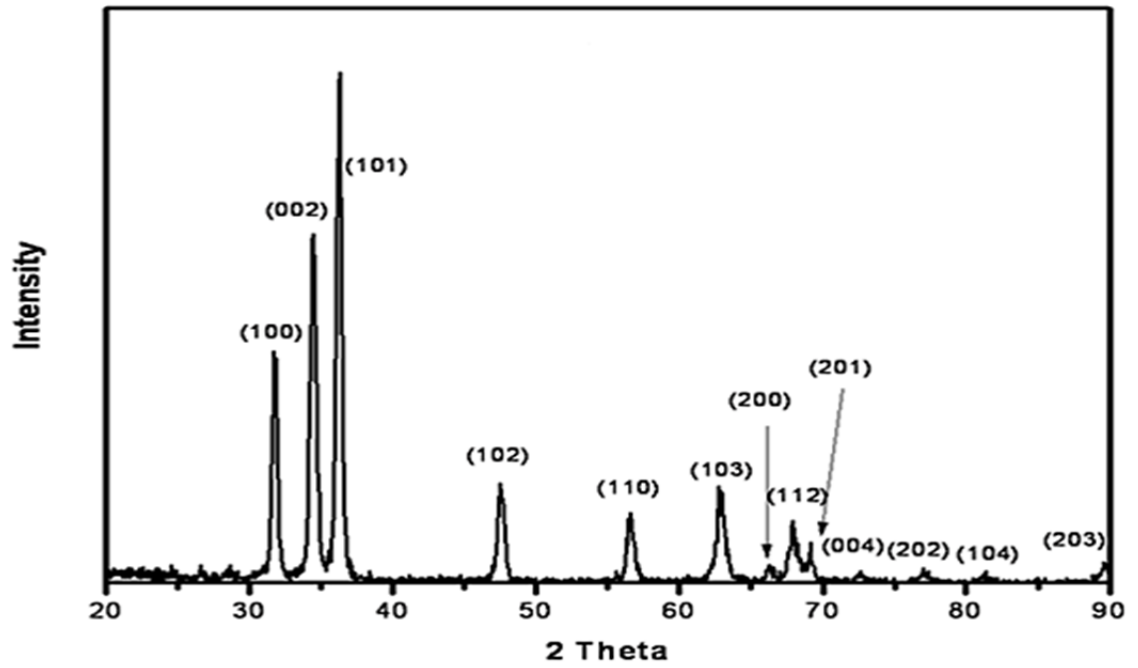
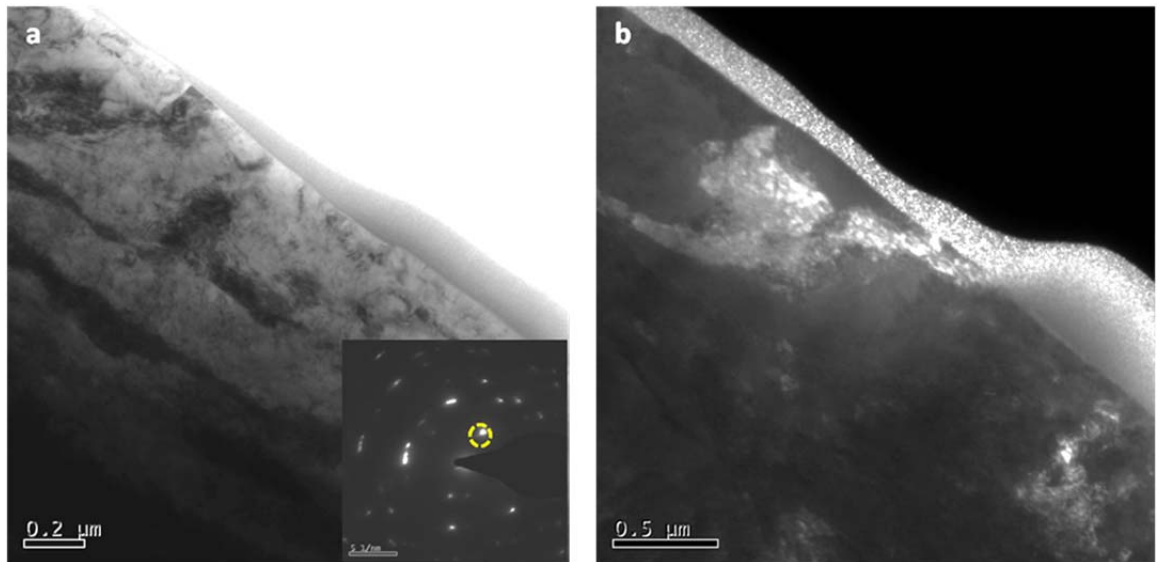Figure 4.33: XRD scan of randomly orientated ZnO nanocrystalline grains.

Figure 4.34: Cross-sectional TEM micrograph (a) BF image with SAED pattern show randomly oriented nanocrystalline of ZnO and (b) central DF micrograph corresponds to the circled reflection in SAED pattern.

The average friction coefficient from the steady-state section of the graph in Fig 4.35 is ~0.4 for nanocrystalline ZnO with randomly oriented grains. Fig. 4.36 shows optical images of significant ball wear and wear track debris. SEM micrographs in Fig 4.37 show wear debris and surface cracks inside the wear track of width ~ 400 μm, similar to the previously mentioned single crystals. Also this ZnO sample with polycrystalline randomly orientated grains has multiple slip systems operative but not the most favorable, single (0002)-orientated slip system. This is important since there is only basal slip in ALD ZnO (no interacting slips systems) which translates to low interfacial shear (friction).
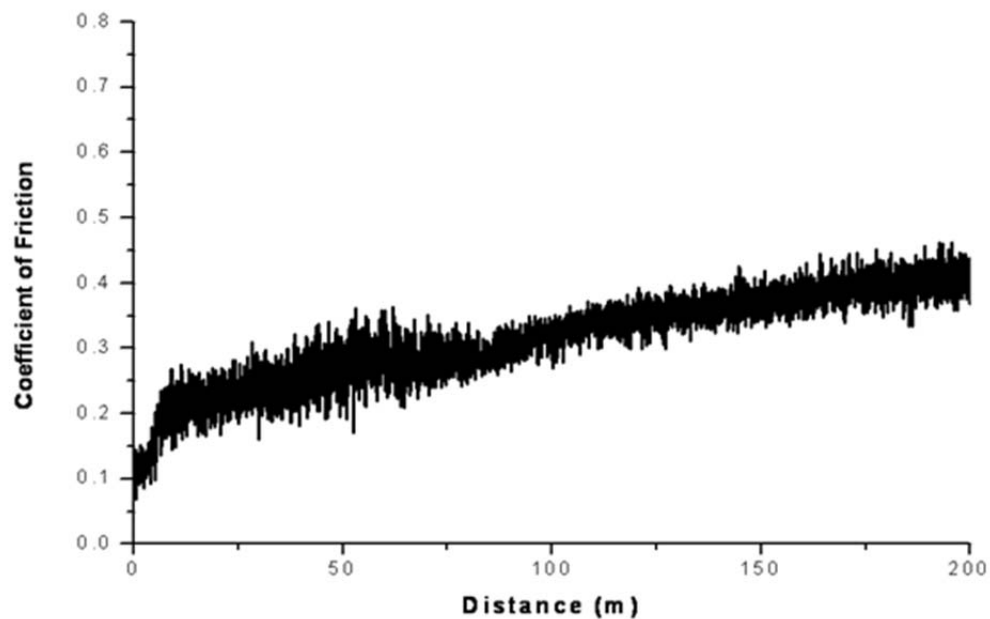

Figure 4.35: Friction coefficient for nanocrystalline ZnO with randomly oriented grains from unidirectional sliding POD test.
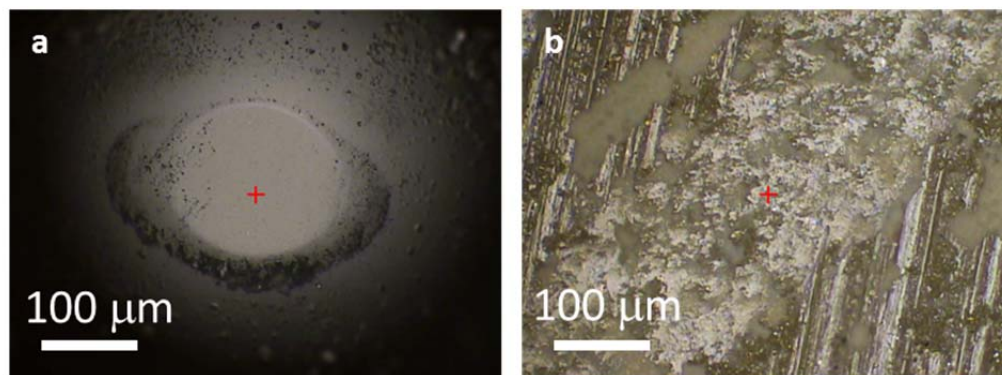
Figure 4.36: Optical images of the Si_3N_4 ball (left) and wear rack (right) after POD test on nanocrystalline ZnO with randomly oriented grains.

Table 4.3: Comparison between friction coefficient of atomic layer deposited ZnO, single crystals of ZnO and randomly oriented ZnO nano-crystals

Sample	Steady-State Friction Coefficient
ALD textured ZnO {0002} nanocrystalline grains	0.2
Single Crystal ZnO-{0001}	0.5
Single Crystal ZnO-{1$\bar{1}$00}	0.4
Randomly oriented ZnO nanocrystalline grains	0.4

To summarize, the lowest friction coefficient (~0.2) was observed in pure sliding for ALD textured ZnO {0002} nanocrystalline grains in comparison to single crystal ZnO-{0001} (~0.5), single crystal ZnO-{1$\bar{1}$00} (~0.4) and randomly oriented ZnO nanocrystalline grains (~0.4) (Table 4.3).
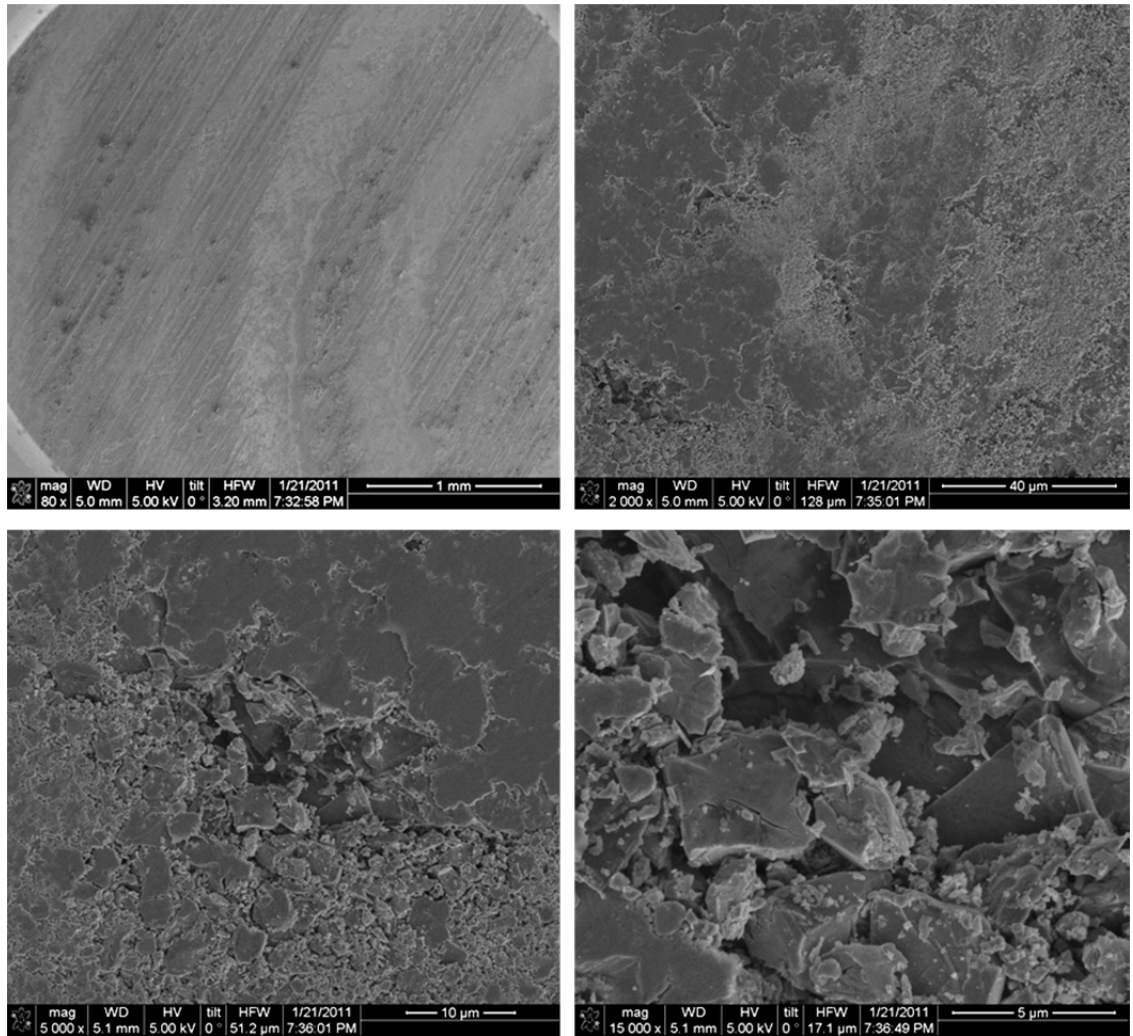
Figure 4.37: SEM micrographs of the wear track showing brittle fracture of nanocrystalline ZnO with randomly oriented grains after POD test and formation of platelet (delamination) wear debris.

Traditionally, wear processes have been classified into various types such as abrasive, adhesive and fatigue. However based upon the successful indentation fracture mechanics which apply to static conditions, a theory of wear in brittle solids has been proposed [19]. The propagation of the lateral-type cracks was addressed as the main reason for chipping of materials and consequently formation of wear particles. Furthermore, it was shown that the process of wear formation by adhesion, fretting and

fatigue all require nucleation, pile-up, motion and interaction of dislocations with obstacles such as grain boundary [20, 21].

The brittle fracture behavior responsible for high wear and high friction coefficient ($\sim$ 0.4) is clear from the high resolution SEM micrographs in Fig 4.37, where faceted and delaminated wear particles were created due to the interaction of dislocations with grain boundaries of nanocrystalline randomly orientated grains that have multiple interactive slip systems. In addition, significant wear and high friction coefficient were observed from the single crystals of ZnO-$\{0001\}$ and ZnO-$\{1\bar{1}00\}$, where there was not any grain boundaries and sources of basal or prismatic stacking faults present for dislocations to interact with or glide. The cross sectional TEM analyses of ZnO-$\{0001\}$ in Fig 4.28 showed that high interfacial shear cannot find any path, such as grain boundaries to accommodate along it, which lead to crack nucleation and propagation. These cracks prefer to spread in certain crystallographic orientations by changing the cleavage plane.

Similar subsurface damage due to single-pass friction tests was reported by Adewoye and Page [22] for single crystal SiC with $\{0001\}$ orientation. Their TEM investigations revealed two major slip systems of $\{0001\} <11$-$20>$ and $\{h0$-$h1\} <2$-1-$10>$ that dominated the deformation, however, both the $\{10$-$10\}$ and $\{11$-$20\}$ cleavage planes controlled the failure.

Although the overall damage mechanism for bulk microcrystalline and single crystal ceramics is known to be brittle (cleavage) fracture, evidence of localized nanocrystalline plasticity in ALD ZnO (Fig 4.18) is shown for the first time where only

the basal slip system is active. The partial dislocation and stacking faults acting along these basal planes are activated by subsurface slip via the 'intrafilm shear' velocity accommodation mode.

4.6 Chapter Summary

Monolayer ZrO_2 coating and trilayer nanolaminate $ZnO/Al_2O_3/ZrO_2$ coating were infiltrated into carbon-carbon composite by application of atomic layer deposition to enhance oxidation resistance and wear resistance. These coatings exhibited excellent conformality and pore-filling capabilities into the carbon-carbon composite and carbon foam. The tribological investigations, included pin-on-disc unidirectional sliding wear tests, exhibited a significant reduction for sliding friction and wear factor compared to the uncoated carbon-carbon composite. Characterization of unworn and worn surfaces was performed by energy dispersive x-ray spectroscopy (EDS) mapping in SEM, transmission electron microscopy (TEM), STEM/HAADF, and X-ray diffraction (XRD). EDS maps showed that the depth that ALD-ZrO_2 penetrated into the CCC is dependent on the exposure time of ZrO_2 precursors. High resolution TEM (HRTEM) and corresponding XRD analysis determined the textured crystalline phases of (0002) graphite and (101) ZrO_2 (tetragonal) and (0002)-orientated grains of wurtzite ZnO. Unlike the monolayer of ALD ZrO_2, the trilayer coating of ALD $ZnO/Al_2O_3/ZrO_2$ provided lubricity to carbon-carbon composite by reduction in friction coefficient and wear. High resolution transmission electron microscopy investigations on ALD ZnO revealed that the {0002} basal planes in wurtzite ZnO, accommodate the shear strains by dislocation glide along the basal planes. Further HRTEM investigations conducted on various ZnO samples for

134

additional determined the deformation and failure mechanisms in ALD ZnO. These samples included single crystal ZnO with {0001} orientation, single crystal ZnO with {1$\bar{1}$00} orientation and nanocrystalline ZnO with randomly oriented grains. In brief the following are the summary and conclusions of results:

- ALD ZrO_2 infiltration into CCC caused ~34% reduction in wear factor compared to uncoated CCC. Also employing longer exposure time of ALD ZrO_2 precursors led to uniform closure of subsurface pores and further wear decrease to ~51%. A further reduction in wear rate and higher thermal resistance is anticipated with the conversion of the ALD ZrO_2 and CCC interface to hybrid layer of ZrC by means of carbothermal reduction.

- ALD exhibited superior capabilities in deposition of conformal and uniform nanolaminates with sharp interfaces without any intermixing. This behavior is more noticeable for subsurface porosities that were filled with sequential and conformal layer of nanolaminates.

- Improvement in friction and wear behavior was observed with ALD infiltration of trilayer $ZnO/Al_2O_3/ZrO_2$ nanolaminates into CCC and on Si substrates. The lowest friction coefficient (~0.2) was observed in pure sliding for ALD textured ZnO {0002} nanocrystalline grains in comparison to single crystal ZnO-{0001} (~0.5), single crystal ZnO-{1$\bar{1}$00} (~0.4) and randomly oriented ZnO nanocrystalline grains (~0.4).

- A high density of ZnO sliding (shear)-induced stacking faults were observed inside the wear tracks of the worn ALD trilayer (in comparison to unworn nanolaminates)

which are responsible for solid lubrication. This is in contrast to the single crystals which exhibit lower stacking fault densities (no grain boundary sources) and undergo brittle fracture that are responsible for higher friction. Also the ZnO sample with polycrystalline randomly orientated nanocrystalline grains has multiple slip systems operative but not the most favorable, single (0002)-orientated slip system.

- Activating subsurface basal stacking faults that are bordered by partial dislocations will promote intrafilm shear/slip and hence improve friction. The slip of partial dislocations likely resulted from a dislocation glide process, but in situ techniques, such as probe sliding in the TEM, are needed to visualize these events.

- Intrafilm shear with a friction induced subsurface (mechanically mixed layer) also aided in shear accommodation by preventing brittle fracture.

- Nanoindentation analysis on the ALD ZrO_2 and ALD one trilayer $ZnO/Al_2O_3/ZrO_2$ deposited on Si wafer revealed that the ALD trilayer exhibited higher resistance to static loading, which is a further benefit of this trilayer coating.

Therefore based on these results and mechanisms, ALD $ZnO/Al_2O_3/ZrO_2$ nanolaminates are good candidates for providing low friction and wear and potentially high thermal (oxidation) resistant surfaces and interfaces in moving mechanical assembles, such as MEMS devices and CCC bushings that experience wear and surface damage.

4.7 Chapter References

1. *ACF-10Q.* 2010; Available from: http://www.poco.com/MaterialsandServices/Graphite/IndustrialGrades/ACF10Q/tabid/88/Default.aspx.

2. Sheppard, R.G., D.M. Mathes, and D.J. Bray, *Properties and Characteristics of Graphite for Industrial Applications*2001: POCO Graphite, Inc.

3. *Zirconium Oxide (Zirconia ZrO_2 TTZ YTZP) Material Properties*.

4. *Poco Graphite HTC Graphite* Available from: http://www.matweb.com/search/datasheet.aspx?matguid=ba4c46c7ffc44fc5b7a4595abb910002.

5. Ritala, M. and M. Leskelä, *Atomic layer deposition*, in *Handbook of Thin Films*, N. Hari Singh, M.Sc, and Ph.D, Editors. 2002, Academic Press: Burlington. p. 103-159.

6. Abelson, J.R., et al., *Methods for coating and filling high aspect ratio recessed features* U.S. Patent, Editor 2009, The Board of Trustees of the University of Illinois (Urbana, IL, US)

7. Knez, M., K. Nielsch, and L. Niinistö, *Synthesis and Surface Engineering of Complex Nanostructures by Atomic Layer Deposition.* Advanced Materials, 2007. 19(21): p. 3425-3438.

8. Cassir, M., et al., *Synthesis of ZrO_2 thin films by atomic layer deposition: growth kinetics, structural and electrical properties.* Applied Surface Science, 2002. 193(1-4): p. 120-128.

9.   Kukli, K., M. Ritala, and M. Leskelä, *Low-Temperature Deposition of Zirconium Oxide–Based Nanocrystalline Films by Alternate Supply of Zr[OC(CH₃)₃]₄ and H₂O.* Chemical Vapor Deposition, 2000. 6(6): p. 297-302.

10. Kukli, K., et al., *Atomic layer deposition of zirconium oxide from zirconium tetraiodide, water and hydrogen peroxide.* Journal of Crystal Growth, 2001. 231(1-2): p. 262-272.

11. Banerjee, S. and P. Mukhopadhyay, *Phase transformations: examples from titanium and zirconium alloys.* 1 ed2007: Elsevier Science.

12. Kukli, K., et al., *Influence of thickness and growth temperature on the properties of zirconium oxide films grown by atomic layer deposition on silicon.* Thin Solid Films, 2002. 410(1-2): p. 53-60.

13. Aarik, J., et al., *Growth kinetics and structure formation of ZrO₂ thin films in chloride-based atomic layer deposition process.* Thin Solid Films, 2002. 408(1-2): p. 97-103.

14. Romanes, M.C., *Structure and Low-Temperature Tribology of Lubricious Nanocrystaline ZrO₂ Monofilms and ZnO/Al₂O₃ Nanolaminates Grown by Atomic Layer Deposition*, in *Department of Materials Science & Engineering*2008, University of North Texas: Denton.

15. Chen, H., Y. Zhang, and C. Ding, *Tribological properties of nanostructured zirconia coatings deposited by plasma spraying.* Wear, 2002. 253(7-8): p. 885-893.

16. Oliver, W.C. and G.M. Pharr, *An improved technique for determining hardness and elastic modulus using load and displacement sensing indentation experiments.* Journal of Materials Research 1992. 7: p. 1564-1583

17. Hong, R.J., et al., *Studies on ZnO:Al thin films deposited by in-line reactive mid-frequency magnetron sputtering.* Applied Surface Science, 2003. 207(1-4): p. 341-350.

18. Navamathavan, R., et al., *Nanoindentation 'pop-in' phenomenon in epitaxial ZnO thin films on sapphire substrates.* Materials Characterization, 2008. 59(4): p. 359-364.

19. Lawn, B.R. and M.V. Swain, *Microfracture Beneath Point Indentations in Brittle Solids.* J. Mater. Sci. , 1975. 10: p. 113-122.

20. Suh, N.P., *An overview of the delamination theory of wear.* Wear, 1977. 44(1): p. 1-16.

21. Suh, N.P., *The delamination theory of wear.* Wear, 1973. 25(1): p. 111-124.

22. Adewoye, O.O. and T.F. Page, *Electron microscopy study of surface and subsurface friction damage in single-crystal SiC.* Wear, 1981. 73(2): p. 247-260.

CHAPTER 5

FRETTING WEAR BEHAVIOR OF ATOMIC LAYER DEPOSITED ZrO_2 AND TRILAYER $ZnO/Al_2O_3/ZrO_2$ NANOLAMINATE FILMS ON CARBON-CARBON COMPOSITES

Lifetime of parts fabricated of CCC, like any other load-bearing components that are subjected to vibration, can suffer from fretting wear, fretting fatigue and contact deterioration [1]. The extent of damage is strongly dependent upon a variety of factors such as reciprocating amplitude, number of cycles to fretting, reciprocating frequency, material, contact temperature, stress field and environment [2].

In general, two approaches have been adopted so far to mitigate and prevent the fretting wear: (i) application of surface treatment such as coating and shot peening- in case of metallic substrate, and (ii) design optimization. Where, the aim of the latter is to modify the geometry of components in order to eliminate the excessive shear stress concentration at the interface. The efficiency of the former approach is reliant on the capabilities of coating technique in providing good adhesion between substrate and coating that prevents spallation of coating and prolongs film's survival [3, 4].

Determining the dominant wear mechanism is crucial in order to select the appropriate coating material and coating method. Numerous vacuum coating technologies have been extensively utilised to deposit foreign material to the surface, such as electro-deposition, plasma spray, ion implantation, physical vapour deposition (PVD) and chemical vapour deposition (CVD). But atomic layer deposition (ALD) is an unknown coating technique in terms of combating fretting wear. As shown in Chapter 4, ALD of

binary compounds has proven capabilities in providing extremely conformal and uniform coatings. ALD of elements and ternary materials with precise and uniform thickness is also desirable [5]. Processing of coatings at the nanoscale with nanolaminate configuration, where each laminate has a specific contribution to the whole coating assembly, and composite alloyed coatings are some of the unique potentials of ALD.

In the case of surface treatment to avoid fretting wear, it was shown that if the applied coating exhibits low-friction characteristic, the fretting fatigue can be reduced significantly [6]:

$$S_{fr} = S_0 - 2\mu P_0 [1 - e^{(-I/k)}] \qquad\qquad (Eq.5.1)$$

where S_{fr} is the fretting fatigue strength (MPa), S_0 is the fatigue strength in the absence of fretting (MPa), μ is coefficient of friction, P_0 is contact pressure (MPa), I is reciprocating amplitude (µm) and k is a constant , typically k=3.8 (µm) and for reciprocating amplitude greater than 25(µm), makes the exponential term negligible. According to Eq.5.1, application of low-friction coating can significantly enhance the fretting wear resistance of the substrate.

Tribological coatings such as sulphides, nitrides, selenides, diamond-like carbons (DLC), are known as potential solid lubricants due to their characteristic wear resistance and low coefficient of friction (COF). Reportedly, application of these coatings on the metallic substrates showed significant improvement in fretting wear behaviour [7, 8].

Prolonged exposure of CCC to high temperatures and oxidizing atmospheres, like aerospace applications, can lead to oxidation and subsequent degradation. It is important to select an optimized coating that not only provides solid lubrication to the substrate and

minimizes the extent of fretting wear, but also maintains its lubrication properties at high temperature (i.e. above 500˚C) and severe environmental conditions. It was found that microstructurally-engineered oxides of certain metals (Re, Ti, Mo, Zn, Zr, V, W, B, etc) are potential solid lubricants that can tolerate a wide range of environmental condition and exhibit low friction at elevated temperatures [9, 10].

Although the majority of investigations on CCC have focused on protective coating such as thermal barrier films [11, 12], investigating the fretting wear behaviour of CCC in the presence of solid lubricant coatings needs to be addressed.

ALD was employed to infiltrate monolayer of ~ 200nm ZrO_2 and trilayer with total thickness of ~ 220nm ZnO (~ 100nm) /Al_2O_3 (~ 20nm) /ZrO_2 (~ 100nm) into the porous CCC substrate. High frequency reciprocating rig (HFRR) was employed to simulate the fretting wear conditions at ambient temperature, 150ºC and 400ºC. Subsequently wear factor was calculated for uncoated CCC (control sample) and ALD-coated CCC. FEI Nova 200 NanoLab-focused ion beam (FIB/SEM) was used for high resolution scanning electron microscopy surface imaging and site-specific specimen preparation for cross sectional TEM (XTEM) analyses. Specimen preparation included: ion-milling, lift-out, thinning and polishing. For each step conservatively low voltage and current were employed to minimize ion-beam damage to the TEM specimen. An FEI Tecnai G2 F20 S-twin TEM equipped with a Schottky field-emission gun operated at 200keV was used to investigate the structural features and deformation mechanisms for both conditions of as-deposited and worn films of all CCC samples.

5.1 Fretting Wear Behavior at Ambient Temperature

Fig 5.1 shows the cross-sectional TEM micrographs of the uncoated CCC and as deposited ALD samples prior to fretting testing. Where the microstructure of the ~ 200nm monolayer of ALD ZrO_2 and the ~ 220nm ALD trilayer of $ZnO/Al_2O_3/ZrO_2$ (ZnO~ 100 nm, Al_2O_3 ~ 20 nm, ZrO_2~ 100 nm) was characterized separately in sections 4.1 and 4.3 respectively. HFRR tests were conducted at optimum conditions that entailed application of the normal load of 1 N with a 6.0 mm diameter AISI E-52100 ball under a reciprocating stroke length of 1 mm and reciprocating frequency of 20Hz for the duration of 130 minutes.
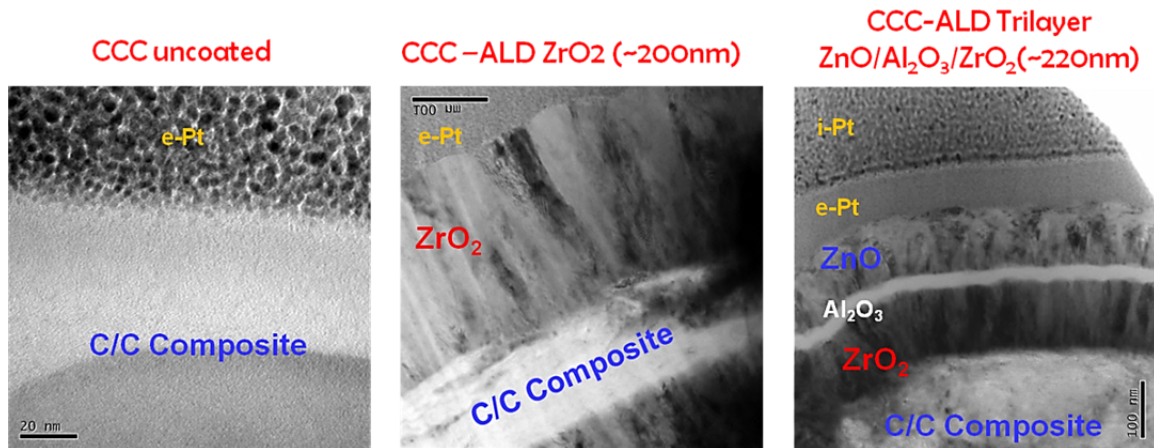
Figure 5.1: Cross-sectional TEM micrographs of uncoated CCC, coated with ALD-ZrO_2 and ALD trilayer before HFRR test.

After HFRR testing, a Veeco Dektak 150 Profilometer was used to calculate the wear area and wear depth of each wear track. Then the wear factor was computed by dividing the cross-sectional areas of the wear track by the load and by the number of cycles (Eq.3.4). By knowing the reciprocating frequency, the number of cycles is converted to the total distance that the ball travelled on the sample.

5.1.1 Microstructure Evolution in Worn Nanolaminate Films at Ambient Temperature

Fig. 5.2 shows the optical images of the AISI E-52100 ball and the wear track after HFRR test at ambient temperature for uncoated CCC, CCC coated with ALD ZrO_2 and CCC coated with ALD trilayer $ZnO/Al_2O_3/ZrO_2$.
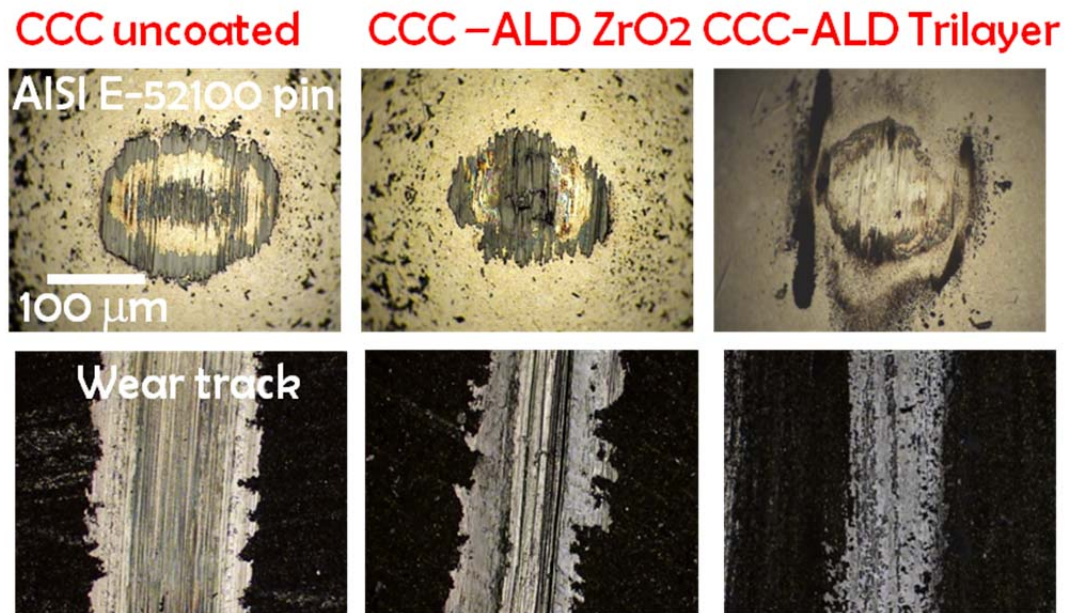

Figure 5.2: Optical images of the ball and wear track after HFRR test at ambient temperature.

It is clear from the optical images in Fig 5.2 that the maximum amount of transfer film was found on the ball for HFRR test on uncoated CCC sample. In addition to the optical images of the wear track in Fig. 5.2., the surface imaging of each wear track by using SEM in Fig 5.3 revealed that uncoated CCC had a wider wear track (~400µm) in comparison to CCC with ALD ZrO_2 (~300-350µm) and CCC ALD Trialyer (~200µm). Therefore, the ALD trilayer, which has least amount of transfer film on the ball and narrowest wear track, exhibits the lowest wear factor.
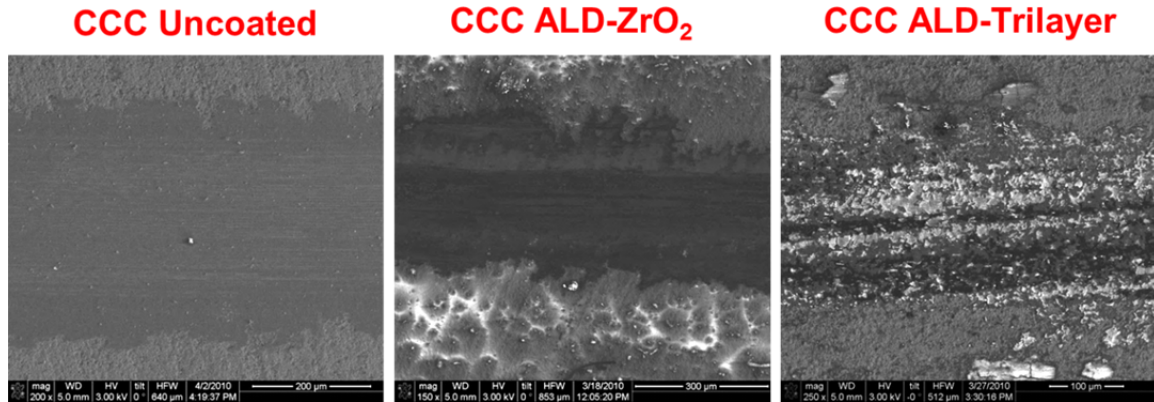
Figure5.3: SEM surface imaging of the wear tracks after fretting wear test at ambient temperature on uncoated CCC, CCC-ALD ZrO$_2$ and CCC-ALD Trilayer.

Profilometry measurements of depth and area of each wear track was performed to calculate the amount of material loss for each sample during the HFRR test at ambient temperature (Fig 5.4). In comparison to the uncoated CCC, CCC with ALD trilayer coating had shown remarkable reduction in the wear factor (~ 65%) and resistance to fretting damage, unlike ALD ZrO$_2$ with ~ 5% improvement. In order to further elucidate the role ALD nanolaminates coatings in providing fretting wear resistance to CCC, cross-sectional ex-situ TEM analyses were conducted. Fig. 5.5 illustrates the XTEM micrographs of the uncoated CCC, CCC ALD-ZrO$_2$ and CCC ALD-Trilayer following the HFRR test at ambient temperature. The comparison between XTEM micrographs in Fig 5.1 and Fig. 5.5 clearly display the microstructural evolution of the worn ALD nanolaminates.

Low magnification BF XTEM micrographs of worn uncoated CCC in Fig 5.5 display the formation of a layer that contains amorphous carbon with approximate thickness of 300 nm. The cross-sectional drift-corrected EDS line scan in STEM image of

the uncoated CCC in Fig. 5.5 shows the presence of carbon and oxygen in this 300 nm-thick layer. No trace of iron was found in this line scan, which is in good agreement with optical image of AISI E-52100 ball in Fig. 5.2 where the ball was not scratched due to the fretting contact.

Breaking of graphitic grains with (0002)-basal plane orientations (Fig. 4.4 (a)) and transformation of these grains into amorphous carbon occurred due to the shear stress induced by contact of AISI E-52100 ball with uncoated CCC. Higher magnification XTEM micrographs of uncoated CCC sample in Fig. 5.5 show the depth of fretting damage to this sample and change in the orientation and structure of the layers below the amorphous layer which emphasizes the susceptibility of uncoated CCC to fretting wear and clarifies why uncoated CCC exhibits very poor wear factor (Fig 5.4).
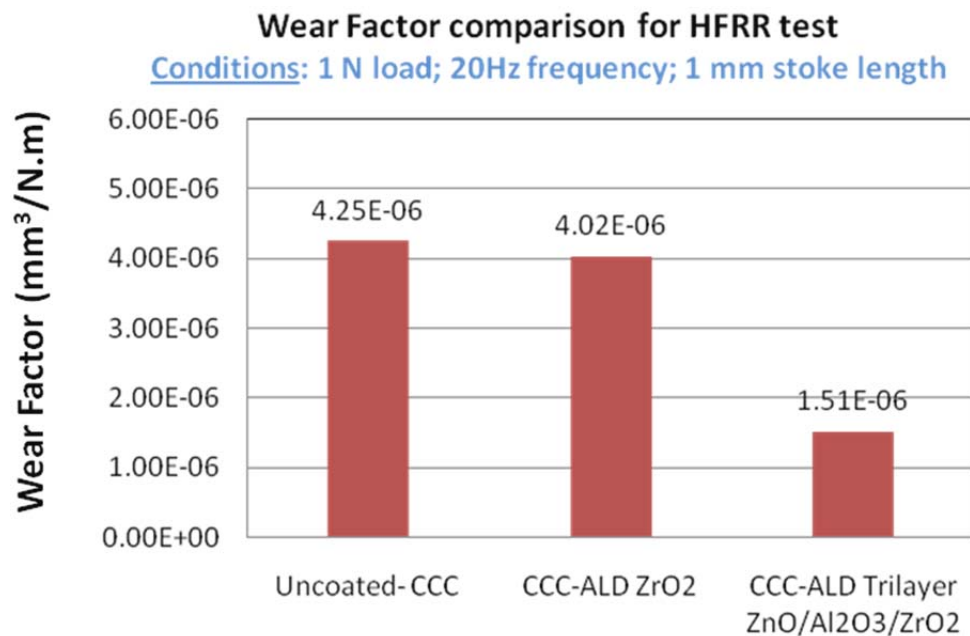

Figure 5.4: Fretting wear factor comparison for HFRR test at ambient temperature between uncoated CCC, CCC-ALD ZrO_2 and CCC-ALD trilayer.
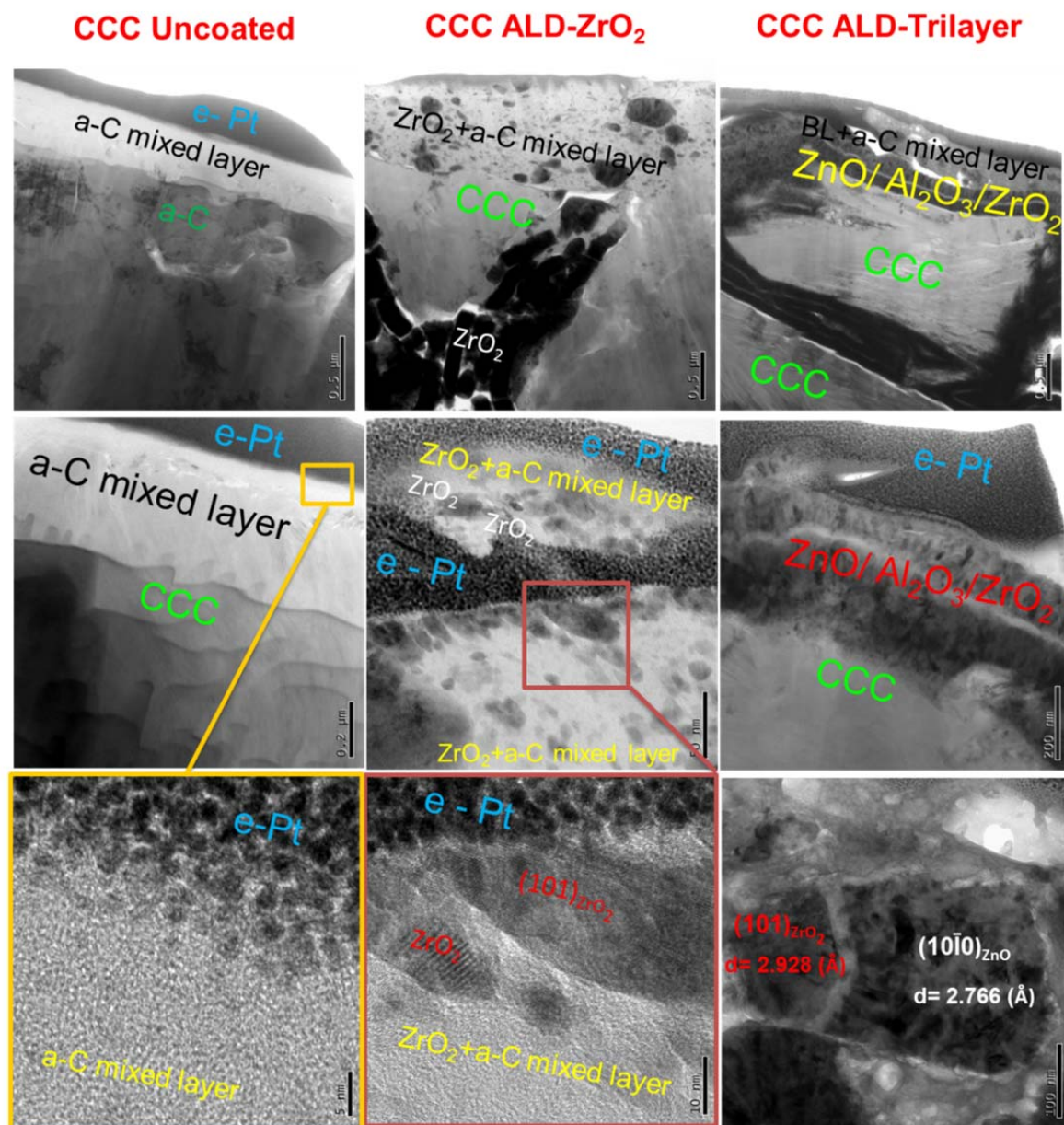
Figure5.5: Cross-sectional TEM micrographs of the worn samples after HFRR test at ambient temperature.

In case of CCC ALD-ZrO_2 the fretting-induced damage led to formation of a mechanically mixed layer (MML) which contains amorphous carbon and various sized nanocrystalline grains of ALD $ZrO_2$with random orientation. Formation of similar layer

in fretting contact of metallic counterfaces was reported by Sauger and co-workers [13], and this tribologically transformed layer contained nanocrystalline structure and is known to be responsible for fretting wear generation.

Moreover, the energy dispersive x-ray spectroscopy (EDS) drift-corrected line scan in Fig 5.6 proves the existence of carbon, zirconium and oxygen in the MML. From the Z-contrast image in the STEM mode, the heavier element (Zr) has higher intensity than the lighter O and C and emphasizes the existence of random orientation of ALD ZrO_2 nanocrystallites.

The fracture of ALD ZrO_2 subsurface coating below the mechanically mixed layer clearly displays the depth of fretting damage and very high strain rate deformation. This is the reason why the CCC ALD-ZrO_2 has comparable fretting wear to uncoated CCC, (wear factors of $4.25x10^{-6}$ and $4.02x10^{-6}$ in Fig 5.4). Higher magnification XTEM micrographs of the same region elucidate the mechanisms responsible for fretting wear formation, where the subsurface fragmented ALD ZrO_2 particles are pushed to the surface due to the contact stress which its direction alters continuously in each reciprocating cycle. This eventually forms a mechanically mixed layer that further reciprocating cycles cause decohesion in the mechanically mixed layer and subsequently lead to wear particle generation. This mechanism is shown in Fig. 5.5 (center figure) where a nanocrystalline wear particle is encapsulated in the protective Pt layer.

The significant wear damage in CCC coated with ALD ZrO_2 can be explained in terms of transformation toughening mechanisms in ZrO_2. It was outlined in section 2.4.2 that pure zirconia exhibits three polymorphic forms under ambient pressure; these are

148

monoclinic, tetragonal and cubic respectively. The tetragonal to monoclinic transformation, which is martensitic in nature, is accompanied by a large (3-5%) volume expansion and is sufficient to exceed the elastic and fracture limit even in relatively small grains of pure ZrO_2 and can only be accommodated by cracking that eventually leads to significant material loss and hence wear.

The as-deposited (unworn) ALD ZrO_2 was characterized to have a tetragonal crystal structure by using XRD and XTEM investigation of CCC sample that was coated with ~200 nm ALD ZrO_2 in Figs 4.3 and 4.4. XTEM micrographs and corresponding FFT pattern in Fig. 5.7 that were taken from wear debris of the mechanically mixed layer after fretting test on CCC ALD ZrO_2 revealed the existence of both monoclinic and tetragonal ZrO_2.

According to Fig 5.4, the CCC coated with ALD trilayer $ZnO/Al_2O_3/ZrO_2$ showed superior fretting wear resistance in comparison to uncoated CCC and CCC coated with ALD ZrO_2. The reason behind of this behavior can be related to the formation of minimum amount of non-uniform mechanically mixed layer (~100 nm) which is clear from XTEM micrographs in Fig 5.5. Likewise, in most of the contact regions the ALD trilayer remained intact after the fretting test and no subsurface damage was observed beneath the mechanically mixed layer. Likewise, the Z-contract imaging Fig 5.6 shows that fretting damage is not significant and ALD trilayer succeeded to preserve its structure beneath the narrow mechanically mixed layer. Thus, the synergistic role of the trilayers provides increased fretting wear resistance, which can be contributed to the solid lubrication of the defective ZnO structure, as outlined in Chapter 4.
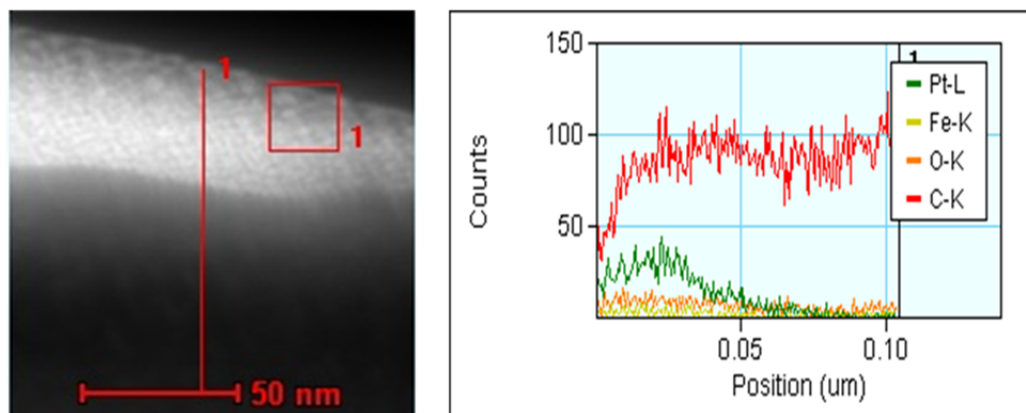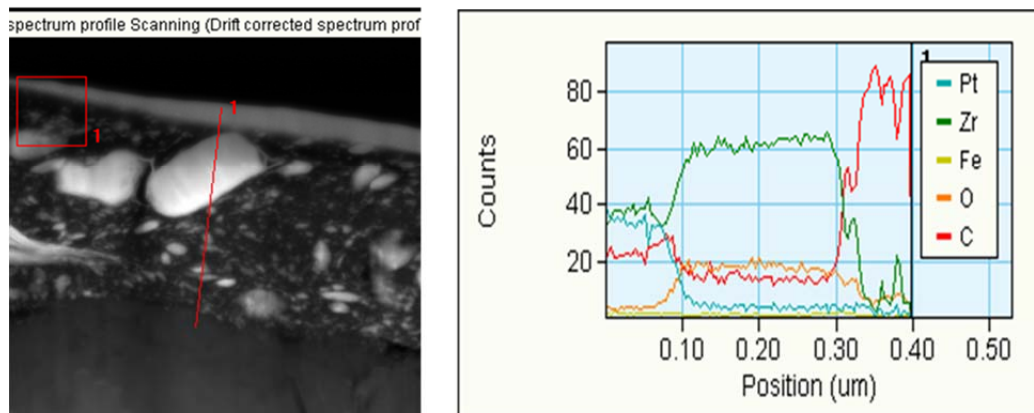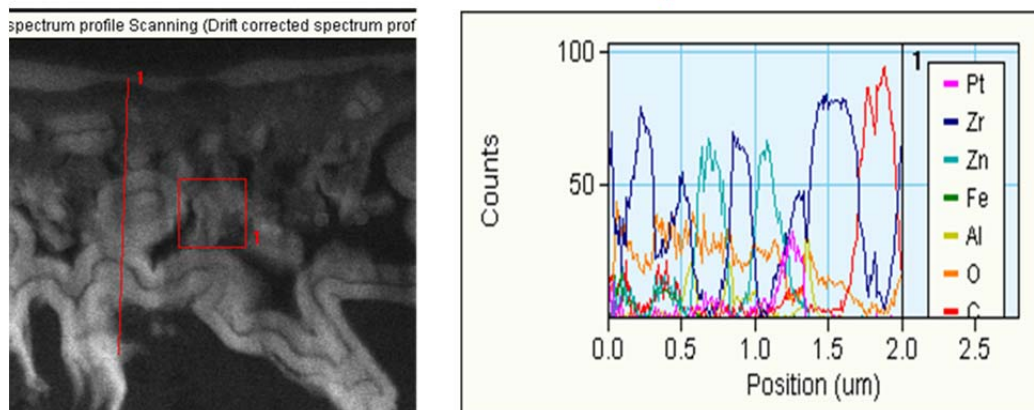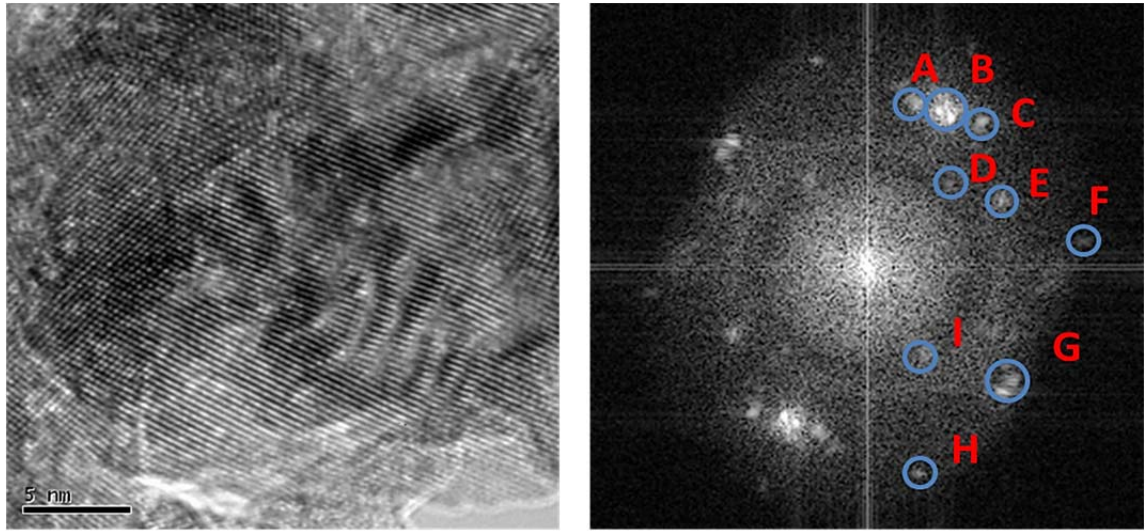
Figure5.6: Cross-sectional EDS line scan results obtained in STEM-HAADF mode illustrate the elemental analysis of the mechanically mixed layer for uncoated CCC, CCC-ALD ZrO_2 and CCC-ALD trilayer after fretting test at ambient temperature.

Diffraction Spot	A	B	C	D	E	F	G	H	I
Phase		T		M	M	T	T	T	T
ZrO$_2$		ZrO$_2$		ZrO$_2$	ZrO$_2$	ZrO$_2$	ZrO$_2$	ZrO$_2$	ZrO$_2$
Atomic plane		(101)		(100)	(110)	(110)	($\bar{1}$01)	($\bar{1}$10)	($\bar{1}$00)

Figure5.7: Cross-sectional high resolution TEM micrograph and the corresponding FFT pattern of ALD ZrO$_2$ grains inside the mechanically mixed layer.

The elemental profile in EDS drift-corrected line scan shows the periodic fluctuation in intensity of Zr and Zn signals which is a good indication that the ALD trilayer remained intact after the fretting test. In addition to formation of minimum amount of mechanically mixed layer and wear particles, the intensity signal assigned to iron in EDS line scan of Fig. 5.6 shows a signal which is close to noise level and hence no iron from the steel counterface is believed to be removed and transferred to the wear track during the fretting test. This is confirmed by observation of the optical image of

AISI E-52100 ball for CCC-ALD trilayer sample (Fig. 5.2), where no roughening or abrasion scars are found on the ball.

5.2 Fretting Wear Behavior at 150°C

      Identical parameters for HFRR fretting test (load, frequency, ball, stroke and time), as explained in section 5.1, were used to conduct the fretting tests at 150°C on uncoated CCC, CCC-ALD ZrO_2 and CCC-ALD trilayer $ZnO/Al_2O_3/ZrO_2$. As a reference, the XTEM micrographs in Fig 5.1 show the structure of each of the abovementioned samples prior to fretting test at 150°C.

5.2.1 Microstructure Evolution in Worn Nanolaminate Films at 150°C

      The optical images of the AISI E-52100 ball and corresponding wear track after HFRR test at 150°C for uncoated CCC, CCC-ALD ZrO_2 and CCC-ALD trilayer $ZnO/Al_2O_3/ZrO_2$ are shown in Fig. 5.8. Optical images of the wear tracks in Fig 5.8 along with SEM micrographs of Fig 5.9 clearly show that the wear track of CCC-ALD trilayer (~ 260 µm) has the narrowest width in comparison to uncoated CCC (~ 370 µm) and CCC-ALD ZrO_2(~ 400µm), which is in agreement with the room temperature fretting tests. Also CCC-ALD trilayer has less amount of film transferred by adhesive wear on the AISI E-52100 ball in comparison to CCC-ALD ZrO_2. These observations are in good agreement with the wear factor calculations in Fig 5.10 where the CCC-ALD trilayer exhibits the highest resistance to fretting damage at 150°C.

      The fretting wear resistance was compared in Fig. 5.10 for each sample at ambient temperature and at 150°C. The CCC-ALD ZrO_2 showed significant increase in wear factor and detrimental effects of higher temperature is obvious for this sample.

Slightly higher wear was observed at 150°C for uncoated CCC compared to the CCC-ALD trilayer conducted at both temperatures.
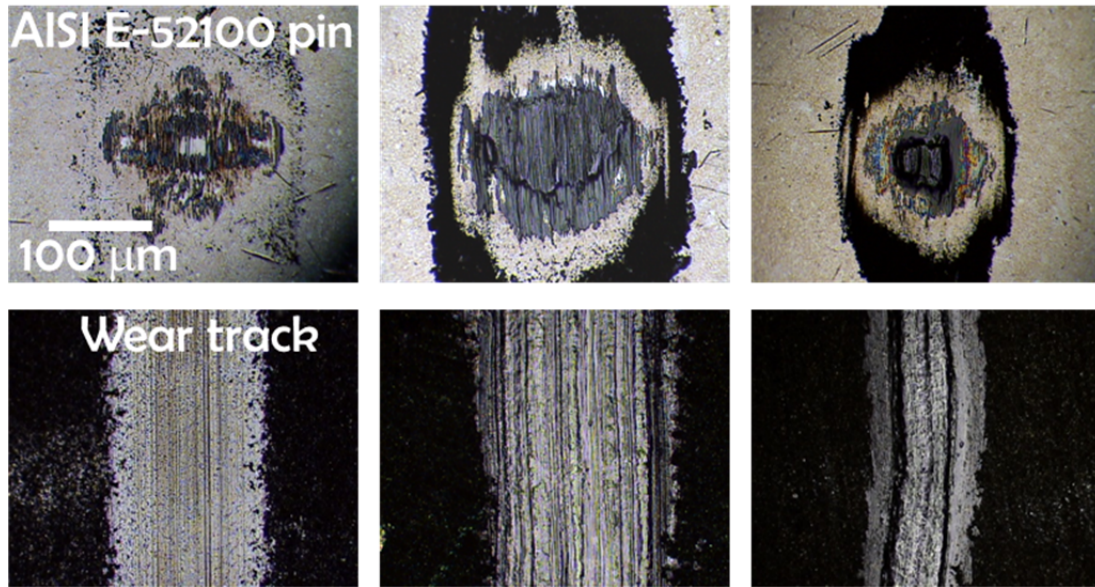

Figure5.8: Optical images of the ball and wear track after HFRR test at 150 °C.
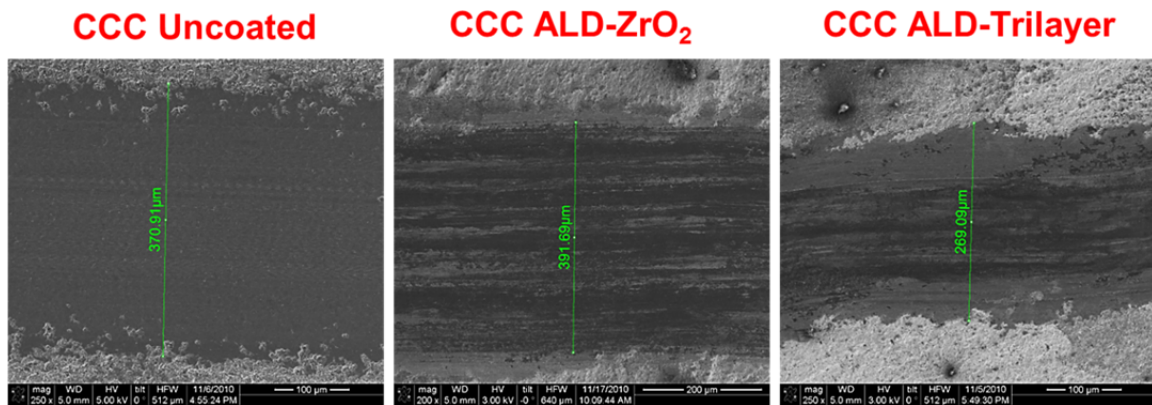

Figure5.9: SEM surface imaging of the wear tracks after fretting wear test at 150 °C on uncoated CCC, CCC-ALD ZrO_2 and CCC-ALD Trilayer.

Cross-sectional TEM micrographs in Fig. 5.11 clearly show the depth of fretting damage to each sample after fretting test conducted at 150°C. For uncoated CCC the fretting test caused the formation of a mixed layer that contains amorphous carbon (the area enclosed within the dash lines). XTEM micrographs of higher magnification illustrate that the layer beneath of the amorphous carbon layer, contains polycrystalline (PX) (0002) - basal planes of graphite. Also evident are sheared grains of graphite which are located right below the amorphous carbon layer.

The EDS drift-corrected line scan in STEM mode by using HAADF detector in Fig. 5.12 displays that the amorphous carbon layer includes traces of iron. A sharp transition in intensity assigned to the iron oxide from amorphous carbon layer into the graphitic substrate is noticeable. This is due to iron being transferred from the AISI E-52100 steel ball to the wear track and oxidized due to tribochemical reactions during the fretting test at 150°C. The sharp transition in the intensity of iron oxide are not observed in the EDS drift-corrected line scans of CCC ALD ZrO_2 and CCC ALD trilayer and iron signal in these line scans was very close to the noise level. The role of iron oxide during the 150°C test does not lower the fretting wear factor, since the wear factor slightly increased at 150°C compared to room temperature testing, as shown in Fig. 5.10.
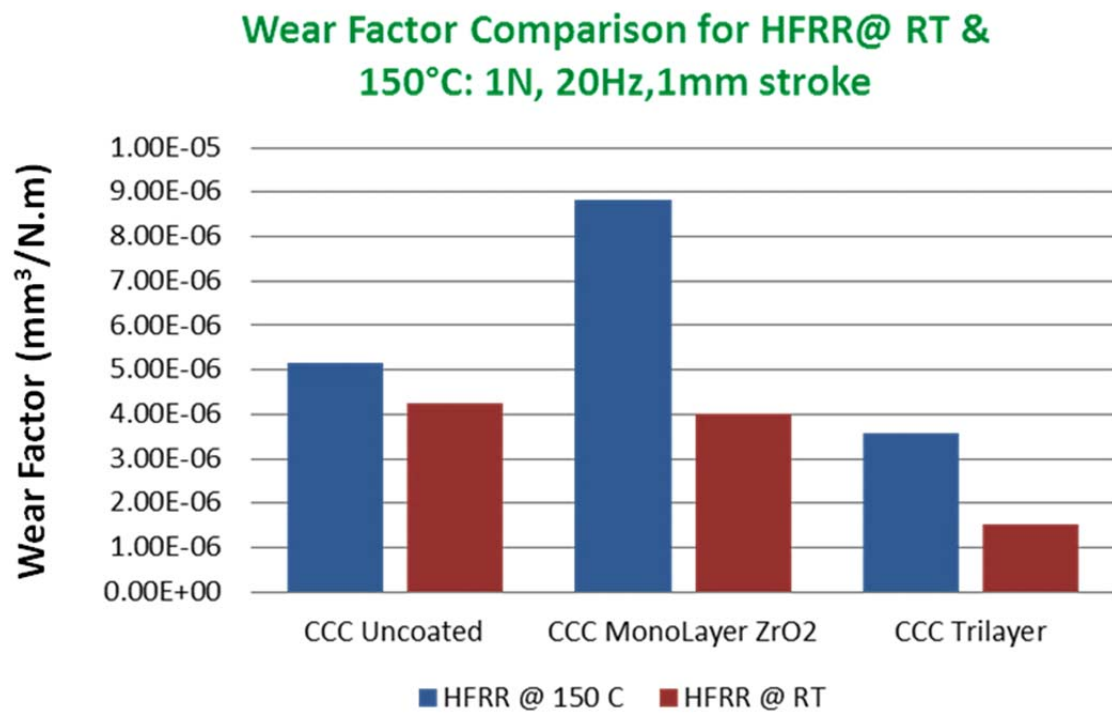
Figure5.10: Wear factor comparison between HFRR tests at ambient temperature and 150 °C on uncoated CCC, CCC coated with ALD ZrO_2 and CCC coated with ALD Trilayer.
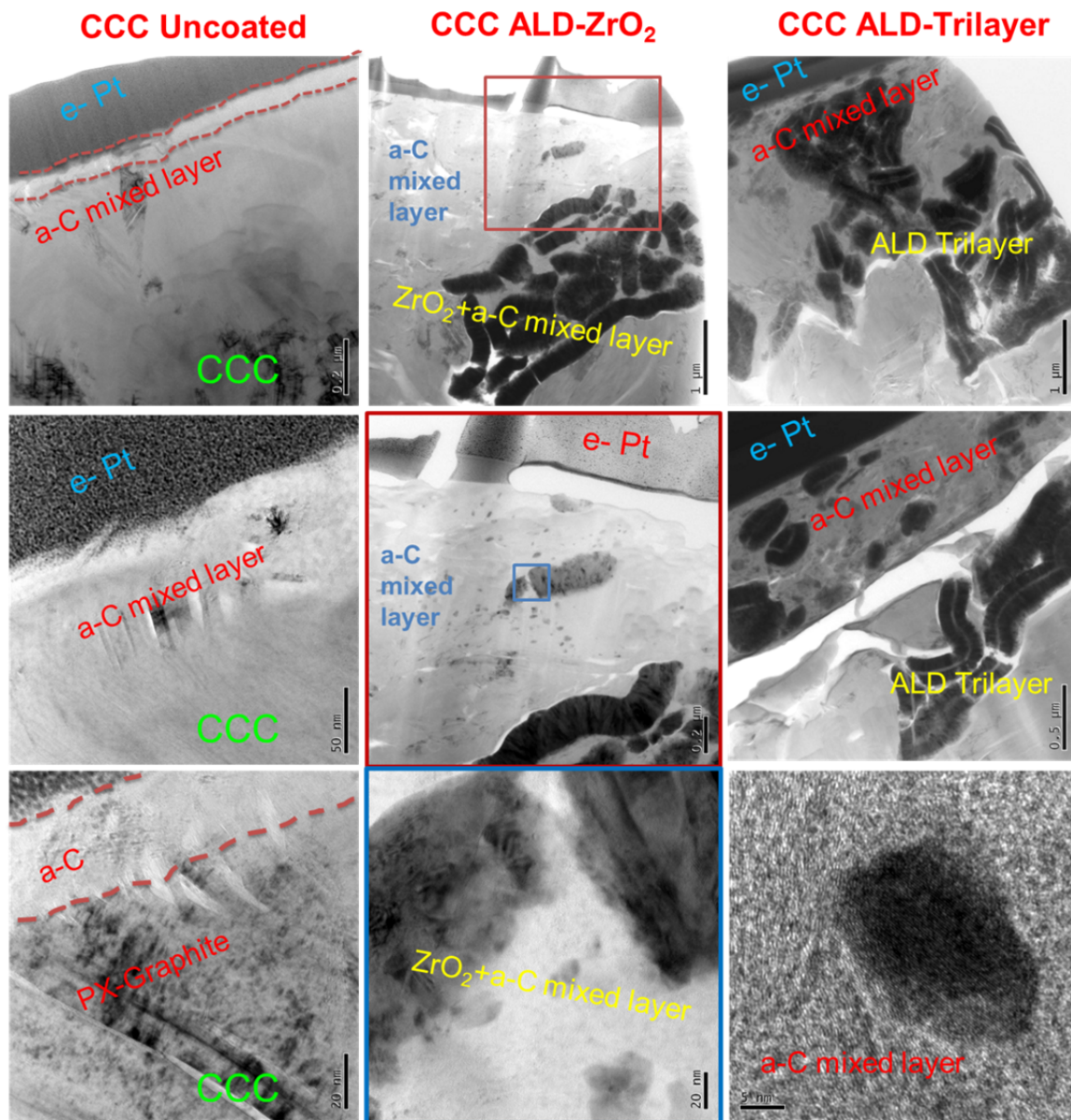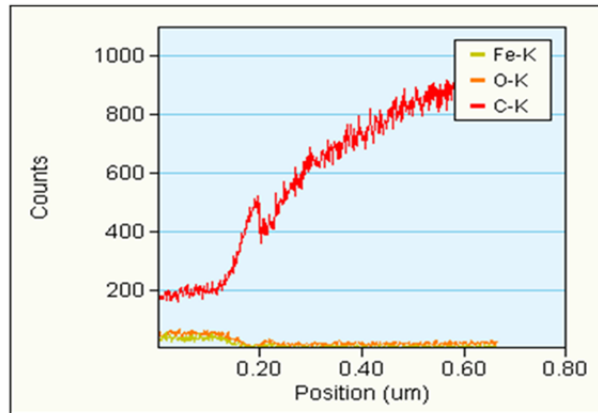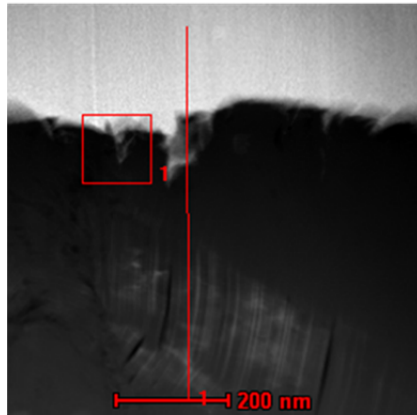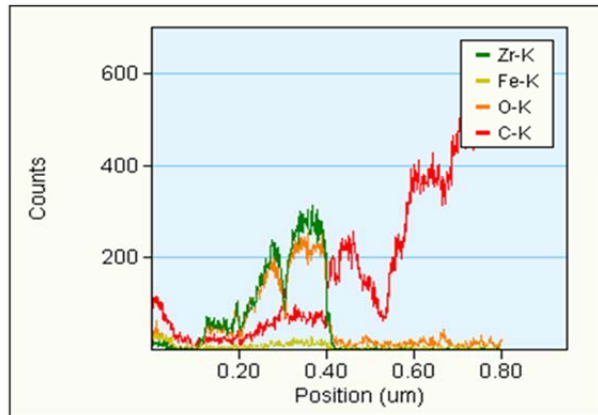
Figure 5.11: Cross-sectional TEM micrographs of the worn samples after HFRR test at 150 °C.
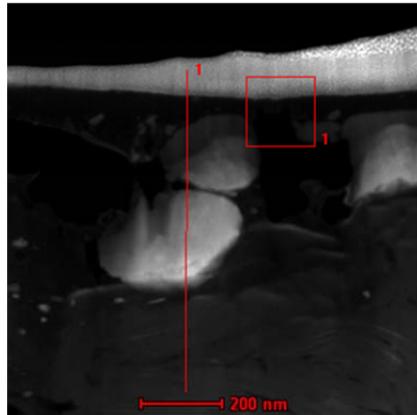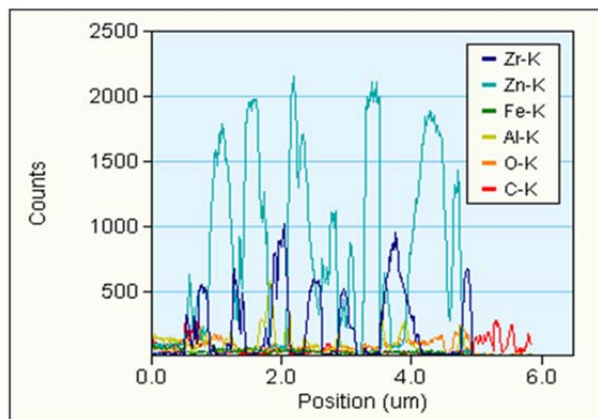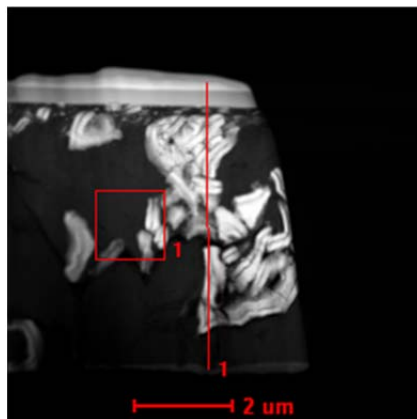
Figure5.12: Cross-sectional EDS line scan results obtained in STEM-HAADF mode that illustrate the elemental analysis of the mechanically mixed layer for uncoated CCC, CCC-ALD ZrO₂ and CCC-ALD trilayer after fretting test at 150°C.

The XTEM micrographs in Fig 5.11 show that CCC ALD ZrO_2 has the largest fretting damage depth and almost no continuous and untouched ALD ZrO_2 was found in the subsurface region. This confirms the highest fretting wear rate of CCC- ALD ZrO_2 in comparison to CCC-ALD trilayer and uncoated CCC. However, the ALD trilayer preserved its structure especially in the subsurface regions and prevented failure of the CCC substrate in the fretting contact that gives rise to the lowest wear factor at 150°C. Moreover, it exhibited the least average friction coefficient (~ 0.16) that shows the ALD trilayer is capable of providing solid lubricity at 150°C. Further clarification about the solid lubricity mechanisms in ALD trilayer will be presented below.

5.3 Fretting Wear Behavior at 400°C

Fretting wear tests were conducted on uncoated CCC, CCC-ALD ZrO_2 and CCC-ALD trilayer $ZnO/Al_2O_3/ZrO_2$ at 400°C by using the same HFRR parameters as section 5.1. As it was explained in sections 5.1 and 5.2, ALD trilayer is capable of protecting CCC against fretting damage and wear, and to some extent it can provide solid lubricity to the carbonaceous substrate up to 150°C.

Investigations on post-annealing of ALD trilayer at 500°C reported that the ALD trilayer maintains its integrity and shows significant thermal stability up to 500°C with just limited grain growth in ALD ZnO layer [14]. But the structural evolution in the presence of a fretting contact during high temperature, where the influences of high temperature are coupled with a high contact shear stress, can be deleterious to the structure. In this section the aim was to reveal the structural changes due to the combined effect of high temperature and fretting contact.

5.3.1 Microstructure Evolution in Worn Nanolaminate Films at 400°C

Fig 5.13 show the optical images of the AISI E-52100 ball and the wear track after HFRR test at 400°C for uncoated CCC, CCC-ALD ZrO_2 and CCC-ALD trilayer $ZnO/Al_2O_3/ZrO_2$. The ball for almost all of the samples has considerable amount of transfer film, especially for CCC-ALD ZrO_2 in which the transfer film on the ball is out of the field of view at 10x magnification. The ball for uncoated CCC sample has vertical scratch marks in the reciprocating direction; this can be due to the formation of a hard material as a third-body that heavily abraded the ball, e.g. iron oxide. Also the discoloration of the ball for all the samples, illustrates the formation of a new phase, most probably iron oxide film, on the surface. This surface film was not observed for the fretting tests that were conducted at ambient temperature or 150°C.
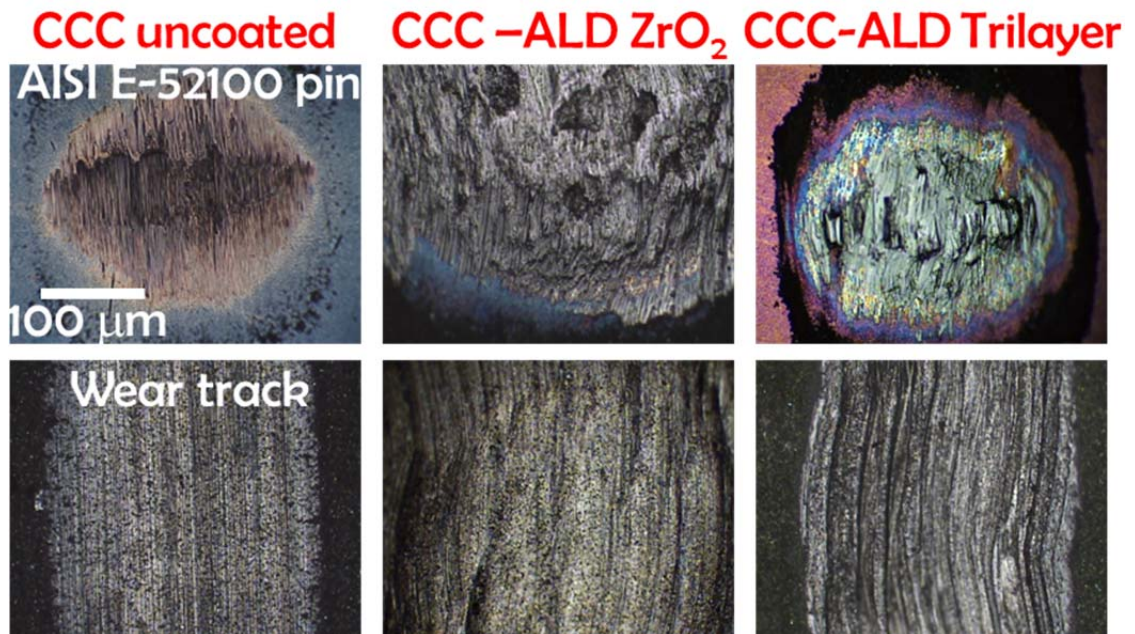

Figure 5.13: Optical images of the ball and wear track after HFRR test at 400°C.

Comparison of the wear tracks show that the wear track of uncoated CCC has approximately the same width (~620 µm) as the wear track of CCC ALD trilayer and this was confirmed by surface imaging that was conducted by SEM (Fig.5.14). However, the CCC-ALD ZrO_2 has the widest wear track (~1000 µm) in optical image of Fig 5.13 and SEM micrograph of Fig. 5.14. Therefore, not surprising it exhibited the highest amount of wear in comparison to uncoated CCC and CCC-ALD trilayer (Fig 5.15). The XTEM micrographs of CCC-ALD ZrO_2 in Fig 5.16 did not show any continuous ALD ZrO_2 film on the surface and subsurface and thus fails to provide some protection to the carbonaceous CCC substrate during the fretting test at 400°C. This was confirmed by drift-corrected EDS line scan in Fig 5.17, where no detectable intensity was found for ZrO_2 in the mechanically mixed layer.

The wear factor calculation for fretting tests at 400°C showed that the CCC-ALD trilayer has a slightly higher wear factor than uncoated CCC. The XTEM micrographs in Fig.5.16 shows increased surface damage for CCC-ALD trilayer, compared to room temperature and 150°C tests. It seems that having a protective ALD coating on CCC substrate provided some fretting wear resistance at 400°C.

The drift-corrected EDS line scan in Fig. 5.17 on both uncoated CCC and CCC-ALD trilayer showed that the CCC-ALD trilayer could not preserve its integrity and was fractured during the fretting contact at 400°C. Also it was revealed that the uncoated CCC has Fe_xO_y particles that were implanted very well on the surface and to some extent to the subsurface of uncoated CCC (Fig. 5.16). Thus, iron oxide is biasing the results, but in the real-life application mating surfaces are often made up of the same material (self-

mated contacts). In other words, it seems unrealistic to have a steel counterface on the carbonaceous substrate in real applications at high temperature. Lastly, based on the XTEM images in Figs. 5.16 and 5.17, the ALD trilayer still provides solid lubricity to CCC at 400°C.
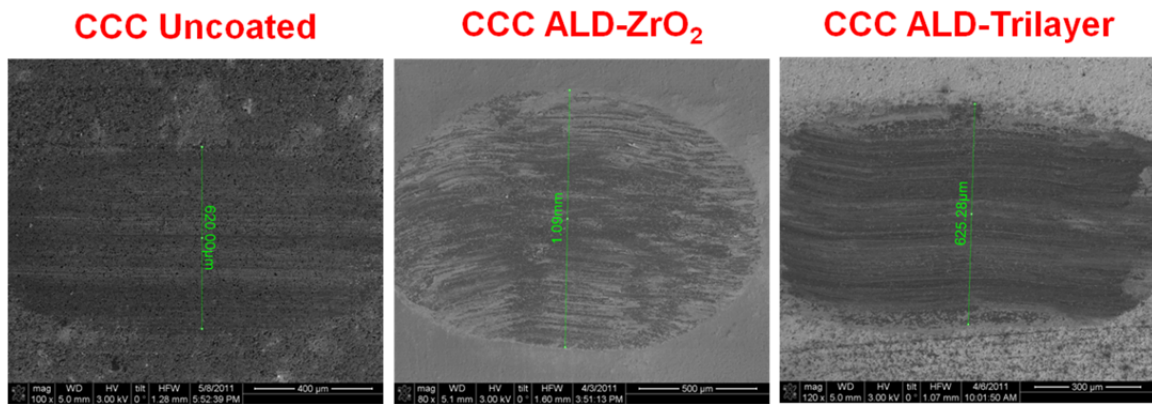

Figure 5.14: SEM surface imaging of the wear tracks after fretting wear test at 400ºC on uncoated CCC, CCC-ALD ZrO_2 and CCC-ALD Trilayer.

Wear Factor Comparison for HFRR@ RT, 150°C & 400 °C: 1N, 20Hz,1mm stroke
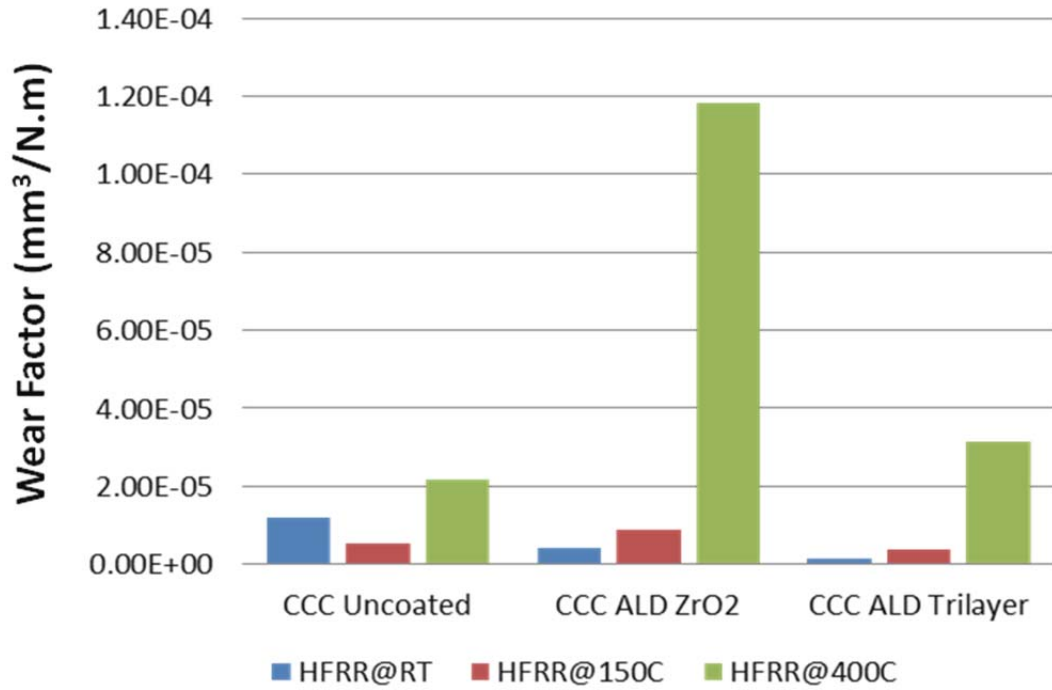
CCC Uncoated	CCC-ALD ZrO$_2$	CCC-ALD Trilayer	
1.19E-05	4.02E-06	1.51E-06	RT
5.17E-06	8.82E-06	3.57E-06	150°C
2.15E-05	1.18E-04	3.13E-05	400°C

Figure 5.15: Wear factor comparison in HFRR tests at ambient temperature, 150°C and 400°C on uncoated CCC, CCC coated with ALD ZrO$_2$ and CCC coated with ALD Trilayer.

162

Figure 5.16:Cross-sectional TEM micrographs of the worn samples after HFRR test at 400°C.
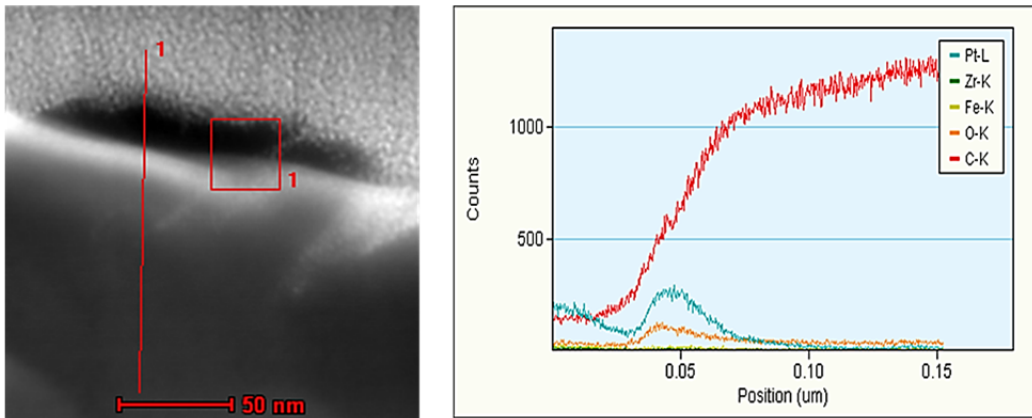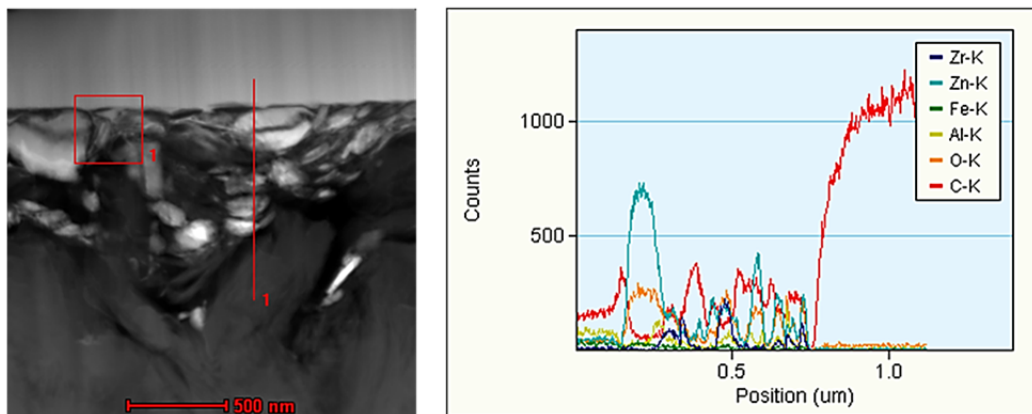
Figure 5.17: Cross-sectional EDS line scan results obtained in STEM-HAADF mode that illustrate the elemental analysis of the mechanically mixed layer for uncoated CCC, CCC-ALD ZrO₂ and CCC-ALD trilayer after fretting test at 400°C.

164

Further STEM analysis (Fig. 5.18) on the surface layers showed that the there exist a continuous layer of Fe_xO_y on the surface of uncoated CCC after fretting test at 400°C. This can play the role of a tribofilm to separate the surfaces in contact and gives a rise to low wear rate and prevents the subsequent failure. In summary, Fig. 5.19 shows schematics of the Raman spectroscopy determined tribochemical phases present on the contacting surfaces, both first bodies (wear track and counterface ball) and third bodies (transfer films adhered to counterface balls).
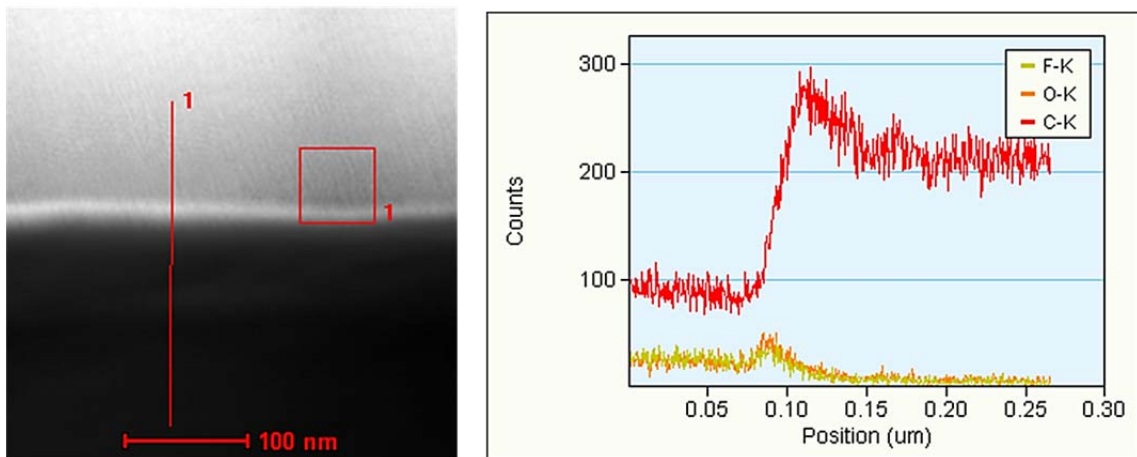
Figure 5.18: Cross-sectional EDS line scan results obtained in STEM-HAADF mode that illustrate the presence of a uniform iron oxide layer on the surface of uncoated CCC after fretting test at 400°C.

As it was mentioned earlier, the CCC-ALD trilayer showed a slightly higher wear rate in comparison to the uncoated CCC (3.13E-05 vs. 2.15E-05), but its average friction coefficient was much lower than the uncoated CCC (~0.24 vs. ~0.87). Furthermore, unlike uncoated CCC, no scratch marks were found on the AISI E-52100 ball after

fretting contact on the ALD trilayer, therefore it can also be concluded that the ALD trilayer is capable of playing the role of solid lubricant for the CCC substrate. In order to elucidate the fundamental friction mitigation mechanism in ALD trilayer, additional TEM investigations were conducted on the worn ALD ZnO layer, the surface layer in the ALD trilayer of $ZnO/Al_2O_3/ZrO_2$.
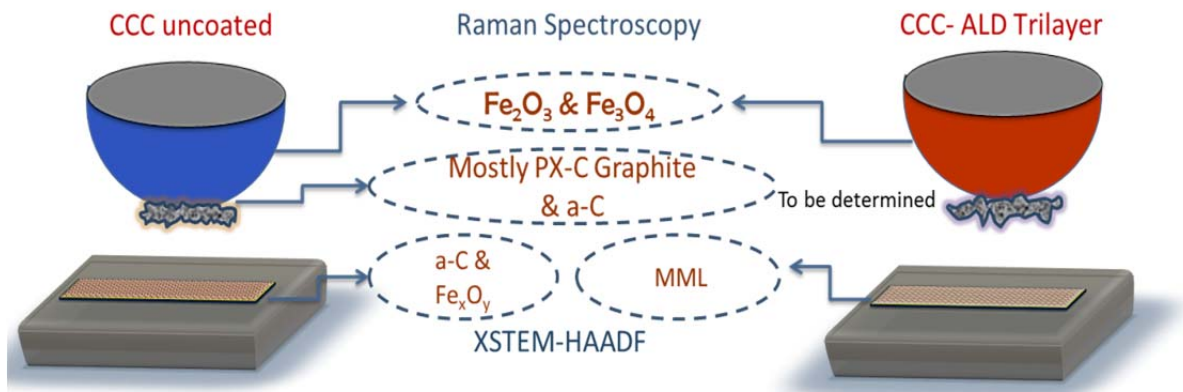
Figure 5.19: Schematics of the Raman spectroscopy determined tribochemical phases on the contacting surfaces (counterface balls sliding on CCC uncoated and CCC-ALD trilayer) and the generation of transfer films (third bodies) on the balls.

The high resolution XTEM micrograph, corresponding FFT pattern and central dark field images in Fig 5.20 revealed a higher density of ZnO (0002) sliding-induced Basal Stacking Faults (white arrows) compared to unworn ZnO (similar mechanism to slower sliding speed that was observed for pin-on-disc experiments in Chapter 4). It seems the activation of the subsurface basal stacking faults will promote the intrafilm shear/slip (see Fig. 2.9 (a) schematic) and hence improve the friction. The intrafilm shear with this friction-induced subsurface activation of stacking faults aid in shear accommodation and prevent brittle fracture.

166
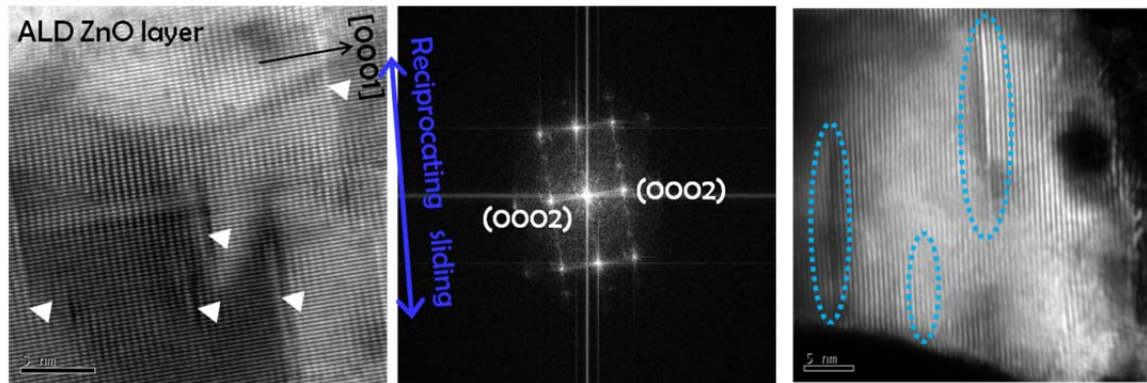
Figure 5.20: HRXTEM image, FFT pattern, and central dark field image show a higher density of ZnO (0002) sliding-induced basal stacking Faults (white arrows).

5.4 Chapter Summary

Investigating the changes in the fretting wear behavior of carbon-carbon composite (CCC) in the presence of solid lubricant coating, was the main objective of this chapter. Atomic layer deposition (ALD) was utilized to infiltrate monolayer of ~ 200nm ZrO_2 and trilayer with total thickness of ~ 220nm $ZnO/Al_2O_3/ZrO_2$ into the porous CCC substrate. High frequency reciprocating rig (HFRR) was employed to simulate the fretting wear condition at room temperature, 150ºC and 400ºC followed by computation of wear factor for uncoated and ALD-coated CCC. Cross-sectional transmission electron microscopy (XTEM) analysis, high resolution TEM (HRTEM) and Z-contrast imaging (STEM-HAADF) were used in order to characterize the tribological contact and the mechanisms responsible for fretting damage. The application of ALD trilayer of $ZnO/Al_2O_3/ZrO_2$ into the CCC substrate led to % 65 improvements in wear factor for fretting tests at ambient temperature. Formation of the MML, due to fretting contact, was found to be responsible for the fretting wear behavior. ALD trilayer

$ZnO/Al_2O_3/ZrO_2$ exhibited least amount of MML in comparison to uncoated and ALD ZrO_2-CCC; instead, the defective solid lubricant ZnO in the ALD trilayer mitigated fretting wear.

Conducting the HFRR tests at RT, 150°C & 400°C revealed that the ALD trilayer of $ZnO/Al_2O_3/ZrO_2$ infiltration into CCC has shown better fretting wear resistance at ambient temperature and 150°C in comparison of uncoated CCC and CCC-ALD ZrO_2 coated, but at 400°C the wear factor is very close to the uncoated CCC biased by the results of the formation of iron oxide.

High density of sliding (shear)-induced stacking faults were observed inside the wear tracks (in comparison to unworn nanolaminates) that were responsible for solid lubrication. In this case, activating subsurface basal stacking faults will promote intrafilm shear/slip and hence improve friction and wear. The slip of partial dislocations likely results from dislocation glide process, as in low speed sliding in Chapter 4. Intrafilm shear with this friction induced subsurface (mechanically mixed layer) also aids in shear accommodation.

ALD $ZnO/Al_2O_3/ZrO_2$ nanolaminates are good candidates for providing low friction and wear and potentially high thermal (oxidation) resistant surfaces and interfaces in moving mechanical assembles, such as CCC bushings in jet engines that experience fretting wear.

5.5 Chapter References

1.   Berthier, Y., L. Vincent, and M. Godet, *Fretting fatigue and fretting wear.* Tribology International, 1989. 22(4): p. 235-242.

2.   Stachowiak, G.W. and A.W. Batchelor, *Fretting and Minor Wear Mechanisms*, in *Engineering Tribology* 2006, Butterworth-Heinemann. p. 621-650.

3.   Waterhouse, R.B., Fretting Wear, in ASM metals handbook volume frictio lubrication and wear technology1992, ASM International.

4.   Stachowiak, G.W. and A.W. Batchelor, *Solid Lubrication & Surface Treatments*, in *Engineering Tribology* 2006, Butterworth-Heinemann. p. 419-459.

5.   Doll, G.L., et al., Chemical Vapor Deposition and Atomic Layer Deposition of Coatings for Mechanical Applications. Journal of Thermal Spray Technology, 2010. 19(1/2): p. 510-516.

6.   Nishioka, K. and K. Hirakawa, Fundamental Investigations of Fretting Fatigue : (Part 5, The Effect of Relative Slip Amplitude). Bulletin of JSME, 1969. 12(52): p. 692-697.

7.   Korsunsky, A.M., A.R. Torosyan, and K. Kim, Development and characterization of low friction coatings for protection against fretting wear in aerospace components. Thin Solid Films, 2008. 516(16): p. 5690-5699.

8.   Fouvry, S., P. Kapsa, and L. Vincent, *Fretting behaviour of hard coatings under high normal load.* Surface and Coatings Technology, 1994. 68-69: p. 494-499.

9.   Zabinski, J.S., et al., Lubrication using a microstructurally engineered oxide: performance and mechanisms. Tribology Letters, 2000. 8(2): p. 103-116.

10. Erdemir, A., *A crystal-chemical approach to lubrication by solid oxides.* Tribology letters, 2000. 8(2-3): p. 97-102.

11. Huang, J.-F., et al., Oxidation resistant yttrium silicates coating for carbon/carbon composites prepared by a novel in-situ formation method. Ceramics International, 2007. 33(5): p. 887-890.

12. Park, S.J., M.K. Seo, and J.R. Lee, Effect of oxidation inhibitor on the low energy tribological behavior of carbon-carbon composites. Carbon, 2002. 40(6): p. 835-843.

13. Sauger, E., et al., *Tribologically transformed structure in fretting.* Wear, 2000. 245(1-2): p. 39-52.

14. Mensah, B.A., Growth, structure and tribological properties of atomic layer deposited lubricious oxide nanolaminates, in Department of Materials Science and Engineering2010, University of North Texas: Denton.

CHAPTER 6

CONCLUSIONS AND FUTURE WORK

6.1 Conclusions

Enhancements in tribological behavior of the carbon-carbon composite (CCC) were the focus of this investigation. Since carbon is susceptible to oxidation and subsequent failure at temperatures above 350ºC, various tribological and protective coatings were designed in an attempt to minimize the friction and wear, particularly at high temperature. Atomic layer deposition (ALD) was employed to infiltrate tribological coatings into the CCC substrate. Evaluation of the tribological behavior were conducted by using unidirectional pin-on-disc tribometer and high frequency reciprocating rig for sliding wear test at ambient temperature and fretting wear test at ambient temperatures well as elevated temperatures, respectively. In order to elucidate the microstructural evolutions in the as-deposited films as well as the worn films, characterization techniques such as XRD, SEM, transmission electron microscopy (TEM), high resolution TEM (HRTEM) and Z-contrast imaging (STEM-HAADF) were used to characterize the mechanisms of damage evolution and succeeding failure due to tribological contact. The changes in microstructural features before and after tribological testing revealed the mechanisms responsible for friction and wear. Furthermore, conducting the tribological testing at elevated temperatures evaluated the thermal stability of the films in the presence of tribological contacts. To further characterize the mechanical properties of

ALD films, that are subject of these analyses, few nanoindentation experiments showed the mechanical response of ALD films in terms of hardness and elastic modulus.

6.1.1 Unidirectional Sliding Wear Test

Monolayer ZrO_2 coating and trilayer nanolaminate $ZnO/Al_2O_3/ZrO_2$ coating were infiltrated into carbon-carbon composite by application of atomic layer deposition to enhance oxidation resistance and wear resistance. These coatings exhibited excellent conformality and pore-filling capabilities into the carbon-carbon composite and carbon foam. The tribological investigations, included pin-on-disc unidirectional sliding wear tests, exhibited a significant reduction for sliding friction and wear factor compared to the uncoated carbon-carbon composite. Characterization of unworn and worn surfaces was performed by energy dispersive x-ray spectroscopy (EDS) mapping in SEM, transmission electron microscopy (TEM), STEM/HAADF, and X-ray diffraction (XRD). EDS maps showed that the depth that $ALD-ZrO_2$ penetrated into the CCC is dependent on the exposure time of ZrO_2 precursors. High resolution TEM (HRTEM) and corresponding XRD analysis determined the textured crystalline phases of (0002) graphite and (101) ZrO_2 (tetragonal) and (0002)-orientated grains of wurtzite ZnO. Unlike the monolayer of ALD ZrO_2, the trilayer coating of ALD $ZnO/Al_2O_3/ZrO_2$ provided lubricity to carbon-carbon composite by reduction in friction coefficient and wear. High resolution transmission electron microscopy investigations on ALD ZnO revealed that the {0002} basal planes in wurtzite ZnO accommodate the shear strains by dislocation glide along the basal planes. Further HRTEM investigations conducted on various ZnO samples for additional determined the deformation and failure mechanisms in ALD ZnO. These

samples included single crystal ZnO with {0001} orientation, single crystal ZnO with {1$\bar{1}$00} orientation and nanocrystalline ZnO with randomly oriented grains. In brief the following are the summary and conclusions of results:

- ALD ZrO_2 infiltration into CCC caused ~34% reduction in wear factor compared to uncoated CCC. Also employing longer exposure time of ALD ZrO_2 precursors led to uniform closure of subsurface pores and further wear decrease to ~51%. A further reduction in wear rate and higher thermal resistance is anticipated with the conversion of the ALD ZrO_2 and CCC interface to hybrid layer of ZrC by means of carbothermal reduction.

- ALD exhibited superior capabilities in deposition of conformal and uniform nanolaminates with sharp interfaces without any intermixing. This behavior is more noticeable for subsurface porosities that were filled with sequential and conformal layer of nanolaminates.

- Improvement in friction and wear behavior was observed with ALD infiltration of trilayer $ZnO/Al_2O_3/ZrO_2$ nanolaminates into CCC and on Si substrates. The lowest friction coefficient (~0.2) was observed in pure sliding for ALD textured ZnO {0002} nanocrystalline grains in comparison to single crystal ZnO-{0001} (~0.5), single crystal ZnO-{1$\bar{1}$00} (~0.4) and randomly oriented ZnO nanocrystalline grains (~0.4).

- A high density of ZnO sliding (shear)-induced stacking faults were observed inside the wear tracks of the worn ALD trilayer (in comparison to unworn nanolaminates) which are responsible for solid lubrication. This is in contrast to the single crystals

which exhibit lower stacking fault densities (no grain boundary sources) and undergo brittle fracture that are responsible for higher friction. Also the ZnO sample with polycrystalline randomly orientated nanocrystalline grains has multiple slip systems operative but not the most favorable, single (0002)-orientated slip system.

- Activating subsurface basal stacking faults that are bordered by partial dislocations will promote intrafilm shear/slip and hence improve friction. The slip of partial dislocations likely resulted from a dislocation glide process, but in situ techniques, such as probe sliding in the TEM, are needed to visualize these events.

- Intrafilm shear with a friction induced subsurface (mechanically mixed layer) also aided in shear accommodation by preventing brittle fracture.

- Nanoindentation analysis on the ALD ZrO_2 and ALD one trilayer $ZnO/Al_2O_3/ZrO_2$ deposited on Si wafer revealed that the ALD trilayer exhibited higher resistance to static loading, which is a further benefit of this trilayer coating.

Therefore based on these results and mechanisms, ALD $ZnO/Al_2O_3/ZrO_2$ nanolaminates are good candidates for providing low friction and wear and potentially high thermal (oxidation) resistant surfaces and interfaces in moving mechanical assembles, such as MEMS devices and CCC bushings that experience wear and surface damage.

6.1.2 Fretting Test

Investigating the changes in the fretting wear behavior of carbon-carbon composite (CCC) in the presence of solid lubricant coating, was the main objective of this chapter. Atomic layer deposition (ALD) was utilized to infiltrate monolayer of ~ 200nm ZrO_2 and trilayer with total thickness of ~ 220nm $ZnO/Al_2O_3/ZrO_2$ into the porous CCC substrate. High frequency reciprocating rig (HFRR) was employed to simulate the fretting wear condition at room temperature, 150 ºC and 400 ºC followed by computation of wear factor for uncoated and ALD-coated CCC. Cross-sectional transmission electron microscopy (XTEM) analysis, high resolution TEM (HRTEM) and Z-contrast imaging (STEM-HAADF) were used in order to characterize the tribological contact and the mechanisms responsible for fretting damage. The application of ALD trilayer of $ZnO/Al_2O_3/ZrO_2$ into the CCC substrate led to % 65 improvements in wear factor for fretting tests at ambient temperature. Formation of the MML, due to fretting contact, was found to be responsible for the fretting wear behavior. ALD trilayer $ZnO/Al_2O_3/ZrO_2$ exhibited least amount of MML in comparison to uncoated and ALD ZrO_2-CCC; instead, the defective solid lubricant ZnO in the ALD trilayer mitigated fretting wear.

Conducting the HFRR tests at RT, 150°C & 400°C revealed that the ALD trilayer of $ZnO/Al_2O_3/ZrO_2$ infiltration into CCC has shown better fretting wear resistance at ambient temperature and 150°C in comparison of uncoated CCC and CCC-ALD ZrO_2 coated, but at 400°C the wear factor is very close to the uncoated CCC biased by the results of the formation of iron oxide.

High density of sliding (shear)-induced stacking faults were observed inside the wear tracks (in comparison to unworn nanolaminates) that were responsible for solid lubrication. In this case, activating subsurface basal stacking faults will promote intrafilm shear/slip and hence improve friction and wear. The slip of partial dislocations likely results from dislocation glide process, as in low speed sliding in Chapter 4. Intrafilm shear with this friction induced subsurface (mechanically mixed layer) also aids in shear accommodation.

ALD $ZnO/Al_2O_3/ZrO_2$ nanolaminates are good candidates for providing low friction and wear and potentially high thermal (oxidation) resistant surfaces and interfaces in moving mechanical assembles, such as CCC bushings in jet engines that experience fretting wear.

6.2 Future Work

Further microstructural investigation that can resolve the properties of ALD coatings can be listed as:

- Using XTEM analyses to clarify the deformation mechanisms in ALD thin films under the nanoindentation loading under the various testing mode, this can lead into clarification of the slip systems and dislocation activities and eventually can be advantageous to optimize an ALD coating that exhibit superior mechanical properties.

- In situ TEM probe studies to study the dislocation glide process during sliding.

- One of the major reasons behind the failure of ALD ZrO_2 film was related to the transformation toughening mechanism by which the tetragonal ZrO_2 undergoes a shear-based martensitic transformation into the monoclinic ZrO_2. This is usually associated with 3-5% volume expansion. Alloying the ZrO_2 with some oxide like Y_2O_3 can bypass this transformation and stabilizes the tetragonal ZrO_2 up to ambient temperature. Hence, design and optimization of an ALD Y_2O_3 layer on ALD ZrO_2 is likely to lead into some enhancement in wear reduction.

- Increased high temperature fretting tests above 400°C, e.g, up to 700°C, to see how lubricious the ZnO is at higher temperatures.